Front Propagation and Feedback in Convective Flow Fields

Saikat Mukherjee

Dissertation submitted to the Faculty of the

Virginia Polytechnic Institute and State University

in partial fulfillment of the requirements for the degree of

Doctor of Philosophy

in

Engineering Mechanics

Mark R. Paul, Chair

Shane D. Ross

Mark A. Stremler

Sunghwan Jung

Danesh K. Tafti

April 24, 2020

Blacksburg, Virginia

Keywords: Reaction-Advection-Diffusion, Front Propagation, Rayleigh-Bénard Convection

Front Propagation and Feedback in Convective Flow Fields

Saikat Mukherjee

(ABSTRACT)

This dissertation aims to use theory and numerical simulations to quantify the propagation of fronts, which consist of autocatalytic reaction fronts, fronts with feedback and pattern forming fronts in Rayleigh-Bénard convection. The velocity and geometry of fronts are quantified for fronts traveling through straight parallel convection rolls, spatiotemporally chaotic rolls, and weakly turbulent rolls. The front velocity is found to be dependent on the competing influence of the orientation of the convection rolls and the geometry of the wrinkled front interface which is quantified as a fractal having a non-integer box-counting dimension. Front induced solutal and thermal feedback to the convective flow field is then studied by solving an exothermic autocatalytic reaction where the products and the reactants can vary in density. A single self-organized fluid roll propagating with the front is created by the solutal feedback while a pair of propagating counterrotating convection rolls are formed due to heat release from the reaction. Depending on the relative change in density induced by the solutal and thermal feedback, cooperative and antagonistic feedback scenarios are quantified. It is found that front induced feedback enhances the front velocity and reactive mixing length and induces spatiotemporal oscillations in the front and fluid dynamics. Using perturbation expansions, a transition in symmetry and scaling behavior of the front and fluid dynamics for larger values of feedback is studied. The front velocity, flow structure, front geometry and reactive mixing length scales for a range of solutal and thermal feedback are quantified. Lastly, pattern forming fronts of convection rolls are studied and the wavelength and velocity selected by the front near the onset of convective instability are investigated.

This research was partially supported by DARPA Grant No. HR0011-16-2-0033. The numerical computations were done using the resources of the Advanced Research Computing center at Virginia Tech.

Front Propagation and Feedback in Convective Flow Fields

Saikat Mukherjee

(GENERAL AUDIENCE ABSTRACT)

Quantification of transport of reacting species in the presence of a flow field is important in many problems of engineering and science. A front is described as a moving interface between two different states of a system such as between the products and reactants in a chemical reaction. An example is a line of wildfire which separates burnt and fresh vegetation and propagates until all the fresh vegetation is consumed. In this dissertation the propagation of reacting fronts in the presence of convective flow fields of varying complexity is studied. It is found that the spatial variations in a convective flow field affects the burning and propagation of fronts by reorienting the geometry of the front interface. The velocity of the propagating fronts and its dependence on the spatial variation of the flow field is quantified. In certain scenarios the propagating front feeds back to the flow by inducing a local flow that interacts with the background convection. The rich and emergent dynamics resulting from this front induced feedback is quantified and it is found that feedback enhances the burning and propagation of fronts. Finally, the properties of pattern forming fronts are studied for fronts which leave a trail of spatial structures behind as they propagate for example in dendritic solidification and crystal growth. Pattern forming fronts of convection rolls are studied and the velocity of the front and spatial distribution of the patterns left behind by the front is quantified.

This research was partially supported by DARPA Grant No. HR0011-16-2-0033. The numerical computations were done using the resources of the Advanced Research Computing center at Virginia Tech.

Dedication

Dedicated to my roots, my family and my beloved.

Acknowledgments

> "The banks of the river are arched, the river meanders and the water is serpentine. I have rowed my boat through all kinds of bends and yet they are new to me every time".
>
> Jasimuddin

The above lines are a couplet from a regional folk Bangla song "*Amar har kala korlam re*" originally written by *Palli Kabi* Jasimuddin which I have translated into English. I believe the above lines closely reflect my thoughts, experiences and my journey so far in academic research. I have found academic research to be akin to a journey by a boat on meandering tropical waters in hitherto unknown terrains. While I have excitedly pushed for new results and new outcomes, I have found that even familiar routes have resulted in unexpected outcomes, similar to navigating through the seasonally varying waters and landmasses of tropical Bengal. I have found research to be of endless possibilities and fascinations and I am hopeful that this is just the beginning. The PhD journey has taught me not just about research but important life lessons which are both personal and political.

I would start by acknowledging the support of my advisor Professor Mark Paul throughout this journey. I am thankful to him for taking me under his wings and introducing me to this interesting problem of front propagation. It is easy to feel lost and clueless in research and I would like to thank him for providing important directions at crucial times. I have been able to tread through troubled waters with a necessary mix of tradition, process and transgression under his guidance. I have learnt valuable lessons on research, professionalism and scientific

writing from Professor Paul. I am grateful for his tremendous composure and patience when I have knocked his office door of 213 C Goodwin Hall innumerable times through the past three and a half years, often for asking rather stupid questions and suggesting crazy ideas regarding research but also perhaps sometimes for seeking positive validation and motivation. I have never left disappointed.

I would like to thank my academic committee starting with Professor Shane Ross. I have enjoyed our chats and discussions on nonlinear dynamics both inside and outside the classroom. I have always enjoyed honest talks on academia and research with Professor Mark Stremler. I loved being a part of the weekly meetings on nonlinear dynamics and fluids in Norris Hall during my first year in graduate school. Professor Sunny Jung has always been enjoyable to talk to whenever I have met him in campus or in APS meetings. I am thankful to each of Professor Ross, Stremler and Jung to be accommodating and honest during my research rotations in their groups in my first year of PhD studies. I have learnt a lot from each of you and have become academically more mature through the process. I would like to thank Professor Danesh Tafti for valuable insights and ideas on computations whenever I have interrupted his regular walks through the hallways of Goodwin Hall. I would like to thank Professor John Palmore for serving in my committee as a proxy for Professor Jung in such a short notice. I am thankful to the support staff and fellow graduate students of Engineering Mechanics program at Virginia Tech. The EM program is a unique program on its own with its stress on fundamental engineering problems. I hope this program continues to foster graduate students who seek to research on fundamental problems. I am thankful to my lab-mates in 224 Goodwin hall, Mu Xu and John Barbish for their feedback in practice talks for conferences and presentations in. I am grateful to Professor Mike Schatz and Professor Jorge Viñals for patiently writing and submitting reference letters for my job applications.

I am thankful to some friends in this quaint little town of Blacksburg. I thank Kedar, Peter,

Poorva, Kristen and other friends in the EM major. I am thankful to the 'old time' musicians Matt, Bob Stepno, Mike and Cara Gangloff who gather in the Downtown Farmer's market every Wednesday evening during the Fall and with whom I have often jammed. Fellow band members of 'Panda Bag', Han, Ayan, Wenhui, Gregg, Ethan and Sara - The songs that we wrote together will stay with me forever. I am thankful to our group 'Migratory Birds of Blacksburg' with whom I have spent enjoyable time performing Bangla regional folk songs and poetry. Mehrab, Swarna, Mahruf, Anik, Riifat, Srijan da, Aevelina, Sifat - I have enjoyed our occasional gatherings which were both musically and gastronomically soothing. I am thankful to 'Association for India's Development' for introducing me to different projects on the ground in India. One of the most beautiful experiences in my life was my stay in the drought-stricken tribal village of Amlasole and my interactions with Dr. Arup Roy and Somnath da. The joy that I felt in those two days in Amlasole, teaching science of rainfall to wide-eyed enthusiastic students will stay with me forever. I would thank Nath, Nob and others in the initiation of this journey and Padhi, Jana and Harsh, with whom I have chatted in length about movies, tv series, manga, cricket and frustrations of graduate school.

I would not be where I am without the support of my family. My father Mrityunjoy Mukherjee and my mother Manika Mukherjee have devoted their lives towards raising me and my sister. I remember our humble fiscal beginnings. I remember the struggles when we moved from one rented apartment to the other in hopes of a better life in Durgapur. Baba, I have learnt to be pragmatic from you. Ma, your sacrifices are immense and incomparable. I have learnt to dream from you. My sister Saheli has been a blessing and a source of inspiration in my life. I have always felt she is one of the handful of people with whom I share a spontaneous, instinctive connection. My studies have made me leave home for quite some time now. I am glad to witness how you have matured in my absence; how you have handled things inside and outside the house along with your studies. It is a privilege to watch you grow up, Saheli. You are an unstoppable force of nature. I will always be by your side.

I would like to acknowledge my late paternal grandparents Chittaranjan Mukhopadhyay and Bijoylakshmi Mukhopadhyay. Your grandson has left the small village of Palsona and is now traveling all over the world. I know you are watching me from somewhere. I would like to thank my maternal grandparents Anath Bandhu Banerjee and Gayatri Banerjee. Dadu has always been incredibly supportive in my education and development. He has always been keen to learn about my latest developments in research and in education. Didu has always made sure I have a full tummy whenever I have visited them in Keshiakole. Her handmade curry of yam and potatoes is the most delicious food that I will ever taste in my life. My identity has been moulded from the red soils of Bankura; my conscience has been shaped by the simple people of this land. My mind often seeks refuge in the colors and festivities of Charak, Horibol and Harinaam and Kirtan in Gaudiya Math. I have traversed across the spatiotemporal continuum in my mind when I have mapped the forests of the Appalachia with the highlands and dry, deciduous *Sal* forests of Bankura.

My initial love for science was due to my teacher Samima Khatun. I hope you are doing well wherever you are. I am thankful to my childhood friends namely Sohan, Debjit, Sudipto, Susobhan and others. I am thankful to my undergraduate days in Jadavpur University which has taught me so much more than engineering. Jadavpur campus has taught me to be unapologetic in seeking the truth, in questioning education, society and politics. My worldviews have been shaped by the conversations inside and outside classrooms, in *addas* over cha and cigarettes, in canteens and in the union room. I have made friends, fell in love and made many memories here. Abu, Pati, Sudeepto, Debnath, Saha, Anik, Ankita, Suman...and many more in JU main hostel and campus, thank you for your friendship during my undergraduate days. I thank the professors in Mechanical Engineering department of JU who introduced me to academic research and have always given me their best advice. Most importantly, I am indebted to Jadavpur for introducing me to my beloved.

No amount of appreciation is enough to quantify our relationship, Sreyashi. We have matured a lot through our times knowing each other in Jadavpur and through the course of our graduate education. My frequent visits to the Twin Cities has made the journey bearable. Our conjugal retreats to each of our respective cities have rejuvenated me and have made me see the larger picture of life, love and research. We have sought our liberation in each other. We have made memories that are carried across the spatiotemporal continuum by the New River bending around the Appalachian mountains, by the Mississippi river flowing past the theater district in Minneapolis, by the sleeping Damodar carrying industrial discharges in Durgapur and the Ganges flowing past the evening prayers of Mandirtala. I do not know what the future has in store for us, but I am hopeful. It is now your turn to cross the bridge. This is to our perpetual transgressions and our incompleteness. We are infinite.

I would like to end by acknowledging my inborn privileges. My first privilege is to be born as a man in an unequal society. Being a woman comes with innumerable challenges in a patriarchal world, which, me being a man would never experience from my privileged vantage point. I can only perhaps empathize with and understand from lived experiences of the women who are close to me. I would like to acknowledge my upper caste privilege that is associated with my surname in India. Even though we were not economically well off, being from an upper caste meant we had cultural capital. Science should be free and without prejudice. I wish for a day when the many Rohith Vemulas in India can dream of writing science like Carl Sagan and are not oppressed for pursuing their dreams. I wish for a day when our society will rise up from the narrow boundaries of religion, caste, gender and creed and cultivate empathy and rationality in their minds. Lastly, I would like to acknowledge the millions of health and sanitation workers who are at the front line dealing with Covid-19 as we sit in self-isolation. My thoughts are with them and with the poor and the marginalized who cannot afford self-isolation. I wish for kinder days.

Contents

List of Figures

List of Tables

List of Symbols

Dimensional quantities

α	Coefficient of thermal diffusivity ($\mathrm{m^2\,s^{-1}}$)
β	Thermal expansion coefficient ($\mathrm{K^{-1}}$)
β_s	Solutal expansion coefficient ($\mathrm{M^{-1}}$)
ΔH	Change in enthalpy from the reaction (kJ)
ΔT	Temperature difference between bottom and top wall of the domain (K)
μ	Coefficient of dynamic viscosity ($\mathrm{kg\,m^{-1}\,s^{-1}}$)
ν	Coefficient of kinematic viscosity ($\mathrm{m^2\,s^{-1}}$)
ρ^*	Density ($\mathrm{kg\,m^{-3}}$)
τ_α	Vertical diffusion time (s)
τ_h	Horizontal diffusion time (s)
$\vec{u}^*$	Fluid velocity ($\mathrm{m\,s^{-1}}$)
a_0	Initial concentration of the reactants (M)
c^*	Concentration of products (M)
c_p	Specific heat capacity ($\mathrm{J\,K^{-1}\,kg^{-1}}$)
D	Diffusion coefficient of the species ($\mathrm{m^2\,s^{-1}}$)

d Depth of the convection layer (m)

g Acceleration due to gravity ($\mathrm{m\,s^{-2}}$)

k_r Reaction rate ($\mathrm{M^{-1}\,s^{-1}}$)

L_c Chemical length scale (m)

L_x Length of the rectangular domain along the x-direction (m)

L_y Length of the rectangular domain along the y-direction (m)

p^* Pressure (Pa)

r_0 Radius of the cylindrical domain (m)

T^* Temperature (K)

t^* Time (s)

T_0 Temperature of a reference state (K)

T_c Temperature of the top wall (K)

T_h Temperature of the bottom wall (K)

Nondimensional quantities

α_b Scaling exponent for $\bar{D}_b$ as a function of Rayleigh number

α_f Scaling exponent for $\bar{v}_f$ as a function of U

$\bar{D}_b$ Time average of the reduced box counting dimension

$\bar{L}_s$ Time average of the mixing length

$\bar{U}$ Time average of characteristic fluid velocity

$\bar{U}_n$ Time average of U_n

$\bar{v}_f$ Asymptotic front velocity

$\Delta t_{\min}$ Minimum time step used

δ_0 No-flow front thickness

ϵ Reduced thermal Rayleigh number

ϵ_b Smallest size of boxes for box counting dimension

η heat release parameter

Γ Aspect ratio of the cylindrical domain

Γ_r The ratio of the fluid length scale to the front thickness

Γ_x, Γ_y Aspect ratios of the rectangular domain

λ Wavelength of the pattern forming front of convection rolls

λ_0 Parameter used for curve fitting λ with ϵ

λ_{eq} Wavelength of straight parallel rolls in the equilibrium configuration

λ_s Steepness of initial condition of the front solution

ω Vorticity

ϕ Reaction zone angle

ψ Stream function

ρ Density

σ Prandtl number

Da Damköhler number

Le Lewis number

Nu Nusselt number

Pe Péclet number

Ra Thermal Rayleigh number

Ra_c Critical thermal Rayleigh number

Ra_s Solutal Rayleigh number

Re Reynolds number

θ Azimuthal angle

θ_l Local orientation of convection rolls

$\tilde{\theta}$ Difference between the azimuthal angle and local orientation of convection rolls

$\vec{q} = (q_x, q_y)$ Wave vector of convection rolls

$\vec{u}$ Fluid velocity

ξ Reaction rate

c Concentration of the products

c_m Midplane profile of the concentration as a function of x

c_t Concentration as a function of time

D_b Box counting dimension

k Wavenumber of convection rolls

k_c Wavenumber of a chaotic pattern

k_t Wavenumber of target pattern produced by fronts with feedback in chaotic flow

L_0 Mixing length in no-flow

L_s Instantaneous mixing length

N Number of boxes for box counting dimension

N_g Number of Gauss-Lobatto-Legendre (GLL) polynomial points

$N_{g,\max}$ Maximum spatial resolution using GLL points

p Pressure

r_p Parameter describing the family of solutions for a reaction-diffusion front with the FKPP nonlinearity

T Temperature

t Time

U Characteristic fluid velocity

U_c Characteristic fluid velocity of convection in the absence of feedback

U_n Normalized characteristic fluid velocity using U_c

v_0 No-flow front velocity

v_f Instantaneous front velocity

v_r Instantaneous front velocity along a radial direction

v_{fp} Front velocity of a pattern forming front

$x_{\max}$ Maximum value of x of the front profile

$x_{\min}$ Minimum value of x of the front profile

x_c Center of the front profile

x_s x-locations in the space-time plots where slices are taken to quantify oscillations

x_t Traveling coordinate

Chapter 1

Introduction

Fronts are defined as moving interfaces between two distinct states in a system, such as products and reactants in a chemical reaction [1, 2]. Fronts separate regions in space which are of unequal amplitude and stability. Fronts are not only limited to chemical reactions but are ubiquitous, ranging from fronts in oceanic and atmospheric flows [3, 4], solidification fronts, biological invasion fronts [1, 2], spreading fronts of forest fires [5], polymerization fronts [6], combustion fronts of premixed gases in internal combustion engines [7] and the front of transition between laminar and turbulent flows [8] to name but a few. In these situations, the propagating front can be modeled as a reaction that consumes unreacted species (the unstable phase) in its path while leaving behind only products (the stable phase). Mathematically, a front is defined as a spatially localized solution which connects two solutions that represent states far away from the front. Fronts determine the long time evolution and dynamics of the system.

Front propagation is modelled using a class of equations known as 'reaction-diffusion' equations [1, 2]. The study of reaction-diffusion equations has a rich history. Reaction-diffusion equations were initially used to model the propagation of advantageous genes in a population [9, 10]. Reaction-diffusion equations have also been used to model the spread of epidemics, chemotaxis, population dynamics, wound healing, predator-prey systems and biological pattern formation, such as coat markings in many mammalian species and Turing patterns [1, 11, 12]. In many situations, the front is subjected to spatial variations during its propagation, such as a front propagating through an underlying flow field, which adds more complications. These situations are modelled using a class of equations known as 'reaction-advection-diffusion' (RAD) equations. The spatial coupling between the front and the underlying flow field can modify the geometry and dynamics of the propagating fronts in a complicated way. The front interface is directly affected by the spatial gradients of the flow field. Front propagation through a background flow field has received significant attention to understand the process of mixing and entrainment in turbulent fluid flow [13], outbreak of an epidemic such as the flu in a moving population [14], plankton blooms in the oceans [4], humidity fronts in the atmosphere [3], reactive mixing in microfluidics [15], cellular transport [16] and autocatalytic chemical reactions [17–19]. Additionally, in many situations, the front feeds back to the flow field to alter the spatial variation which can further alter the front dynamics. The feedback can be generated from the heat release from the reaction and from the differential densities between the products and the reactants after the reaction. The front in these scenarios creates its own flow field which interacts with the background flow in a complicated way. Front induced feedback has received significant attention to understand lock-exchange gravity waves in geophysics [20–22], reactive transport in the surface of stars [23] as well as engineering applications such as design of flow reactors, hydrocarbon oxidation and polymerization [6, 18].

In this dissertation, we will study front propagation through convective flow fields of varying spatial complexity. We will study front propagation through straight and parallel time-independent convection rolls, convection rolls undergoing defects, instabilities, spatiotemporal chaos and convection rolls undergoing weak turbulence. We will explore how these complicated convective flow fields alter the geometry and dynamics of propagating fronts. We will then explore how a propagating front feeds back to the underlying convective flow field resulting in rich and emergent dynamics such as spatiotemporal oscillations and pattern formation.

In many scenarios, fronts leave a trail of spatial structures behind as they propagate. This class of fronts are known as pattern forming fronts [1, 2]. Examples of such fronts are dendritic growth fronts, crystal growth fronts, dissolution fronts in rocks and flame fronts which leave cellular patterns on their wake [24, 25]. In this dissertation, we will study pattern forming fronts of convection which leave a trail of convection rolls behind as they propagate. We will encounter pattern forming fronts of convection rolls in the wake of a front propagating with thermal and solutal feedback. Overall, we will probe the following questions,

1. How do nonlinear reaction-advection-diffusion fronts propagate in Boussinesq convection?
2. How does spatio-temporally chaotic convection affect the front propagation?
3. What happens when the fronts feed back to the Boussinesq flow field?
4. What are the velocity and wavelength selected by a pattern-forming front?

1.1 Front propagation in convective flow fields

There has been intense interest in the study of front propagation coupled with the underlying fluid motion because of its relevance to a myriad of physical, chemical, engineering and biological problems. There has been a range of studies on fronts that are propagating through simplified flow fields such as an idealized chain of vortices [26–30], a shaken layer of liquid exhibiting Faraday waves [31], Marangoni flows [32, 33] and Hele-Shaw flows [34, 35] to obtain a fundamental understanding of RAD fronts. An overall aim of studying front propagation through simplified flow fields is to understand fundamentally how the spatial variations of a flow field affect the front dynamics. A simplified two dimensional model of fluid flow helps in the quantification of the front dynamics using fewer system variables such as the details of the stream function and the details of the nonlinear reaction. In many such cases, the front velocity of propagation has been shown to vary as a power law of the fluid velocity [26, 27]. The power law behavior has been established using theoretical predictions for some limiting scenarios where the reaction is weak compared to the flow field strength or where the front interface is sharp due to strong reaction and advection. Many important theories on front velocity, geometry and orientation in simplified flow fields have been developed. For sharp front interfaces, it has been shown that there are dynamically defined barriers in the system space which guide the front evolution in flow fields. These barriers, named 'burning-invariant-manifolds' [28, 29, 36] are one-way and invariant in nature such that the front cannot propagate in the opposite direction into the manifold.

An important property for quantifying the relation between the front and fluid dynamics is the front velocity. The front velocity is often difficult to quantify because of disintegrated front interfaces in disordered flows which make tracking of the front unfeasible. In these scenarios, rigorous mathematical definitions of front velocity such as the 'bulk burning-rate' [37] have been found to be quite useful. We will find this approach particularly convenient to quantify the velocity of fronts and fronts with feedback in convective flows which make the front interface disordered and complicated [38, 39].

The majority of work on front propagation coupled with fluid flow, however has been in idealized and two-dimensional fluid flows such as cellular flows, vortex chains and vortex arrays, which can be represented with stream-functions. In the present dissertation, we explore a more difficult problem of front propagation in spatially nonuniform and time-dependent flow fields along with time-independent cellular flow fields and quiescent flow fields. We use the canonical pattern-forming system known as Rayleigh-Bénard convection as our flow field [2]. We use experimentally realizable domains and boundary conditions for simulating the front and fluid dynamics. We use a highly efficient and scalable spectral element fluid solver called NEK5000 [40] to solve the resulting front and fluid dynamics.

Rayleigh-Bénard convection is the buoyancy-driven fluid motion that occurs when a shallow layer of fluid is heated uniformly from below against the gravitational field. When an initially quiescent layer of fluid is heated from below, after crossing a certain critical temperature difference between the bottom and the top wall, the fluid becomes unstable and gives rise to convection rolls. The linear conduction profile of the fluid in this case becomes convectively unstable through a pitchfork bifurcation [2, 41]. A further increase in temperature difference gives rise to complicated spirals and defects in the convection rolls inducing a state called spiral defect chaos [42]. A further increase in temperature difference induces oscillatory instabilities in the convection rolls. The convection rolls then give rise to plumes and undergo a route to turbulence.

Rayleigh-Bénard convection is an experimentally accessible system, which makes it extremely attractive for studying chaos and nonlinear dynamics. Moreover, the system can be described using a modified form of the incompressible Navier-Stokes equations, which makes it extremely accessible for theoretical and numerical studies. Rayleigh-Bénard convection is a canonical example of pattern formation in a dissipative nonequilibrium system. The emergence of spatial structures such as convection rolls when a system is driven far from thermodynamic equilibrium falls under the umbrella of nonequilibrium pattern formation theory, which describes the mechanisms behind morphogenesis, cell-division, self-organization of chemical compounds to form life to other physical phenomena such as the coat-markings of zebra, the structure of sand dunes in deserts, the aggregation of slime-mold colonies and even the formation of spirals in galaxies [2].

Because of its inherent accessibility, there have been extensive theoretical, numerical and experimental investigations on Rayleigh-Bénard convection, aimed at understanding open questions on chaos and turbulence [43–45]. Recent focus has been on the quantification of spatiotemporal chaos in Rayleigh-Bénard convection using nonlinear dynamical tools such as the covariant Lyapunov vectors [46] and Kaplan-Yorke dimension [47, 48]. The overall aim of these studies is to quantify invariant manifolds in the state-space of the system and identify regions in the state-space that have high magnitude of growth when subjected to small perturbations. Mathematical pattern-diagnostic tools such as persistent homology [49] have also been used in this regard to establish the relation between observed patterns such as spirals, plumes and defects, with regions of large Lyapunov growth [50]. Rayleigh-Bénard convection is also directly related to natural convective processes such as atmospheric convection, mantle convection and stellar convection [51–53]. An understanding of front propagation in complex convective flow fields is thus important to understand material transport in such systems.

Figure 1.1 shows schematics of domains which contain fluid that is undergoing Rayleigh-Bénard convection. The red regions indicate locations where an autocatalytic reaction has been initiated. A shallow layer of fluid is confined inside a cylinder shown in Fig. 1.1 (a) and a rectangular domain shown in Fig. 1.1 (b). The fluid is subjected to a temperature difference, $\Delta T = T_h - T_c$ against the gravity, with the bottom plate at temperature T_h and the top plate at temperature T_c. The depth of the fluid layer, d, is sufficiently small compared to the spatial extent of the layer, which is an important feature of pattern formation in dissipative and nonequilibrium systems [2, 41]. The aspect ratio, Γ, of the domain is defined as the ratio of the radius to depth for the cylindrical domain, that is $\Gamma = r_0/d$, where r_0 is the radius of the cylinder. For the rectangular domain, the aspect ratio is defined as the ratio of the length of sides to the depth, $\Gamma_x = L_x/d$ and $\Gamma_y = L_y/d$, where L_x and L_y are lengths of the sides aligned with the x and y axes, respectively. After a certain critical temperature difference, we get convection rolls in the domain. The convection rolls observed are in the form of straight-parallel rolls, spirals and other complicated patterns for a range of values of ΔT.

As we will observe from the governing equations in Ch. 2, when nondimensionalized with the depth of the fluid layer as the length scale and the vertical diffusion time as the time scale, the governing equations provide us with two important control parameters, the thermal Rayleigh number, Ra, and the Prandtl number, σ. The thermal Rayleigh number, from herein referred to as simply the Rayleigh number, is the ratio of buoyancy to dissipation and is defined as,

$$\mathrm{Ra} = \frac{\beta g \Delta T d^3}{\alpha \nu}. \tag{1.1}$$

Here, β is the thermal expansion coefficient, α is the thermal diffusivity and ν is the kinematic viscosity. For an infinite layer of fluid, the critical Rayleigh number at the onset of convection is $\mathrm{Ra}_c = 1707.76$ [2, 41]. As the Rayleigh number is increased, an initially quiescent layer of fluid gives rise to time-independent convection rolls at $\mathrm{Ra} = \mathrm{Ra}_c$. Further increase in the Rayleigh number results in time-dependent dynamics, period doubling, chaos and finally turbulence. We will find it useful to represent the dynamics using the reduced Rayleigh number, which is defined as $\epsilon = (\mathrm{Ra} - \mathrm{Ra}_c)/\mathrm{Ra}_c$. The Prandtl number is defined as the ratio of momentum and thermal diffusivity,

$$\sigma = \frac{\nu}{\alpha}. \tag{1.2}$$

For all our simulations, we fix the Prandtl number at $\sigma = 1$, which is typically found in compressed gas Rayleigh-Bénard convection experiments [43]. A higher value of Prandtl number ($\sigma \approx 7$) is required to simulate front propagation in an aqueous medium. However a higher value of Prandtl number weakens the spiral defect chaos state of the convection rolls by damping the *mean flow* in the domain [2]. In this text, we have kept $\sigma = 1$ to quantify front propagation through spatially disordered and chaotic convective flow fields.

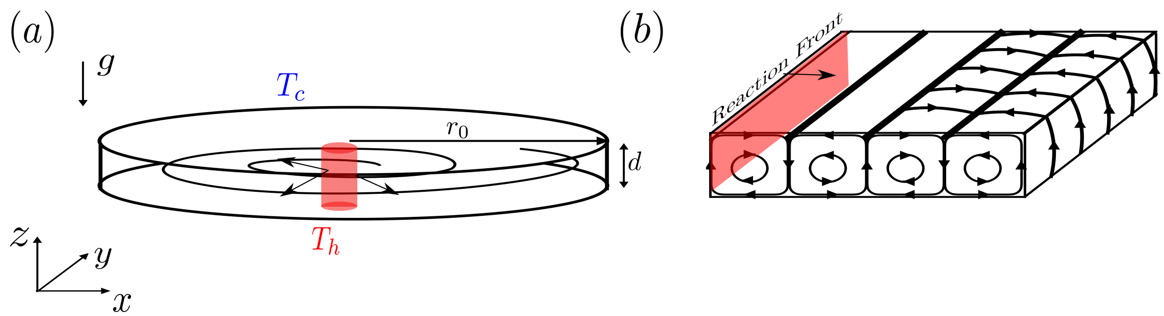

Figure 1.1: Schematics of the computational domains used to study front propagation in Rayleigh-Bénard convection. (a) A cylindrical domain of radius r_0 and depth d. The hot bottom and the cold top wall are maintained at temperature T_h and T_c. The schematic shows a spiral that has been formed by the convection rolls. The red region is a blob where a reaction has been initiated. This reaction will result in a front that will propagate radially towards the boundaries of the domain, until all the reactants in the domain are consumed. (b) A schematic of a rectangular domain with straight parallel, counterrotating convection rolls. The arrows indicate the direction of fluid flow. A reaction has been initiated at the left wall of the domain. This reaction will generate a front that will travel towards the right wall indicated by a arrow.

Previous works on material transport in Rayleigh-Bénard convection and other spatiotemporally disordered flow fields have focused mainly on passive scalars or tracers in the flow. An enhancement in the effective diffusion coefficient of passive tracers in convective flow fields was found [54, 55]. The diffusion coefficient was found to be enhanced by a factor of $\mathrm{Pe}^{1/2}$ in two-dimensional convective flow fields, where Pe denotes the Péclet number, which is the ratio between convection and mass diffusion. The study was extended further by a direct numerical simulation of an advection-diffusion equation in three-dimensional, time-dependent Rayleigh-Bénard convection [56]. It was found that the diffusion enhancement was linear with the Péclet number for larger values of Pe and behaved as the square root of the Péclet number for smaller values of Pe. The complex dependence of the tracer transport with the defects and orientation of the flow field was also investigated. Active transport in Rayleigh-Bénard convection was then studied by solving a reaction-advection-diffusion equation coupled with three-dimensional Rayleigh-Bénard convection in the presence of spatiotemporal chaos [57]. The enhancement of the spreading rate of the front in spatiotemporally chaotic flow fields was quantified as a function of the flow field disorder [57, 58]. The study of propagating reacting fronts in a two-dimensional turbulent flow field was done by Ref. [59], where it was found that the multiscale character of a turbulent flow field enhanced the bulk burning rate and the complexity of the reaction front interface. A reacting Belousov-Zhabotinsky front in an array of fluid rolls was studied in Ref. [60] where it was found that reacting fronts travelled towards the core of the vortex rolls in the presence of a flow field unlike a nonreactive scalar. The *blow-out* of a reaction due to a strong flow field was also quantified using an optimal stretching tensor.

A thorough investigation of front propagation in a range of convective flow fields from time-independent straight parallel rolls to time-dependent chaotic rolls and weakly turbulent rolls was done by Ref. [38]. It was found that chaos and instabilities in convective flow fields can impart rich spatiotemporal dynamics and fractal geometry to the front interface. It was shown that front propagation is highly affected by the spirals and defects in the Boussinesq flow field. It was found that convection rolls which are undergoing spiral defect chaos can impede front propagation and make fronts slower than time-independent cellular convection rolls. When the Rayleigh number was increased, eventually the front velocity in chaotic convection was found to be faster than time-independent cellular convection rolls. It was reported that this transition occurred when the convection rolls undergo an oscillatory instability, which imparts a fractal geometry to the front interface. Different mathematical and computational tools were used to quantify front velocity, fractal dimension and front angles. The details of this work can be found in Ch. 5 of the present dissertation.

1.2 Front induced feedback to convection

In many scenarios, the propagating front can affect the flow field, generating a feedback mechanism. Reactions which are exothermic and where the products and reactants are of different densities can feedback to the underlying flow field [18, 61]. Under such scenarios, the reaction-advection-diffusion equation creates a local flow field traveling with the front that can interact with the underlying convective flow field. Reactions that are exothermic cause a local increase of the temperature at the reaction zone which creates fluid rolls that travel with the front. This feedback is called a thermal feedback from the reaction. On the other hand, a change in chemical composition after the reaction can induce fluid flow driven by the density difference between products and reactants, a situation known as solutal feedback.

Solutal and thermal feedback are important aspects in many aqueous chemical reactions such as the iodate-arsenous acid (IAA) reaction and Belousov-Zhabotinsky reaction [17, 32, 61–65]. Front induced feedback to the flow field is important to understand the lock-exchange instability of geophysical and industrial applications [20], propagation of polymerization fronts [6] and propagating forest fire fronts [5]. Front induced feedback has received significant attention in autocatalytic chemical reactions, where chemical fronts traveling through capillary tubes have been found to induce convection [17, 19, 62, 63]. In autocatalytic chemical reactions, one of the reactants acts as a catalyst for itself and the reactants are completely converted to products. Autocatalytic chemical reactions can be second order or third order of type ($A + B \rightarrow 2B$) or ($A + 2B \rightarrow 3B$) respectively, where A and B are the two species of the reaction. A second order autocatalytic chemical reaction in an aqueous media can be modeled as a reaction-advection-diffusion equation with a quadratic nonlinearity. The class of reaction-diffusion equations with quadratic nonlinearities are named

Fisher-Kolmogorov-Petrovskii-Pishkunov equation after Fisher who studied this equation to model the propagation of advantageous genes in a population [9] and Kolmogorov, Petrovskii and Pishkunov who studied the equation simultaneously in Russia [10].

There have been a range of experimental investigations in channels, Petri dishes and Hele-Shaw cells that have shown front speed enhancement due to the feedback induced flow field [17, 19, 21, 66]. Autocatalytic front induced feedback has been suggested as a mechanism of plume formation and pinch-off events in geophysics and astrophysics [23, 66, 67]. Autocatalytic plume propagation and pinch-off in a vertical geometry, against gravity, for an IAA reaction was studied in Refs. [66, 67] where the different spatial structures such as heads and tails of autocatalytic plumes were quantified using viscous and reactive time scales. There have been many numerical investigations of front propagation with feedback in an initially quiescent fluid. The front speed enhancement due to convective motion in capillary tubes was quantified by Ref. [68] using a two-dimensional truncated Galerkin approach. Horizontally traveling fronts with solutal feedback coupled with a Stokes flow were numerically explored by Ref. [64]. It was found that the reactive mixing length and velocities scaled with the square root of the solutal Rayleigh number. It was also reported that the fluid velocity profiles exhibited self-similar behavior.

Horizontally traveling fronts with both solutal and thermal feedback were explored in Refs. [61, 69]. There are two separate scenarios that are possible when both solutal and thermal feedback are present in combination. The contribution to the density jump across the front interface due to the solutal and thermal feedback can either be positive, a scenario known as *cooperative* feedback, or the contributions can be of opposite signs, a scenario known as *antagonistic* feedback. The reactive mixing length and velocities for cooperative and antagonistic feedback were quantified by Ref. [61] using a Stokes flow. It was observed that the antagonistic scenario exhibited chemical oscillations with time. A detailed quantification of the effect of the solution layer to the system dynamics of fronts with feedback was done by Ref. [69] using a combined experimental and computational approach. Autocatalytic fronts have been shown to affect the surface tension gradients of flows in uncovered horizontal layers of fluid inducing Marangoni driven flows [17, 32]. A detailed review of chemical reaction triggered flows can be found in the PhD dissertation of Rongy [19]. An important objective of studying front induced feedback is to design conditions of chemically induced convection where the control of nonlinear dynamics, oscillations and complex behaviors can be achieved. A recent study has shown that chemical oscillations can be induced and controlled in a second order chemical reaction by simple hydrodynamic coupling [70]. A detailed review of chemo-hydrodynamic coupling induced patterns and instabilities can be found in Ref. [71] where chemical reaction induced flows due to viscosity and density gradients have been reviewed.

Although there has been a significant amount of literature in front induced feedback to the flow, most of these works have been in two dimensions and are limited to using a Stokes flow to model the induced flow field. The majority of studies on front induced feedback have not quantified the effect of front induced feedback flow in the presence of background fluid motion. Moreover, most of these works have also used third order autocatalytic chemical reactions which is a model for the IAA reaction. The interaction of front induced flow with an array of convective rolls generated by Rayleigh-Bénard convection using a second order autocatalytic reaction was studied by Ref. [39]. In the absence of convection rolls, for small values of solutal Rayleigh numbers, a perturbation expansion was used which revealed that the fluid velocity scaled linearly while the front velocity and the reactive mixing length scaled quadratically, with the increasing solutal Rayleigh number. At larger values of solutal Rayleigh number, the square root dependence of the velocities and the reactive mixing length with the solutal Rayleigh number was established which was consistent with previous studies of front induced feedback from a third order autocatalytic reaction in a Stokes flow [64]. A direct implication of front induced feedback is the temporal oscillations of the reacting species due to the nonlinear interactions of the reacting species and the flow [19, 70]. Recently, it was reported that the solutal feedback in underlying Rayleigh-Bénard convective flow can also induce chemical oscillations in the reacting species [39]. It was also found that the presence of background convection decreased the reactive mixing length but increased the front velocity. The results from this paper can be found in Ch. 6 of the present dissertation.

The complex interaction of a front propagating with the combined effects of solutal and thermal feedback with background convection has been reported in Ch. 7 of the dissertation. We first study fronts with only thermal feedback where we make scaling arguments for the front and fluid velocity. Next, we study fronts with *cooperative* and *antagonistic* feedback in a two-dimensional horizontal layer of fluid undergoing Rayleigh-Bénard convection. We then study fronts with feedback in three-dimensional Rayleigh-Bénard convection, where the underlying fluid is undergoing spatiotemporal chaos. We discuss the spatiotemporal features of the complex fronts in Rayleigh-Bénard convection that form over a range of solutal and thermal driving.

1.3 Thesis layout

We briefly describe the overall layout of the present dissertation. We first state our overall approach and methodology for computing reaction-advection-diffusion fronts and fronts with feedback in convective flow fields. This includes a discussion of our computational methodology, governing equations and the diagnostic tools to quantify front propagation. We then study fronts and front induced feedback in convective flow fields over a range of parameters and spatial disorder of the flow field. We start by stating our governing equations, nondimensionalization scheme and boundary conditions in Ch. 2. We introduce the relevant parameters of feedback and discuss the modifications in the governing equations to realize front induced feedback. Next, we develop the diagnostic tools that we use to quantify front propagation and to probe the nonlinear dynamics in Ch. 3. We discuss our numerical approach including temporal and spatial resolutions of the code in Ch. 4. We next describe our results. We study propagating fronts in a range of spatially varying convective flow fields in Ch. 5. We compare fronts propagating through straight parallel rolls, chaotic convection rolls and weakly turbulent rolls. We next study the effect of feedback from the front on the flow field by solving an exothermic reaction where the products and reactants vary in density. We study fronts propagating through flow fields with only solutal feedback in Ch. 7. For this case we solve a reaction which is isothermic and the only feedback from the reaction is due to the products and reactants being at different densities. We then study fronts propagating through flow fields with combined thermal and solutal feedback from the reaction in Ch. 7, where the combined feedback can act cooperatively or antagonistically in reducing the density of the fluid. In the presence of convection rolls, fronts with feedback annihilate the convection rolls ahead of it which results in convection rolls reemerging behind the front. This is an example of a pattern forming front where the reemerged convection rolls form more rolls to fill the void left behind by the front. We will study convective pattern forming fronts in Ch. 8, where we study how a chain of fluid convection rolls propagate at different thermal driving near the convective instability and quantify the front velocity as well as the wavelength of the pattern left behind. Lastly, we present our concluding remarks in Ch. 9.

Chapter 2

Governing equations

In this chapter we discuss the governing equations, our nondimensionalization scheme and the boundary conditions. We consider an incompressible shallow horizontal layer of fluid undergoing buoyancy driven convection. We then initiate an autocatalytic reaction in the fluid which results in a propagating reaction front. We solve the associated nondimensional incompressible Navier-Stokes equations and the coupled reaction-advection-diffusion equation.

When an incompressible layer of fluid is heated from below, the convective instability of the fluid layer can be modelled using the Boussinesq approximation. The Boussinesq approximation assumes the density to be constant everywhere except for the forcing term in the momentum equation. The density is expanded as a Taylor series in the temperature difference and only the terms up to the first order are retained. The Boussinesq approximation states,

$$\frac{\rho^*}{\rho_0} = 1 - \beta\left(T^* - T_0\right), \tag{2.1}$$

where ρ^* is the dimensional density and T^* is the dimensional temperature of the fluid. ρ_0 and T_0 are the density and temperature of a reference state and $\beta = -\frac{1}{\rho_0}\frac{\partial \rho^*}{\partial T^*}$ is the coefficient of thermal expansion.

2.1 Incompressible Navier-Stokes equation

The conservation equations of mass, momentum and temperature are,

$$\frac{\partial \vec{u}^*}{\partial t^*} + \vec{u}^* \cdot \vec{\nabla}^* \vec{u}^* = -\frac{1}{\rho_0}\vec{\nabla}^* p^* + \nu {\nabla^*}^2 \vec{u}^* - \frac{\rho^*}{\rho_0} g\hat{z}, \tag{2.2}$$

$$\frac{\partial T^*}{\partial t^*} + \vec{u}^* \cdot \vec{\nabla}^* T^* = \alpha {\nabla^*}^2 T^*, \tag{2.3}$$

$$\vec{\nabla}^* \cdot \vec{u}^* = 0. \tag{2.4}$$

Here $\vec{u}^*$ is the dimensional fluid velocity, p is the pressure, α is the thermal diffusivity, ν is the kinematic viscosity and g is the acceleration due to gravity. Using the Boussinesq approximation in Eq. 2.1, the momentum Eq. 2.2 can be rewritten as,

$$\frac{\partial \vec{u}^*}{\partial t^*} + \vec{u}^* \cdot \vec{\nabla}^* \vec{u}^* = -\frac{1}{\rho_0}\vec{\nabla}^* \tilde{p} + \nu {\nabla^*}^2 \vec{u}^* + \beta g T^* \hat{z}, \tag{2.5}$$

where, $\tilde{p} = p^* + \rho_0 g z^* + \rho_0 \beta g T_0 z^*$, is obtained by including all the constant terms inside the gradient operator of the pressure field.

We nondimensionalize the incompressible Navier-Stokes equations given by Eqs. 2.2-2.5 and apply the Boussinesq approximation shown in Eq. 2.1 to obtain our final equations. We use the depth d of the convection layer as length scale and vertical diffusion time $\tau_\alpha = d^2/\alpha$ as the time scale. $\Delta T = T_h - T_c$, which is the temperature difference between the top (at T_c) and bottom plate (at T_h) is used as the temperature scale. We specifically use the following operations to go from dimensional to nondimensional formulation, $t^* = t\tau_\alpha$, $d\nabla^*() = \nabla()$, $\vec{u}^* = \vec{u}\alpha/d$ and $T^* = T\Delta T$ and write our nondimensional equations as,

$$\sigma^{-1}\left(\frac{\partial \vec{u}}{\partial t} + \vec{u} \cdot \vec{\nabla}\vec{u}\right) = -\vec{\nabla} p + \nabla^2 \vec{u} + \mathrm{Ra} T \hat{z}, \tag{2.6}$$

$$\frac{\partial T}{\partial t} + \vec{u} \cdot \vec{\nabla} T = \nabla^2 T, \tag{2.7}$$

$$\vec{\nabla} \cdot \vec{u} = 0. \tag{2.8}$$

The nondimensional set of fluid equations given by Eqs. 2.6-2.8 are governed by the Rayleigh number Ra and Prandtl number σ which are defined in Eqs. 1.1 and 1.2 respectively. We explore a range of Rayleigh numbers $0 \leq \mathrm{Ra} \leq 25000$ which generates a range of different convective flow fields from straight parallel convection rolls to spatiotemporally chaotic and weakly turbulent rolls. We use a Prandtl number of $\sigma = 1$ which is typically used in Rayleigh-Bénard convection experiments with compressed gases. However, our computational approach is flexible and it would be straightforward to explore other parameter values such as a larger Prandtl number of $\sigma \approx 7$ to align with aqueous experiments, if desired [18, 63].

2.2 Reaction-Advection-Diffusion equation

We initiate a second order autocatalytic reaction with a reaction rate of k_r, which is coupled with the flow field. We initiate a second order reaction in our domain which contains an initial concentration of reactants a_0. The dimensional reaction-advection-diffusion (RAD) equation coupled with the flow field is,

$$\frac{\partial c^*}{\partial t^*} + \vec{u}^* \cdot \vec{\nabla}^* c = D {\nabla^*}^2 c + k_r c^* (a_0 - c^*). \tag{2.9}$$

Here, c^* is the concentration of the products in a second order autocatalytic reaction. D is the coefficient of molecular diffusion of the species, and k_r is the reaction rate. To obtain the nondimensional reaction-advection-diffusion equation, we use the same length and time scales used to nondimensionalize the Navier-Stokes equations. We then use the initial concentration of the reactants a_0 to nondimensionalize the concentration of the products. We write the nondimensional RAD equation as,

$$\frac{\partial c}{\partial t} + \vec{u} \cdot \vec{\nabla} c = \mathrm{Le} \nabla^2 c + \xi c(1 - c). \tag{2.10}$$

The nondimensional RAD equation is coupled with the nondimensional flow field equation given in Eq. 2.6. c is the normalized concentration of products such that the state $c = 1$ is the state of pure products and the state $c = 0$ is the state of pure reactants. The intermediate state of $0 < c < 1$ is a mixture products and reactants. The front is mathematically defined as the level set of $c = 1/2$. The reaction-advection-diffusion equation given in Eq. 2.10 governs the propagation of a front that propagates until all the reactants given by $c = 0$ are converted to the products given by $c = 1$. The reaction-advection-diffusion equation represents the time evolution of the concentration of the species which is reacting and is advected by a flow field $\vec{u}$.

The two important nondimensional parameters in Eq. 2.10 are the Lewis number Le, and the nondimensional reaction rate ξ. The Lewis number is the ratio of mass diffusion to heat diffusion $\mathrm{Le} = D/\alpha$. Here, D is the coefficient of molecular diffusion of the species. Decreasing the Lewis number results in stronger effect of the fluid flow on the front dynamics. The nondimensional timescale of mass diffusion is expressed as $\tau_D = \mathrm{Le}^{-1}$. We will use Lewis number values of $\mathrm{Le} = 1$, $\mathrm{Le} = 0.1$ and $\mathrm{Le} = 0.01$ in this dissertation.

The nondimensional reaction rate is defined as the ratio of the flow and the reaction time scales. $\xi = \tau_\alpha/\tau_r$, where τ_α is the vertical diffusion time scale used to nondimensionalize the flow field equations Eqs. 2.6-2.8. $\tau_r = (k_r a_0)^{-1}$ is the reaction time scale. Unless otherwise stated, we will fix our nondimensional reaction rate to a value of $\xi = 9$ which means that the time scale of vertical diffusion of heat is nine times slower than the reaction time scale.

This particular value for the reaction rate is chosen such that the reaction and flow field have comparable strength. The ratio of the reaction rate to the characteristic fluid velocity is known as the Damköhler number $\mathrm{Da} = \xi/U$ which we will study in greater detail in Ch. 3. A reaction rate of $\xi = 9$ ensures that $\mathrm{Da} \sim \mathcal{O}(1)$ and the fronts propagate with a finite velocity. Our computational approach is quite general and we can easily change our reaction rate. We show this by a comparison of front velocity with increasing reaction rates in Ch. 5.

2.3 Governing equations with front induced feedback

To realize front induced feedback, we recall that fronts can feedback to the the flow field in two key ways. The feedback can be solutal - a scenario when the products and the reactants of the autocatalytic reaction are of different densities and thermal - where the autocatalytic reaction is exothermic and releases heat. To realize the effect of a change in composition of the reacting species to a change in density, we use a generalized Boussinesq equation which takes into account the linear variation of density with changes in temperature and in concentration. A Taylor expansion of density in terms of the concentration field and temperature around a reference state yields,

$$\rho^* \left(c^*, T^*\right) = \rho_0 \left(a_0, T_0\right) + \frac{\partial \rho^*}{\partial c^*} \left(c^* - a_0\right) + \frac{\partial \rho^*}{\partial T^*} \left(T^* - T_0\right). \tag{2.11}$$

Here, ρ^*, c^* and T^* are the dimensional density, the dimensional concentration of products of the reaction, and the dimensional temperature, respectively. ρ_0 is the density of a reference state, a_0 is the initial concentration of reactants in the domain, and T_0 is the temperature of a reference state. We use the Boussinesq equation given by Eq. 2.11 to simplify the dimensional momentum equation Eq. 2.2 as,

$$\frac{\partial \vec{u}^*}{\partial t^*} + \vec{u}^* \cdot \vec{\nabla}^* \vec{u}^* = -\frac{1}{\rho_0} \vec{\nabla}^* \tilde{p} + \nu {\nabla^*}^2 \vec{u}^* + \beta g T^* \hat{z} + \beta_s g c^*, \tag{2.12}$$

where, $\tilde{p_s} = p^* + \rho_0 g z^* + \rho_0 \beta g T_0 z^* + \beta_s g a_0 z^*$, is obtained by including all the constant terms inside the gradient operator of the pressure field and $\beta_s = -\frac{1}{\rho_0}\frac{\partial \rho^*}{\partial c^*}$ is the solutal expansion coefficient.

To realize the effect of exothermic heat release from the autocatalytic chemical reaction, we use the chemical production term $f(c^*) = c^* (a_0 - c^*)$ in the dimensional energy equation such that,

$$\frac{\partial T^*}{\partial t^*} + \vec{u}^* \cdot \vec{\nabla}^* T^* = \alpha {\nabla^*}^2 T^* - \frac{\Delta H}{\rho_0 c_p} k_r c^* (a_0 - c^*). \tag{2.13}$$

Where, ΔH is the change in enthalpy from the reaction, which is negative for an exothermic reaction [18]. No autocatalytic endothermic reactions have been discovered as of now, however, our numerical procedure is quite general and we can investigate endothermic front propagation through a flow field in the future by simply changing the sign of the heat release term in Eq. 2.13.

The nondimensional governing equations of the flow field with front induced thermal and solutal feedback from the reaction-advection-diffusion equation given by Eq. 2.10 are,

$$\sigma^{-1}\left(\frac{\partial \vec{u}}{\partial t} + \vec{u} \cdot \vec{\nabla} \vec{u}\right) = -\vec{\nabla} p + \nabla^2 \vec{u} + \mathrm{Ra} T \hat{z} + \mathrm{Ra}_s c \hat{z}, \tag{2.14}$$

$$\frac{\partial T}{\partial t} + \vec{u} \cdot \vec{\nabla} T = \nabla^2 T + \eta c(1-c), \tag{2.15}$$

$$\vec{\nabla} \cdot \vec{u} = 0. \tag{2.16}$$

The two important nondimensional parameters that describe fronts with feedback to the underlying flow field are then,

1. The solutal Rayleigh number Ra_s which describes the change in density due to the change in chemical composition. The solutal Rayleigh number is given by the ratio between the buoyancy force generated due to compositional change to the dissipative force and is written as,
$$\mathrm{Ra}_s = \frac{\beta_s g a_0 d^3}{\alpha \nu}. \tag{2.17}$$
A positive value of Ra_s implies that the products are lighter than the reactants whereas $\mathrm{Ra}_s < 0$ implies heavier products after the reaction. We will explore a range of solutal Rayleigh numbers between $0 \le \mathrm{Ra}_s \le 8000$. Often in the physical chemistry literature, Ra_s is described using the chemical length scale $L_c = \sqrt{D\tau_r}$ instead of the depth of the fluid layer [19, 64]. For our parameters, the ratio of the depth of the fluid layer to the chemical length scale yields $d/L_c = \sqrt{\xi/\mathrm{Le}}$ which can be used to navigate between the two scaling and definitions.

2. The heat release parameter η which is given by,
$$\eta = -\xi \frac{\Delta H}{\rho_0 c_p \Delta T}. \tag{2.18}$$
Larger positive values of η implies larger heat release from the reaction which feeds back to the fluid flow. We explore a range of heat release between $0 \le \eta \le 100$. The heat release parameter is directly proportional to the reaction rate and the enthalpy change due to the reaction.

Different scenarios of front induced feedback are realized by different values of the thermal and solutal Rayleigh numbers, Ra and Ra_s, and the heat release parameter η.

Finally, using a characteristic density scale $\rho_c = \mu\alpha/(d^3 g)$, and converting the dimensional quantities to nondimensional quantities using the temperature and concentration scale, we get a nodimensional density given by,

$$\rho(c,T) = -\mathrm{Ra}_s c - \mathrm{Ra}T, \tag{2.19}$$

where ρ, c and T are nondimensional. Here, $\rho = (\rho_r - \rho_0)/\rho_c$, and $\rho_r = \rho^* - a_0\beta_s\rho_0 - T_0\beta\rho_0$. We tabulate the different scales used to arrive at the nondimensional set of equations Eqs. 2.14-2.16 in Table 2.1.

Quantity	**Scale**
Length	d
Time	$\tau_\alpha = d^2/\alpha$
Velocity	α/d
Temperature	ΔT
Concentration	a_0
Density	$\rho_c = \mu\alpha/(gd^3)$
Pressure	$\rho_c g d$

Table 2.1: List of scales used for nondimensionalization of different quantities in the governing equations given by Eqs. 2.14-2.16.

2.4 Boundary conditions

In general, we use no-slip boundary conditions $\vec{u} = 0$ for the fluid velocity at all material surfaces. The boundary condition for temperature is perfectly conducting on the sidewalls and is set to the conduction profile of $T(z) = 1 - z$. The bottom and top walls are held at $T(z=0) = 1$ and $T(z=1) = 0$. The boundary condition for the concentration is *no-flux* for all material surfaces, that is $\vec{\nabla}c \cdot \vec{n} = 0$, where $\vec{n}$ is the outward going normal from the material surface. In certain cases, we remove the walls and use periodic boundary conditions for all field variables.

Chapter 3

Front diagnostics

In this chapter we focus on tools and methodology by which we quantify front propagation. We start by studying the reaction-diffusion equation and quantifying front propagation in the absence of a flow field. We will explore the exact solutions and initial conditions of propagating fronts. We will then develop tools to quantify the different length scales and velocities associated with front propagation. The ideas we develop will be useful when quantifying fronts in the presence of convective disordered flow fields and fronts with feedback.

3.1 Front propagation in a quiescent flow field

We first study the propagation of reacting fronts in a quiescent flow field. In this scenario, the RAD equation given by Eq. 2.10 simplifies to a reaction diffusion equation given by Eq. 3.1 below with $\vec{u} = 0$.

$$\frac{\partial c}{\partial t} = \mathrm{Le}\nabla^2 c + \xi c\,(1-c)\,. \tag{3.1}$$

Reaction-diffusion equations such as Eq. 3.1 are used frequently in biological and ecological invasion models and bi-molecular chemical reactions [1, 18]. We will find this equation helpful to develop several mathematical and computational tools to quantify the complex front geometry and dynamics that we will encounter when fronts are subjected to flow fields and two-way feedback. Le is the nondimensional diffusion coefficient known as the Lewis number and ξ is the nondimensional reaction rate.

The concentration $c(x, y, z, t)$ is a single scalar quantity that represents the ratio of products to reactants where $c = 1$ is pure products (no reactants), $c = 0$ is pure reactants (no products), and intervening values $0 < c < 1$ represent a mixture of products and reactants. The front is mathematically defined as the $c = 1/2$ level set.

3.1.1 Initial conditions, *pulled* versus *pushed* fronts

Front propagation has a significant dependence on the initial conditions. Fronts can be classified as either *pulled* or *pushed* depending on the spreading speed that the propagating front selects [1]. Pulled fronts are fronts which propagate with a speed that is dictated by the linearized dynamics at the leading edge of the front around $c = 0$. In this case, equation Eq. 3.1 can be cast in a traveling wave formulation in one dimension and then linearized about the leading edge to obtain a linear spreading speed. The linear spreading speed is the asymptotic velocity attained by the fronts at large times. This approach is discussed in detail in Refs. [1, 72, 73]. For the FKPP type nonlinearity used in Eq. 3.1, we define the linear spreading speed as the no-flow front velocity, v_0 which is given by,

$$v_0 = 2f'(0)^{1/2}\sqrt{\mathrm{Le}\xi}, \tag{3.2}$$

where f is the reaction nonlinearity in Eq. 2.10 [1, 10]. For $f(c) = c(1-c)$, Eq. 3.2 yields $v_0 = 2\sqrt{\mathrm{Le}\xi}$.

On the other hand, pushed fronts are fronts where the nonlinearity is important. The front is pushed by the spatial region behind the leading edge where $0 < c < 1$ and the nonlinearity is significant. The spreading speed for pushed fronts is more than pulled fronts. A front can be categorized as either pulled or pushed depending on the *steepness* of the initial condition. A pulled front which develops from a sufficiently steep initial condition will select a spreading speed given by Eq. 3.2. The optimal steepness of the initial condition can be retrieved from casting the reaction-diffusion equation in a traveling wave formulation and then linearizing around the leading edge of the front. The fronts are initiated with an initial condition $c(x, y, z, t = 0) = e^{-\lambda_s x}$. The steepness of the initial condition is determined by λ_s. Any initial condition which is steeper than $\lambda_s = \sqrt{\xi/\mathrm{Le}}$, will generate a pulled front. Therefore, the minimum steepness of the initial condition for generating pulled fronts is given by,

$$c(x, y, z, t = 0) = e^{-\sqrt{\frac{\xi}{\mathrm{Le}}}x}. \tag{3.3}$$

Whereas, initial conditions flatter than Eq. 3.3 will generate a pushed front which will propagate with a larger velocity than Eq. 3.2. In this dissertation, for all the cases we consider, our initial conditions will be steeper than Eq. 3.3 and will generate pulled fronts that propagate towards the right in the rectangular domain or radially outward in the cylindrical domain, as shown in Fig. 3.1 (a),(b) and (d). Shown are the color contours of the normalized concentration of products c, with the color blue representing reactants at $c = 0$ and the color red representing products at $c = 1$. The intermediate green and yellow region represents the reaction zone containing the front. We will use this color scheme throughout the dissertation. For the cylindrical geometry, we will initiate a reaction at the center of the cylindrical domain with an initial condition of the form,

$$c(r, \theta, z, t = 0) = e^{-r^2}, \tag{3.4}$$

where r, θ and z are cylindrical coordinates. This results in a front moving radially outward as shown in Fig. 3.1 (d). The Gaussian initial condition given by Eq. 3.4 is always steeper than exponential initial conditions given by Eq. 3.3 and will always generate a pulled front.

3.1.2 Exact solutions

The FKPP nonlinearity used in Eq. 3.1 is given by $f(c) = c(1-c)$. Because of its quadratic nature, the FKPP nonlinearity has been used to model radial chain branching and bi-molecular oxidation reactions. The FKPP nonlinearity also arises in models of Belousov-Zhabotinsky reaction [18, 65]. For this nonlinearity, the system has two states of equilibrium at $c = 0$ and $c = 1$. It can also be seen that $f'(0) = 1 > 0$ while $f'(1) = -1 < 0$. A Taylor expansion near $c = 0$ suggests that this state is unstable. Thus, a pulled front propagating from $c = 1$ to $c = 0$ is always generated, with the aim of devouring the entire state into the stability of $c = 1$ [1]. The front will propagate until the entire state is at $c = 1$. For the quadratic FKPP nonlinearity, there is no general explicit solution for $c(x, y, z, t)$ and instead the exact solution is given by a family of solutions [72, 73]. For initial conditions which depend on one spatial dimension such as given by Eq. 3.3, we get a one parameter family of solutions given by,

$$c(x, y, z, t) = \frac{1}{[1 + r_p e^{(x_t/\sqrt{6})}]^2} \tag{3.5}$$

where x_t is the traveling coordinate given by $x_t = \sqrt{\xi/\mathrm{Le}}x - 2\xi t$ [72] and $r > 0$. Figure 3.1 (c) shows the excellent agreement between the front profile at the midplane in the rectangular domain $c_m(x) = c(x, y = \Gamma_y/2, z = 1/2)$ and the solution given by Eq. 3.5 at a time $t = 4$ from the start of the reaction. The parameter r_p for this particular case was found to be $r_p = 6.74$.

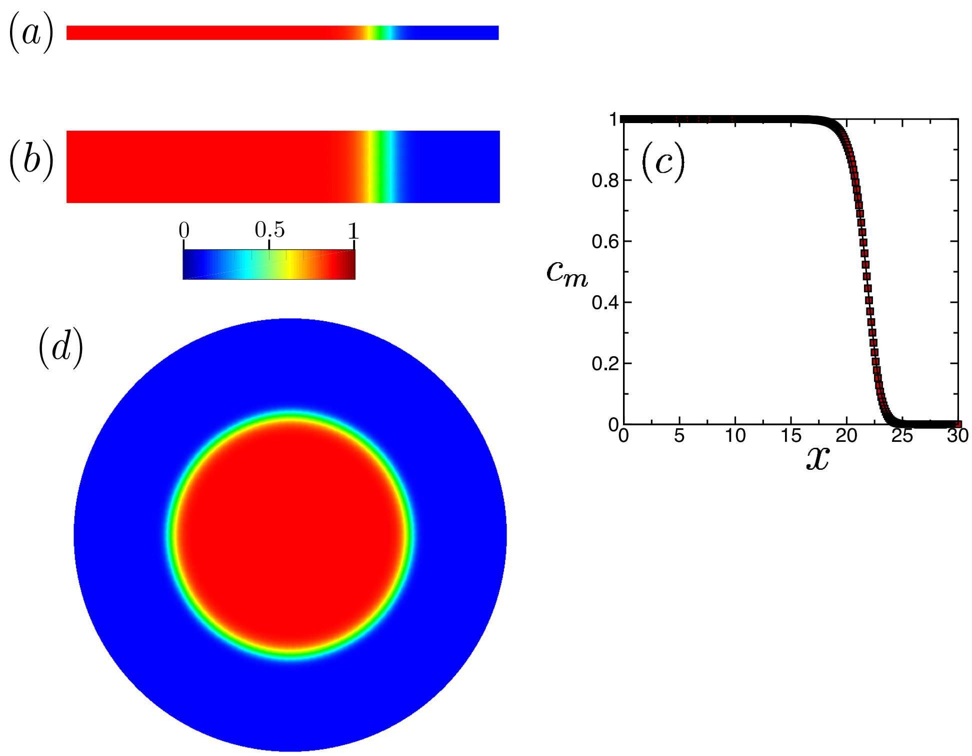

Figure 3.1: Front propagation in the absence of a background flow. The color contours are of the concentration where red is pure products ($c = 1$) and blue is pure reactants ($c = 0$). The intermediate green and yellow region indicates the reaction zone or loosely the front. (a) and (b) show a propagating front at Le $= 1$ and $\xi = 9$ in a rectangular domain as shown in Fig. 1.1 (b) with $\Gamma_x = 30$ and $\Gamma_y = 5$. The front is initiated at the left wall at $x = 0$ with the initial condition given by Eq. 3.3. (a) Propagating front in the x-z plane at a slice $y = \Gamma_y/2$. (b) Propagating front in the x-y plane at a slice $z = 1/2$. (c) Shape of the propagating front at a time $t = 4$ from the onset of the reaction as a function of spatial extent x taking the midplane slice of (a). Here the front profile in the midplane is written as $c_m(x) = c(x, y = \Gamma_y/2, z = 1/2)$. The red squares are the profile points and the solid black line is from the solution given in Eq. 3.5 with parameter $r_p = 6.74$. The curve-fit shows excellent agreement with the data. (d) Front propagating in a cylindrical domain shown in Fig. 1.1 (a) with initial condition given by Eq. 3.4. Shown is the horizontal midplane of a cylinder having an aspect ratio of $\Gamma = 40$.

3.2 Diagnostic tools

We quantify the front velocity using an integral known as the bulk burning rate [37, 74]. The front velocity using this approach can be quantified as,

$$v_f(t) = \int_0^1 dz \int_0^{\Gamma_x} dx \frac{\partial c}{\partial t}. \tag{3.6}$$

For fronts propagating through cylindrical domains with initial condition given by Eq. 3.4, the bulk burning rate equation gets modified as,

$$v_f(t) = \int_0^1 dz \int_0^{2\pi} d\theta \int_0^{\Gamma} dr \frac{\partial c}{\partial t}, \tag{3.7}$$

where θ is the azimuthal angle.

One of the properties of a pulled front is the slow asymptotic convergence of the front velocity with time. The front velocity scales algebraically as $\mathcal{O}(t^{-1})$ [1, 75]. We will call this long-time asymptotic velocity as $\bar{v}_f$. We will use an algebraic relation to fit our finite time data in order to quantify this slow convergence. This relation is given by,

$$\bar{v}_f = v_f(t) - b/t. \tag{3.8}$$

Because of the slow convergence of fronts, we are required to use large domains to quantify the front velocity properly. The fastest no-flow fronts with $\mathrm{Le} = 1$ and $\xi = 9$ had a no-flow front velocity of $v_0 = 6$ from Eq. 3.2. We found that a minimum spatial extent of $\Gamma_x = 30$ for this case yielded a limiting velocity of $v_f = 5.87$ which is in error of 2.17%. We then use the relation Eq. 3.8 to find the asymptotic front velocity $\bar{v}_f = 6.03$. Figure 3.2 shows the use of this method to determine the asymptotic front velocity. The blue circles in Fig. 3.2 are obtained from using the bulk-burning rate equation on a front propagating with the absence of flow in the rectangular domain and the black line through the data points is a curve-fit of the form Eq. 3.8.

An important property of the propagating front is the thickness of the reaction zone, loosely referred to as the front thickness. The front thickness is the thickness of the intermediate zone which consists of a mixture of products and reactants. The front thickness for pulled fronts in no-flow scales as $\delta_0 \sim \sqrt{Le/\xi}$ [10]. The front thickness for pulled fronts with the

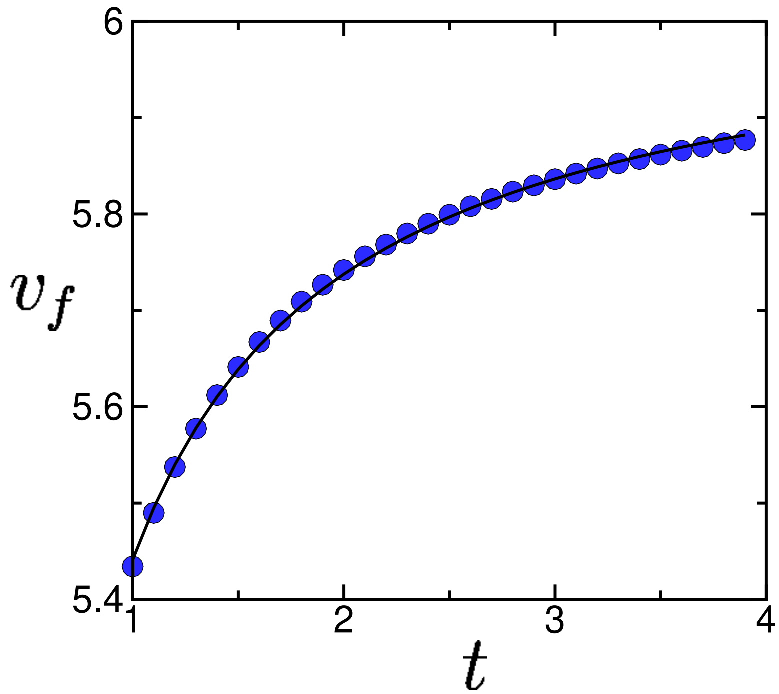

Figure 3.2: The time variation of front velocity $v_f(t)$ for Le $= 1$ and $\xi = 9$ for the fronts shown in Fig. 3.1 (a)-(c). The data is shown by the filled blue circles. The solid line is a curve fit Eq. 3.8. The curvefit yields $\bar{v}_f = 6.03$ and $b = 0.59$.

FKPP nonlinearity under no-flow conditions can be written as [30],

$$\delta_0 = 2\frac{f'(0)^{1/2}}{f(1/2)}\sqrt{\mathrm{Le}/\xi}. \tag{3.9}$$

For $f(c) = c(1-c)$, the front thickness becomes $\delta_0 = 8\sqrt{\mathrm{Le}/\xi}$ [27]. The front thickness represented by this equation represents a length scale where $0.1 \lesssim c \lesssim 0.9$ [38]. The reaction zone is the spatial region where $0.1 \leq c \leq 0.9$ which consists of a mixture of reactants and products.

A similar length scale, known as the 'mixing length' will be useful to quantify fronts with feedback in Ch. 6 and Ch. 7. In two-dimensional domains, the mixing length is defined using the vertical average of the concentration field

$$\langle c(x,t)\rangle = \int_0^1 c(x,z,t)dz. \tag{3.10}$$

The mixing length is defined as the distance between the x-location where $\langle c(x,t)\rangle = 0.01$ and $\langle c(x,t)\rangle = 0.99$ [64]. As we will find out in Ch. 6 and Ch. 7, this length scale correctly represents the length scale associated with stretched front interfaces that result from solutal and thermal feedback.

Lastly, to quantify the fluid velocity, we will use the characteristic velocity, U, defined as the time-average of the maximum velocity of the flow field. For fronts in three-dimensional domains, we use the midplane slice $z = 1/2$ to define U while for two dimensional domains, U equals the maximum fluid velocity magnitude in the two dimensional domain. In the presence of front induced feedback, we will find that it is insightful to represent the maximum fluid velocity using the spatial region equal to the mixing length around the front.

It is insightful to define the Reynolds number Re for the flow fields. Using the characteristic velocity U and our nondimensionalization yields the relationship $\mathrm{Re} = U/\sigma$. Since for us $\sigma = 1$, this yields $\mathrm{Re} = U$.

In addition to the Lewis number Le, and the nondimensional reaction rate ξ in Eq. 2.10, there are two more nondimensional numbers which will be useful to quantify the front and fluid dynamics. The Damköhler number is the ratio of the nondimensional flow time scale and the nondimensional reaction time scale and is given as $\mathrm{Da} = \xi/U$. Increasing the Damköhler number results in the increased reaction strength and the faster fronts which are not affected by the slower flow time scale. Throughout this text we use $\mathrm{Da} = \mathcal{O}(1)$, which ensures that the flow and the reaction time scales are comparable. The Péclet number is defined as the ratio of the nondimensional timescale of molecular diffusion of the species,

Le^{-1}, to the nondimensional flow time-scale, U^{-1}, and it is written as $\text{Pe} = U/\text{Le}$. Larger Péclet numbers imply a larger effect of the fluid flow on the front dynamics while smaller Péclet numbers imply smaller diffusion time scales and faster fronts which are less affected by the underlying fluid motion.

There have been significant theoretical insights into the two limiting regimes of fast reaction and fast advection ($\text{Da} \gg 1, \text{Pe} \gg 1$) and slow reaction and fast advection ($\text{Da} \ll 1, \text{Pe} \gg 1$). For $\text{Da} \ll 1, \text{Pe} \gg 1$, since the diffusion timescale is faster than the reaction timescale, the RAD equation can be replaced by an effective reaction-diffusion equation with enhanced diffusion coefficient. On the other hand, for $\text{Da} \gg 1, \text{Pe} \gg 1$, the reaction time scale is faster which leads to a renormalization of the time scales [26, 27]. The front thickness δ_0 is smaller compared to the length scale of the flow in the fast reaction limit. The fast reaction limit is thus conducive for theoretical analysis such as an eikonal approximation [76] or burning-invariant-manifold theory [28, 36]. Specifically in this limit the ratio of the fluid length scale to the front thickness Γ_r is large. $\Gamma_r \gtrsim 1000$ is considered to be the eikonal regime where the front is thin and sharp, where as $\Gamma_r \to 0$ is the mixing regime [35]. The fronts that we study do not lie in these extremities and are situated in the middle of the two bounds. Our reaction rate is always fixed at $\xi = 9$ which makes our Damköhler number $\text{Da} \sim \mathcal{O}(1)$. We use a Lewis number of $\text{Le} = 1, 0.1, 0.01$ and study a range of Péclet numbers of $0 \leq \text{Pe} \lesssim 1100$. Our thickness ratio of the flow length scale and front thickness is $\Gamma_r = 1/\delta_0$. The font thickness is a function of the Lewis number as evident from Eq. 3.9. For the Lewis numbers we study the thickness ratio is in the range $0.375 \leq \Gamma_r \leq 3.75$, which is away from the two bounds that describe mixing regime and eikonal regime [35].

Chapter 4

Computation of fluid dynamics and propagating fronts

In this chapter we describe our computational approach for computing the fluid and front dynamics. Our overall approach consists of creating a spectral element mesh, determining the polynomial order of interpolation and time step for computation, solving the governing equations which govern the fluid dynamics and front propagation given by Eq. 2.10 and Eq. 2.14-2.16, and post processing of the results.

For our computations we use a highly parallelized and high-order spectral element method (SEM) to solve the governing equations of the front and fluid dynamics described in Ch. 2. SEMs use high-order orthogonal polynomials as basis functions for discretization of nonlinear partial differential equations. Because of this, they can achieve ten digits of accuracy compared to two or three digits of accuracy with traditional finite-difference and finite-element approaches [77]. This high-order accuracy of SEM is referred to as 'spectral accuracy'. SEMs provide exponential convergence of errors with spatial resolution [77–79]. This makes SEMs very useful in solving highly nonlinear and pattern-forming systems. We use the open source SEM solver known as NEK5000 [40]. NEK5000 have been extensively used to study canonical pattern-forming systems such as Rayleigh-Bénard convection in high aspect ratio experimentally realistic domains [44, 80] . Additionally, NEK5000 has also been used to study the problem of front propagation and passive transport in three-dimensional Rayleigh-Bénard convection flow fields [38, 39, 56, 57].

Our computational domain is divided into a number of spectral elements. The solution is then represented in each element as a high order Langrangian interpolant polynomial based on a Gauss-Lobatto-Legendre (GLL) quadrature [79]. For the cylindrical domain of aspect ratio $\Gamma = 40$, which is shown in Fig. 1.1 (a), we use 3072 hexahedral spectral elements. For the rectangular mesh of aspect ratio $\Gamma_x = 30$ and $\Gamma_y = 5$, shown in Fig. 1.1 (b), we use 150 equally spaced square spectral elements. The choice for the number of elements is such that each element has a side length of unity. A length of one is equal to the depth of the convection layer and is also approximately equal to the width of a single convection roll. The number of elements are chosen such that each element approximately resolves about one convection roll. We first solve the flow field equations (Eqs. 2.6-2.8) using a 10th order polynomial for discretization. We then restart the flow field with the coupled RAD equation (Eq. 2.10) with 16th order polynomials. The increased spatial resolution is needed to quantify the intricacies of the complex and sharp front interface.

Figure 4.1 shows the x-y projection of the three-dimensional cylindrical mesh for better visualization. Figure 4.2 shows the three-dimensional rectangular mesh using an x-y projection. Each element in both Figs. 4.1-4.2 is discretized with 10th order polynomials. For understanding front induced feedback to the flow with smaller values of Lewis number ($\mathrm{Le} = 0.01$) we use a two-dimensional rectangular convection domain shown in Fig. 4.3. We have used 20th order polynomials to discretize the elements in Fig. 4.3. We use 480 equally spaced square elements in this domain, such that each element is 0.4×0.4 in dimension. We then solve the fluid flow with 16th order and the front with 20th order Lagrangian interpolant polynomials. The increased spatial resolution is needed to resolve fronts with $\mathrm{Le} = 0.01$ where the fluid flow has a large effect on the front dynamics and the front interface is sharper. This is discussed in Ch. 6 and Ch. 7. The increase in the number of elements is

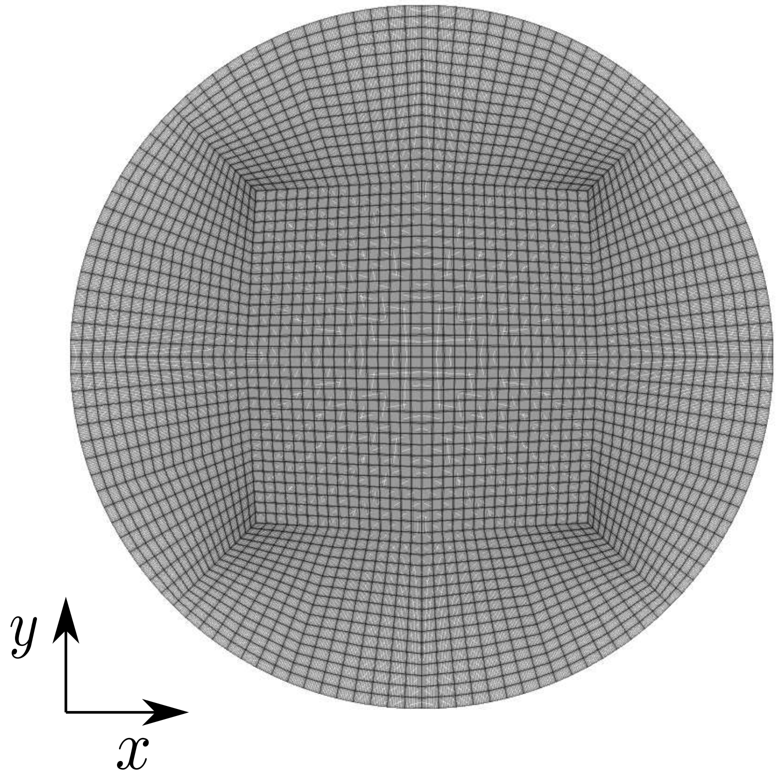

Figure 4.1: The x-y projection of the three-dimensional cylindrical mesh used for computations in the cylindrical domain of aspect ratio $\Gamma = 40$. The top view of the domain is shown. The mesh consists of 3072 hexahedral spectral elements. We have used 10th order polynomials to discretize the elements in the mesh for the figure shown here.

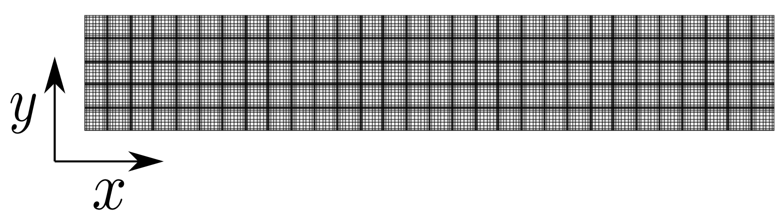

Figure 4.2: The x-y projection of the three-dimensional rectangular mesh used for computations in the rectangular domain of aspect ratio $\Gamma_x = 30$ and $\Gamma_y = 5$. The top view of the domain is shown. The mesh consists of 150 equally spaced square spectral elements. We have used 10th order polynomials to discretize the elements in the mesh for the figure shown here.

motivated from the fact that for computing fronts with smaller Lewis number Le, we need our smallest spatial resolution to be $\Delta x \sim \mathrm{Pe}^{-1/2}$ [56] where $\mathrm{Pe} = U/\mathrm{Le}$ is the Péclet number defined in Sec. 1.2.

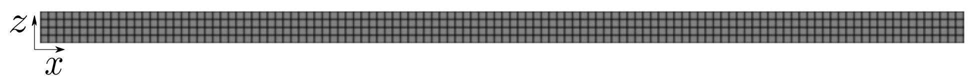

Figure 4.3: The two-dimensional rectangular mesh used for computations of fronts with Le $=0.1$ in a two-dimensional rectangular domain of aspect ratio $\Gamma_x = 30$. The mesh consists of 480 equally spaced square spectral elements. We have used 20th order polynomials to discretize the elements in the mesh for the figure shown here.

For the temporal discretization, NEK5000 employs an operator splitting approach where the nonlinear and forcing terms are treated explicitly and the linear terms are treated implicitly. A second or third order Adams-Bashforth method is used for the explicit time-stepping while a second or third order accurate backward difference scheme is used to treat the linear terms implicitly. We have employed third order temporal schemes for all our calculations which makes our solutions third order accurate in time. The temporal and spatial convergence of Rayleigh-Bénard convection using NEK5000 has been discussed in detail by Scheel [80]. Here we focus on the temporal convergence of the front solution. We use the asymptotic front velocity $\bar{v}_f$ for this analysis. For a front propagating in the absence of a flow field, the no-flow front velocity is given by an exact solution given by Eq. 3.2. We have verified the no-flow velocity of the fronts we explore converge to this solution. Figure 3.2 shows the excellent agreement between the result obtained and the no-flow solution using $\Delta t = 10^{-4}$ and 16th order polynomials for spatial interpolation in a rectangular domain.

Here we use the asymptotic front velocity $\bar{v}_f$ for a front propagating through a chain of straight parallel rolls at Ra $=3000$ and Le $=0.1$ in the absence of front induced feedback, that is $\text{Ra}_s = 0$ and $\eta = 0$. Figure 4.4 shows the spatial and temporal resolution of the asymptotic front velocity $\bar{v}_f$. Since we do not have an exact solution, we use the results obtained for the highest resolutions as a reference to quantify the solution convergence.

Figure 4.4 (a) shows the variation of the reduced asymptotic front velocity with the time-step Δt. The smallest time-step used was $\Delta t_{\min} = 2 \times 10^{-5}$. The reduced asymptotic front velocity is defined as $\Delta \bar{v}_f = |(\bar{v}_f - \bar{v}_{f,\min})/\bar{v}_{f,\min}|$, where $\bar{v}_{f,\min}$ has been computed with the smallest time-step $\Delta t_{\min}$. Shown is the logarithmic variation of $\Delta \bar{v}_f$ as a function of Δt. The solid line through the plot has a slope of 1.1. For a third order explicit time-stepping scheme we expect a slope of 3. There can be several contributions to this observed discrepancy. The solution used for the temporal convergence analysis is obtained from the coupled reaction-advection-diffusion equation to the flow. Moreover, the solution is obtained from the bulk burning rate integral given by Eq. 3.6 and the associated curve fitting of the front velocity given by Eq. 3.8 as discussed in Ch. 3 which may lead to some deviation from the expected slope of 3. However, overall this result points out the code's ability to quantify a complex quantity like the racting-advecting-diffusing front velocity, which is relevant to our calculation. Overall our result suggests $\Delta \bar{v}_f \propto \Delta t^{1.1}$.

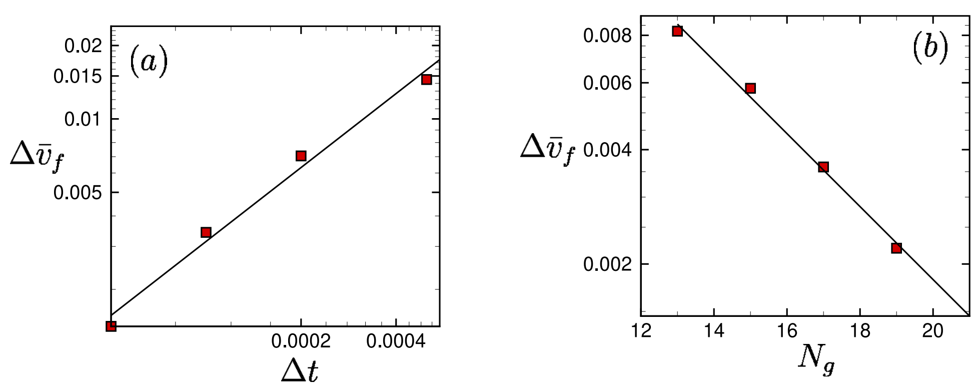

Figure 4.4: The temporal and spatial resolution of the reduced asymptotic front velocity with time-step size Δt and number of GLL polynomial points N_g. This is for front propagation in a field of straight parallel rolls in a rectangular domain at Ra = 3000 and Le = 0.1. The corresponding figure of the front is shown in Fig. 5.9. (a) The variation of the reduced asymptotic front velocity with the time-step size Δt using a log-log scale. The solid line has a slope of 1.1 which suggests $\Delta v_f \propto \Delta t^{1.1}$. (b) The variation of the reduced asymptotic front velocity with the number of GLL polynomial points N_g. The variation is shown using a log-linear plot. The solid line has a slope of -0.22 which suggests $\Delta \bar{v}_f \propto e^{-0.22 N_g}$.

Figure 4.4 (b) shows the variation of the reduced asymptotic front velocity $\Delta\bar{v}_f$ as a function of the number of GLL interpolation points N_g. For a particular value of N_g, the order of the polynomial used for interpolation is $N_g - 1$. The highest spatial resolution used was $N_{g,\max} = 21$. The reduced asymptotic front velocity is defined for this case as $\Delta\bar{v}_f = |\left(\bar{v}_f - \bar{v}_{f,\max}\right)/\bar{v}_{f,\max}|$, where $\bar{v}_{f,\max}$ has been computed with the highest spatial resolution of $N_{g,\max}$. A semi-logarithmic plot is shown where the $\Delta\bar{v}_f$ is plotted in log scale. The linear trend in the data shows exponential convergence of errors with spatial resolution which is expected for the spectral element approach. The black solid line has a slope of -0.22. Overall, our result suggests $\Delta\bar{v}_f \propto e^{-0.22N_g}$. Exponential convergence of solutions with the spatial resolution is a key property of spectral element methods. Our results show that the asymptotic front velocity is exponentially convergent with the polynomial order of interpolation.

Chapter 5

Front propagation without front induced feedback

We are interested in studying front propagation with one-way coupling between the fluid flow and the front and no front induced feedback to the flow. That is, the spatial variations in the flow field affect the front but the front does not affect the flow field. In this scenario we will have $\mathrm{Ra} \geq 0$, $\mathrm{Ra}_s = 0$ and $\eta = 0$ in Eqs. 2.14-2.16. Although the front will not have any feedback to the fluid flow, the underlying fluid motion will modify the velocity and geometry of the propagating fronts in a complicated way. The results discussed in this chapter have been published in Ref. [38]. We will study fronts in: (i) quiescent flow fields with $\mathrm{Ra} = 0$, (ii) a flow field consisting of time-independent cellular straight parallel convection rolls and, (iii) a flow field consisting of spatiotemporally chaotic convection rolls and weakly turbulent convection rolls. We explore a range of Rayleigh numbers from $0 \leq \mathrm{Ra} \leq 25000$ which will consist of different types of convection rolls such as straight parallel rolls, convection rolls undergoing spiral defect chaos and convection rolls undergoing an oscillatory instability. We will fix our nondimensional reaction rate at $\xi = 9$ and we will study Lewis numbers of $\mathrm{Le} = 1$ and $\mathrm{Le} = 0.1$. We will explore the Péclet number and Damköhler number ranges of $0 \leq \mathrm{Pe} \lesssim 1000$ and $0.1 \lesssim \mathrm{Da} \lesssim 30$.

5.1 Convective flow field

An integral component of our study is to quantify front propagation in a range of complicated flow fields such as straight parallel convection rolls, rolls exhibiting spiral defect chaos and oscillatory and weakly turbulent convection rolls. The rolls are obtained by varying the Rayleigh number from $0 \leq \mathrm{Ra} \leq 25000$ and using a Prandtl number, $\sigma = 1$. The governing equations Eqs. 2.6-2.8 are then solved. The temperature field acts as a passive scalar in the governing equations of Rayleigh-Bénard convection as shown in Eqs. 2.6-2.8. The temperature field is thus a direct indicator of the underlying flow structures and we will find it useful to visualize the underlying flow structure using the temperature field.

5.1.1 Straight parallel convection rolls

We use a rectangular domain shown in Fig. 1.1 (b) with aspect ratio $\Gamma_x = 30$ and $\Gamma_y = 5$. In order to achieve straight parallel rolls, we used a hot sidewall condition for the walls aligned with the x-direction such that $T(x = 0, y, z, t) = T(x = \Gamma_x, y, z, t) = 1$. The sidewalls force the fluid at the sidewall to rise and form rolls which propagates inward to fill the entire domain. We run the simulation until all the initial transients have decayed as indicated by the time variation of Nusselt number in Fig. 5.3. In general, it is considered that a time on the order of one horizontal diffusion time $\tau_h \sim \Gamma^2 \tau_\alpha$ is sufficient for all the initial transients to decay [2]. The time variation of Nusselt number is shown in a small window of time for $t = 3$ where the time has been adjusted such that $t = 0$ corresponds to $t = \tau_h$. Nusselt number is defined as the ratio of the total heat transfer to the conductive heat transfer. A value of $\mathrm{Nu} > 1$ indicates the presence of convective heat transfer [2].

We start with initial conditions which are random perturbations to the temperature field such that we get 15 pairs of counter rotating convection rolls (30 convection rolls) which are lined up in the x-direction. The wavelength of this pattern is thus approximately $\lambda \approx 2$ and the wavenumber of the pattern is $k \approx \pi$. We explore a range of $0 \leq \mathrm{Ra} \leq 6900$. For $\mathrm{Ra} \geq 6900$, the straight parallel rolls become unstable when simulated long enough due to a *skew-varicose* instability [2]. However, for the purpose of studying front propagation in a field of straight parallel rolls, we need the straight parallel rolls to persist at the same wavenumber for $t \lesssim 10$. This condition holds true for all our simulations in the rectangular domain to obtain straight parallel rolls. The boundary conditions for the fluid is no-slip in the x and z walls and periodic in the y direction. Figure 5.1 shows a field of straight parallel convection rolls at $\mathrm{Ra} = 3000$ in a rectangular domain of aspect ratio $\Gamma_x = 30$ and $\Gamma_y = 5$. Figure 5.1 (a) shows the view in the x-z plane at the slice of $y = \Gamma_y/2$. Figure 5.1 (b) shows the view in the x-y plane at the slice of $z = 1/2$. Overall it is clear from the figure that the straight parallel convection rolls have lined up in the x direction with a wavenumber of $k \approx \pi$.

The red solid line in the Fig. 5.3 indicates the time variation of Nusselt number for straight parallel rolls at $\mathrm{Ra} = 6000$. The line is flat which indicates that the convection rolls are steady. The hot sidewalls stabilize the straight parallel rolls to line up in the x-direction. Figure 5.2 shows the fluid flow velocity magnitude along with the direction of fluid velocity shown by the fluid velocity vectors. The spatial variation of the fluid velocity indicates maximum fluid flow at the boundaries of convection rolls and zero fluid motion near the core of the convection rolls as expected. We use the characteristic fluid velocity U which is defined as the time average of the maximum fluid velocity in the domain, at the horizontal midplane, to quantify the fluid. To avoid the influence of the hot sidewalls, we measure U in a spatial region which is 4 convection rolls away from the sidewalls. For Figs. 5.1-5.2 this yields a value of $U = 10.81$.

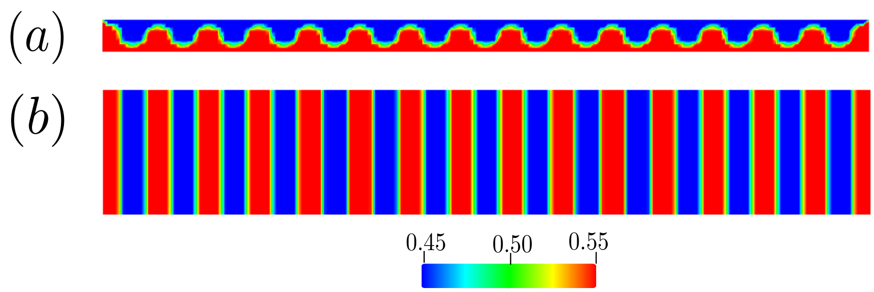

Figure 5.1: A field of straight parallel convection rolls in a rectangular domain shown in Fig. 1.1 (b) with $\Gamma_x = 30$ and $\Gamma_y = 5$. The Rayleigh number is Ra = 3000. Shown are the color contours of temperature field. The left and right walls aligned with the x-direction are hot such that $T(x=0,y,z,t) = T(x=\Gamma_x,y,z,t) = 1$. The sidewalls help the formation of straight parallel convection rolls by forcing the fluid at the sidewall to rise and form a roll. The color contours are of temperature field where red is hot rising fluid and blue is cold descending fluid. (a) Color contours of the temperature field in the x-z plane shown at the y-midplane of $y = \Gamma_y/2$. (b) Color contours of the temperature in the x-y plane at $z = 1/2$.

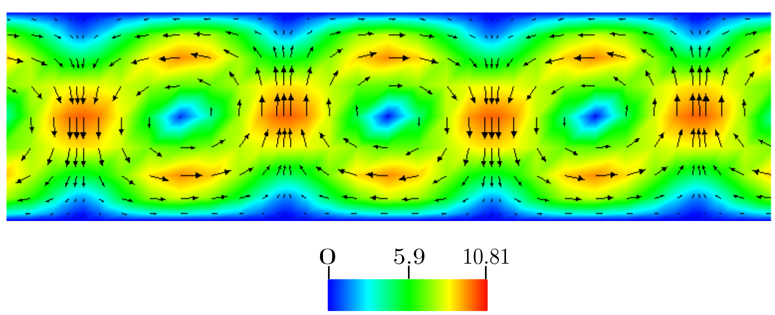

Figure 5.2: A zoomed-in view of the fluid velocity of the counterrotating convection rolls in Fig. 5.1. The arrows represent the fluid velocity vector. Shown is the color contour of fluid velocity magnitude $|\vec{u}| = \sqrt{u^2+v^2+w^2}$ where the maximum velocity is 10.81 for Ra = 3000. An x-z projection is shown at a slice $y = \Gamma_y/2$ similar to Fig. 5.1 (a).

Figure 5.4 shows the variation of U as a function of Ra. The data symbols shown as blue squares denote the characteristic fluid velocity for straight parallel rolls for a range of $0 \le \epsilon \lesssim 3.04$, where $\epsilon = (\mathrm{Ra} - \mathrm{Ra}_c)/\mathrm{Ra}_c$. The solid line is a curve fit through the data where $U = 12.54\epsilon^{0.54}$. It is interesting to note that the dependence $U \propto \sqrt{\epsilon}$ near the onset of convection is expected [2]. However, it is interesting that for our results, this dependence persists away from the convective threshold. The red circles represent the data for chaotic

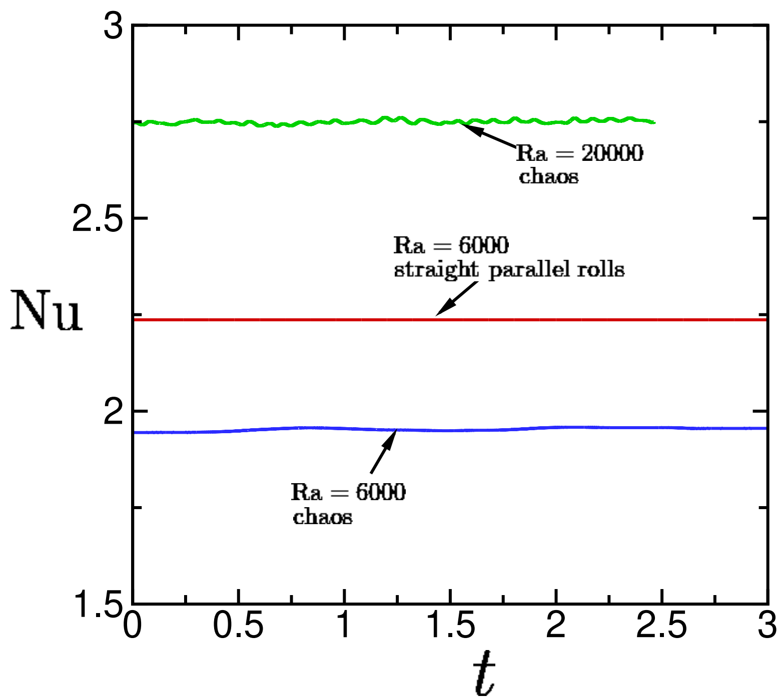

Figure 5.3: The variation of Nusselt number with time. The blue line is the variation of Nusselt number with time for convection rolls exhibiting spatiotemporal chaos at Ra = 6000 in the cylindrical domain shown in Fig. 1.1 (a). The red line represents the variation of the Nusselt number with time for straight parallel rolls in a rectangular domain shown in Fig. 1.1 (b). The green line represents the variation of Nusselt number with time for convection rolls exhibiting chaos and weak turbulence at Ra = 20000. The time is adjusted such that $t = 0$ is one horizontal diffusion time or $t_0 = \tau_h$ after the numerical simulation was started. The variation is shown for three vertical diffusion times ($t = 3$).

flow fields which will be explained in section Sec. 5.1.2.

5.1.2 Spatiotemporally chaotic convection rolls

We use a cylindrical domain as shown in Fig. 1.1 (a) to study fronts in spatiotemporally chaotic flow fields. The aspect ratio of the cylindrical domain is $\Gamma = r_0/d = 40$. Large aspect ratio cylindrical domains are widely used in experiments to study spatiotemporal chaos in Rayleigh-Bénard convection [2, 43]. Figure 5.5 shows several visualizations of a typical

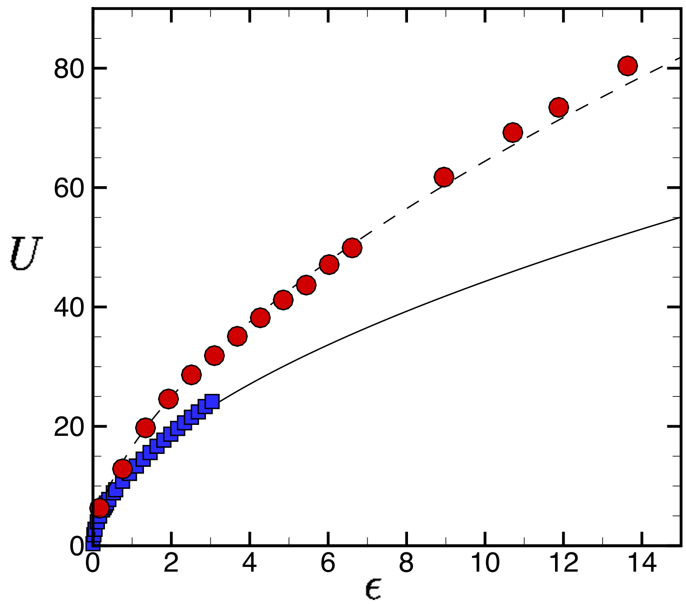

Figure 5.4: The variation of the characteristic velocity U with the reduced Rayleigh number ϵ. The circles (red) points are data points for chaotic and weakly turbulent flow fields in the cylindrical domain shown in Fig. 1.1 (a). The dashed line is a power law fit through the data points where $U = 16.61\epsilon^{0.59}$. The squares (blue) are data points for the straight-parallel rolls in a rectangular domain shown in Fig. 1.1 (b) and in Fig. 5.1. The solid line is a power law fit through the data where $U = 12.54\epsilon^{0.54}$.

chaotic flow field at $\mathrm{Ra} = 9000$ in the horizontal midplane of $z = 1/2$. Figure 5.5 (a) shows the color contours of temperature field for the flow field where red is the hot rising fluid and blue is the cold descending fluid. Figure 5.5 (b) shows the color contours of the vertical component of the fluid velocity w where the red and blue represent rising and falling fluid. At the horizontal midplane slice, w is the largest component of fluid velocity. It is clear from Fig. 5.5 (a) and Fig. 5.5 (b) that the temperature field closely follows the vertical component of the fluid velocity. Figure 5.5 (c) shows the color contour of the magnitude of fluid velocity in the x-y plane $|u_\perp|$ where $\vec{u}_\perp = (u, v)$. We use the convention $\vec{u}_\perp$ to represent the fluid velocity components which are perpendicular to the temperature gradient in the z direction following [2]. Figure 5.5 (c) shows that the color contours of $|u_\perp|$ is not representative of the flow field pattern. Red and blue denote large and small velocity magnitude respectively.

Overall, the magnitude of $\vec{u}_\perp$ is small as expected, however there are spatial regions where we find $\vec{u}_\perp$ is of large magnitude. These spatial regions correspond to local defects and disorder in the flow field which affects the front velocity. $|\vec{u}_\perp|$ is nearly zero in the spatial regions consisting of straight parallel convection rolls. The vertical average of $\vec{u}_\perp$ equals the *mean flow* which has been shown to be intricately linked with spiral defect chaos [81]. Figure 5.5 (d) shows the color contours of total fluid velocity magnitude $|\vec{u}|$, at the horizontal midplane slice. Figure 5.5 (d) shows the large velocity magnitudes occur in spatially disordered regions as well as regions consisting of regular straight parallel rolls. We define the maximum value of velocity magnitude in Fig. 5.5 (d) as the characteristic fluid velocity U. The variation of U with Ra for Rayleigh-Bénard convection in the cylindrical domain is shown by the red circles in Fig. 5.4. The solid line through the data shows a power law fit of $U = 16.61\epsilon^{0.59}$. Overall, it is clear that the temperature field is a good representation of the flow field.

We plot spatiotemporally chaotic convective flow fields for different Rayleigh numbers in Fig. 5.6. The color contours of the temperature field is shown in the horizontal midplane. As the Rayleigh number increases, the flow field becomes increasingly complex with defects and small scale complex features as can be seen in Fig. 5.6 (a), (b) and (c) which are at $\mathrm{Ra} = 3000, 6000, 9000$ respectively. Each flow field has been simulated for a time of $t \sim \tau_h$. Figure 5.3 shows the time variation of Nusselt number for a chaotic flow field at $\mathrm{Ra} = 6000$ shown in Fig. 5.6 (b). The heat transfer due to convection is less efficient than for the case of straight parallel convection rolls shown by the red line. The convection rolls are now time-dependent and spatially irregular. The complex spatiotemporal dynamics involves the nucleation and annihilation of defect structures. For this condition, it has been shown that the flow fields exhibit *extensive* chaos [45, 82] and yields a spectrum positive Lyapunov exponents which is an important signature of high-dimensional chaos. For $\mathrm{Ra} \leq 10^4$, this state also corresponds to the spiral defect chaos state as seen in the experiments. Under this

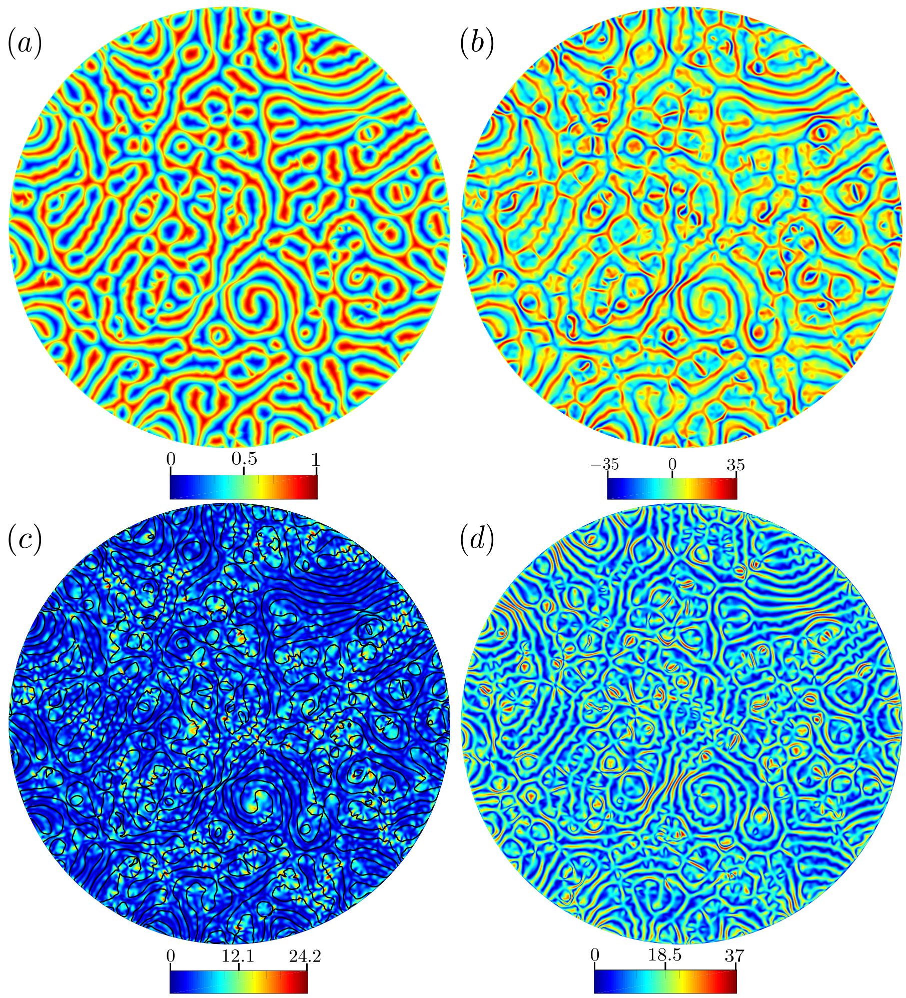

Figure 5.5: Different representations of flow fields of spatiotemporally chaotic convection at Ra $= 9000$ and $\sigma = 1$ in a cylinder of aspect ratio $\Gamma = 40$ shown in Fig. 1.1 (a) at the midplane $z = 1/2$. The flow field is shown at a specific time t. (a) Contours of the temperature field $T(x, y, z, t)$ where red is hot rising fluid and blue is cold descending fluid. (b) Contours of the vertical component of the fluid velocity $w(x, y, z, t)$ where red represents rising fluid and blue represents descending fluid. (c) The contours of the fluid velocity in the x-y plane $u_\perp$ where red represents large magnitude and blue represents small magnitude. (d) The magnitude of fluid velocity $|\vec{u}|$ where red represents large fluid velocity magnitude and blue represents small fluid velocity magnitude.

state, convection rolls exhibit a chaotic pattern consisting of spirals and defects [42].

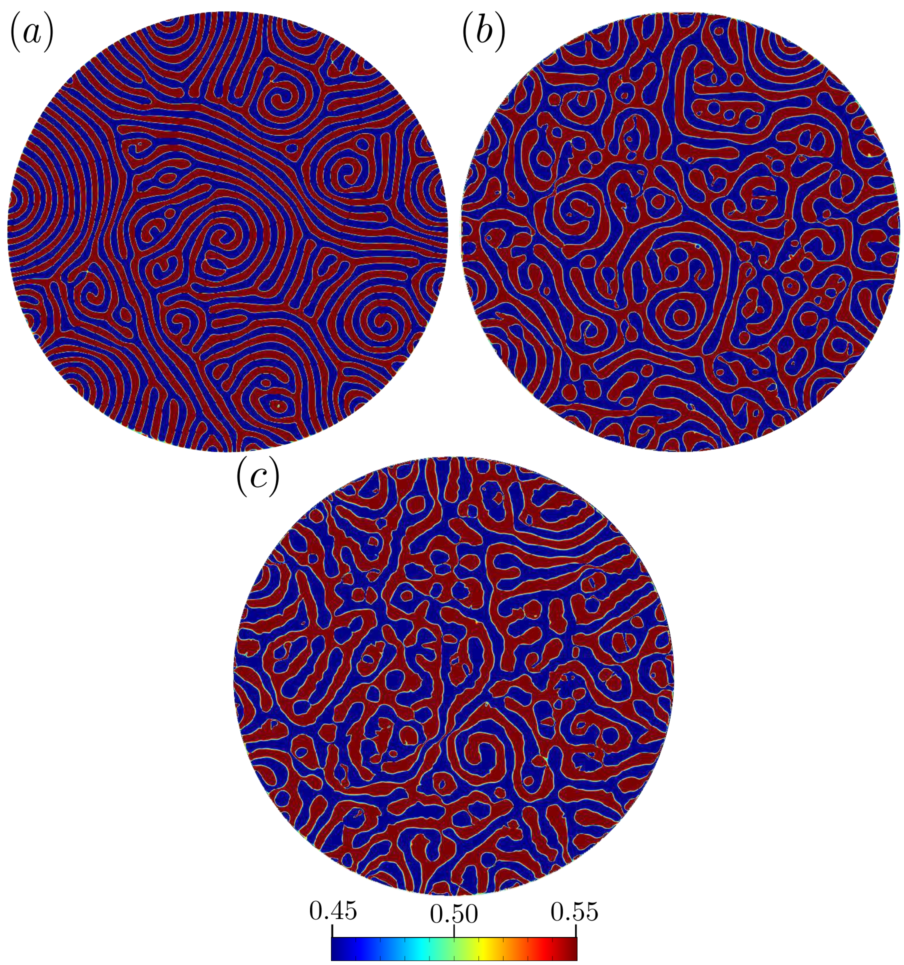

Figure 5.6: Spatiotemporally chaotic convection flow fields in a cylindrical domain of aspect ratio $\Gamma = 40$ shown in Fig. 1.1 (a). Prandtl number of the fluid is $\sigma = 1$. For these parameters, the flow fields undergo *spiral defect* chaos [42]. The color contours are of temperature $T(x, y, z = 1/2, t)$ at a specific time t where red represents hot rising fluids and blue represents cold descending fluid. Shown are flow fields for (a) $\mathrm{Ra} = 3000$, (b) $\mathrm{Ra} = 6000$ and (c) $\mathrm{Ra} = 9000$.

5.1.3 Weakly turbulent convection rolls

For $\mathrm{Ra} \geq 10^4$ the flow field undergoes an *oscillatory* instability which consists of small scale features traveling axially along the convection rolls [43]. We call flow fields exhibiting oscillatory instability as *weakly turbulent* because the small scale oscillatory features give rise to plume structures and turbulence. We signify this initial deterioration of the convection rolls as *weak turbulence*. Figure 5.7 shows several flow fields at $\mathrm{Ra} = 13000, 20000, 25000$. The axially traveling small scale features along the convection rolls are clear when compared to Fig. 5.6. For the highest Rayleigh number that we studied $\mathrm{Ra} = 25000$ shown in Fig. 5.7 (c), the flow field is highly disordered and complicated. The small scale features in the axial direction of the convection rolls are significant and there are localized regions where the convection rolls give rise to plumes. Figure 5.3 shows the time variation of Nusselt number for a weakly turbulent flow field at $\mathrm{Ra} = 20000$ as shown in Fig. 5.7 (b) by the solid green line. The convective heat transfer is now much larger because of the larger Rayleigh number. Moreover, the increased time dependence and oscillations of the flow field is visible by the small fluctuations about the mean value in the Nusselt number.

5.2 Front propagation in convective flow fields

In this section we will study front propagation through the flow fields discussed in Sec. 5.1. Figure 5.8-5.9 shows a front propagating through the flow field consisting of straight parallel convection rolls as shown in Fig. 5.1. The fronts are pulled and are initiated in the left wall with an initial condition given by Eq. 3.3. Figure 5.8 shows a front with Lewis number $\mathrm{Le} = 1$, which means that the the thermal and the molecular diffusivity are equal and the flow field does not have a significant effect on the front. This is apparent from the smooth transition from the products (red) to reactants (blue) in Fig. 5.8.

Figure 5.9 shows a propagating front through straight parallel rolls at $\mathrm{Le} = 0.1$. In this case, the flow field has a larger effect on the front dynamics which is apparent from the discontinuous transition from products to reactants. Because of the lowered diffusion, the front gets whirled around by a convection roll before moving on to the next convection roll by diffusion and reactive instability. The reaction zone thickness is smaller than the case of

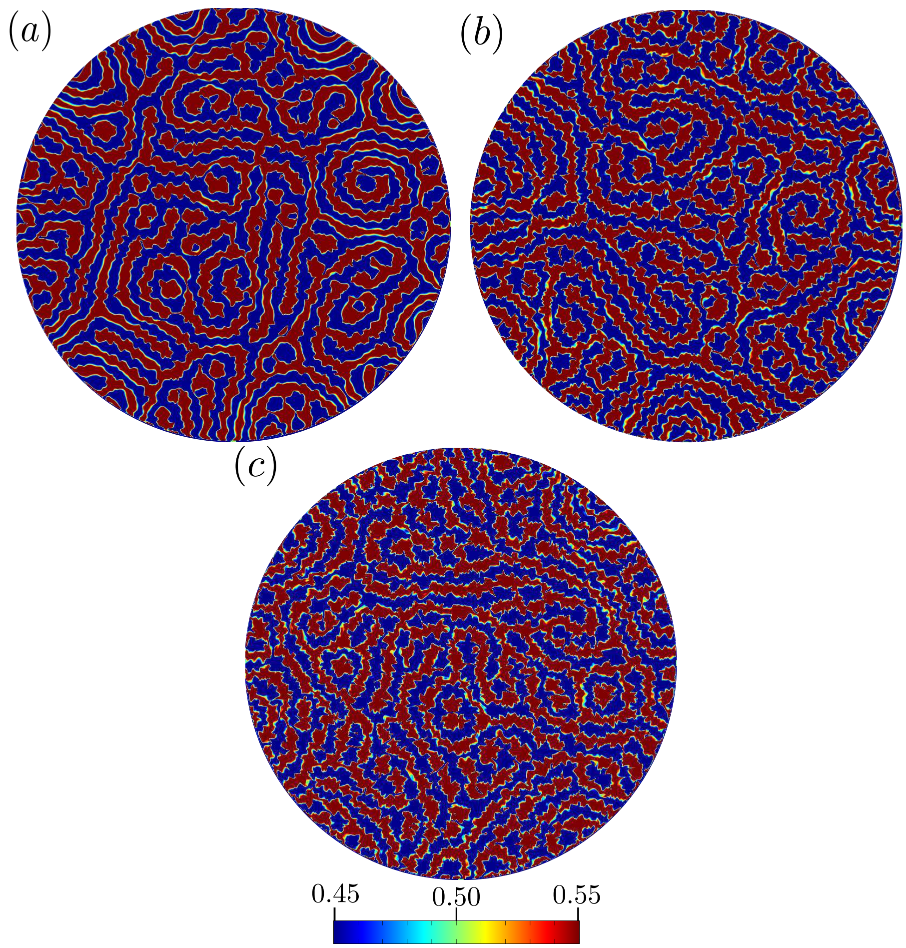

Figure 5.7: Oscillatory and weakly turbulent convection flow fields in a cylindrical domain of aspect ratio $\Gamma = 40$ shown in Fig. 1.1 (a). Prandtl number of the fluid is $\sigma = 1$. For these parameters, the convection rolls undergo an oscillatory instability for Ra $>$ 10000 and transition to a weakly turbulent flow field which consists of time independent irregular convection rolls and plumes. The color contours are of temperature $T(x, y, z = 1/2, t)$ at a specific time t where red represents hot rising fluids and blue represents cold descending fluid. Shown are flow fields for (a) Ra = 13000, (b) Ra = 20000 and (c) Ra = 25000.

Le = 1 as predicted.

The effect of the flow field on the front is apparent in Fig. 5.10, where a zoomed-in view of the front is shown in the vertical x-z plane. The smooth transition from products to reactants for Le = 1 is clear in Fig. 5.10 (a). Figure 5.10 (b) shows that for Le = 0.1 the reaction spirals into the core of a convection roll. The front gets whirled around to the center

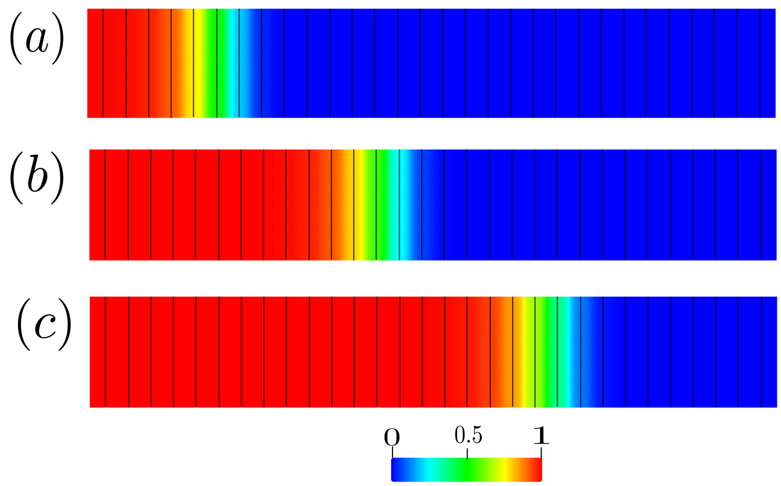

Figure 5.8: A front propagating in a field of straight parallel rolls shown in Fig. 5.1 (b) at Ra $= 3000$ and Le $= 1$. The color contours are of concentration at the horizontal midplane $c(x, y, z = 1/2, t)$ where red is pure products ($c = 1$), blue is pure reactants ($c = 0$) and the intermediate green and yellow spatial region is the reaction zone or front. The black lines are contours of $T = 1/2$ which indicates the center-line of the convection rolls. The front is shown in different times at (a) $t = 1$ (b) $t = 2$ and (c) $t = 3$ where t is measured from the initiation of the reaction at the left wall. (Additional parameters : $U =$ Pe $= 10.81$ and Da $= 0.83$.)

of the convection rolls to complete a reaction before moving on to the next roll.

Figure 5.11 shows the closeup view of the geometry of $c = 1/2$ level-set or the front at the x-z plane. The front geometry is morphed by the convection rolls. Figure 5.11 (a)-(d) shows the propagating front at Le $= 1$. The convection rolls bend the initially straight front to an S-shaped structure. Figure 5.11 (e)-(h) shows the propagating front at Le $= 0.1$. The increased distortion of the front for this case is apparent. The convection rolls induce the reaction to spiral inside its core, which results in the cusp-like structures of the front geometry as evident in Fig. 5.11 (e)-(h).

Snapshots of propagating fronts in chaotic flow fields are shown in Fig. 5.12-5.13. The fronts are initiated by a reaction in the center of the domain with a pulled front initial condition given Eq. 3.4. The fronts are propagating radially outwards with the color red representing

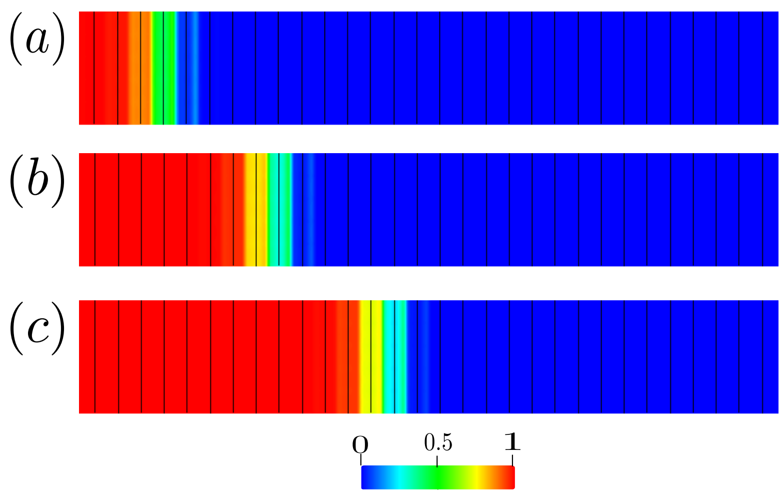

Figure 5.9: A front propagating in a field of straight parallel rolls shown in Fig. 5.1 (b) at Ra = 3000 and Le = 0.1. The color contours are of concentration at the horizontal midplane $c(x, y, z = 1/2, t)$ where red is products ($c = 1$), blue is reactants ($c = 0$) and the intermediate green and yellow spatial region is the reaction zone or front. The black lines are contours of $T = 1/2$ which indicates the center-line of the convection rolls. The front is shown in different times at (a) $t = 1$ (b) $t = 2$ and (c) $t = 3$ where t is measured from the initiation of the reaction at the left wall. (Additional parameters: $U = 10.81$, $\mathrm{Pe} = 100.81$, $\mathrm{Da} = 0.83$.)

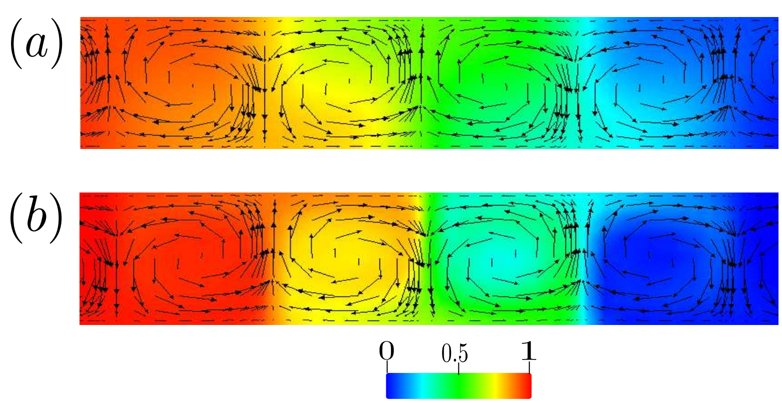

Figure 5.10: A zoomed-in view of the x-z projection of the propagating fronts in Figs. 5.8 and 5.9. Color contours of $c(x, y = \Gamma_y/2, z, t)$. The black arrows are the fluid velocity vectors which indicate the counterrotating convection rolls. (a) Le$=$1, (b) Le$=$0.1.

products and blue representing the reactants of the reaction-advection-diffusion equation given by Eq. 2.10. The snapshots are shown in the horizontal midplane $z = 1/2$ with

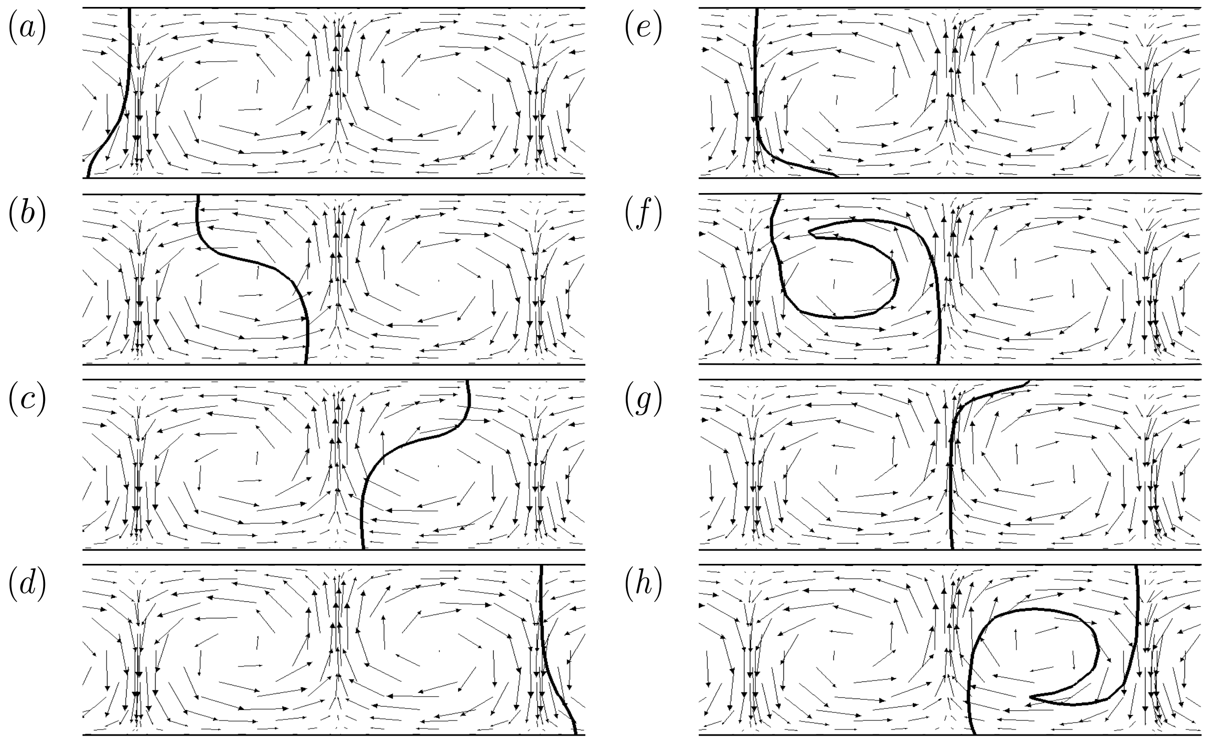

Figure 5.11: A zoomed-in view of the spatial structure of the propagating fronts traveling from left to right in a field of cellular convection rolls at Ra = 3000. The horizontal extent of each panel includes a pair of counterrotating convection rolls. The propagating front is described as the solid black line which represents $c = 1/2$ level-set. The flow field vectors are visualized by arrows. (a)-(d) Le=1 and (e)-(h) Le=0.1. The time between successive panels is 0.1 time units.

Ra $= 9000, 13000, 25000$ in Fig. 5.12 (a), (b) and (c) respectively. The distortion of the front is apparent by the small scale spatial features in the reaction zone due to the chaotic flow. The distortion increases with the complexity of the flow given by the Rayleigh number. For flow fields which have undergone oscillatory instability as shown in Fig. 5.12 (a) and (b), the complexity in the front geometry increases.

Figure 5.13 shows fronts propagating in chaotic flow fields at Le $= 0.1$. For this case, there is an increased dependence of the front on the underlying fluid dynamics, which is evident from the complex exaggerated small scale features of the reaction zone. Figure 5.13 (a)

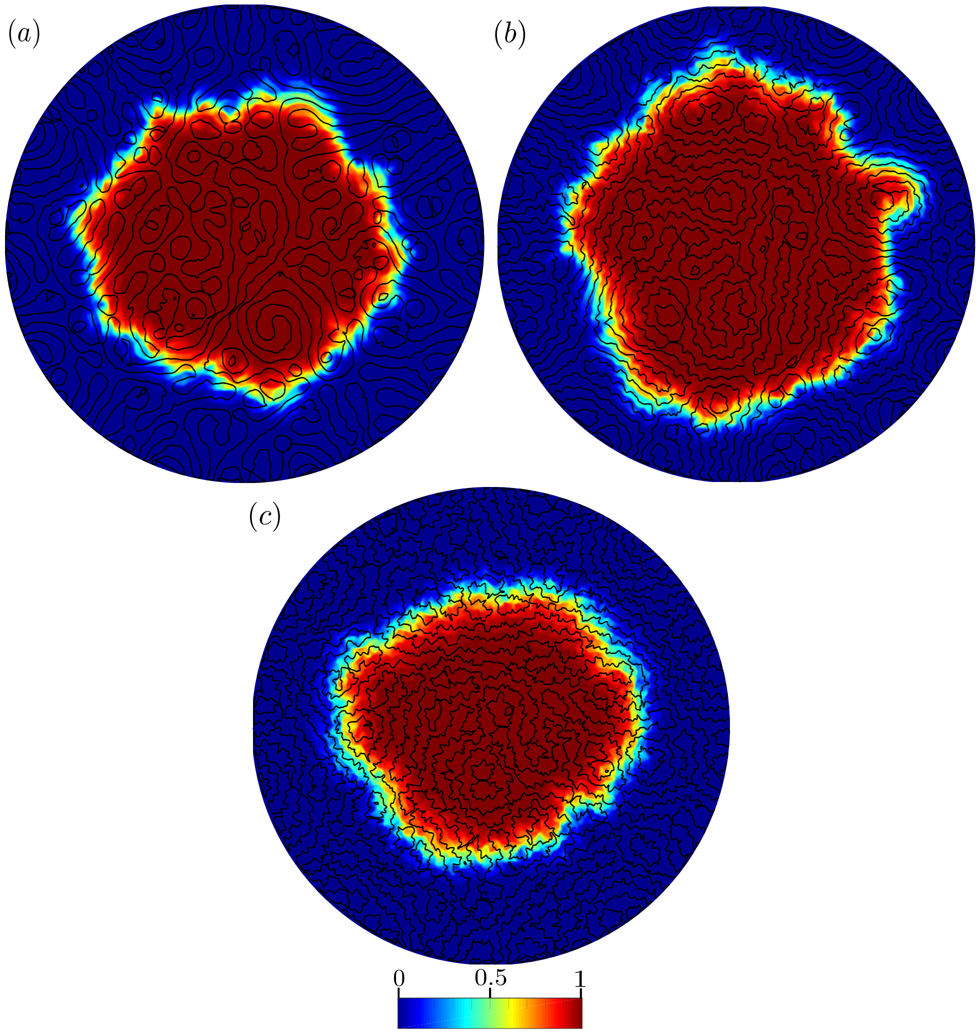

Figure 5.12: Fronts propagating in spatiotemporally chaotic and weakly turbulent flow fields for Le = 1 where (a) Ra = 9000, (b) Ra = 13000, and (c) Ra = 25000. The color contours are of concentration at the horizontal midplane $c(x, y, z = 1/2, t)$ where red is pure products and blue is pure reactants. The snapshots of fronts are shown at different times from the initiation of the reaction at the center of the domain where (a) $t = 3$, (b) $t = 3$, and (c) $t = 2.5$.

and (b) show the snapshots in time of fronts propagating through chaotic flow fields at Ra = 9000 and Ra = 13000. The front geometry becomes come complex for Fig. 5.13 (b) where the flow field has undergone an oscillatory instability. For Le = 0.1, Ra = 13000 was the maximum value of Rayleigh number we could explore. For larger values of Ra, more number of spectral elements or a sophisticated numerical approach using specialized filters will have to be used [56]. We have not explored these numerical ideas further however, this is an interesting direction for future exploration.

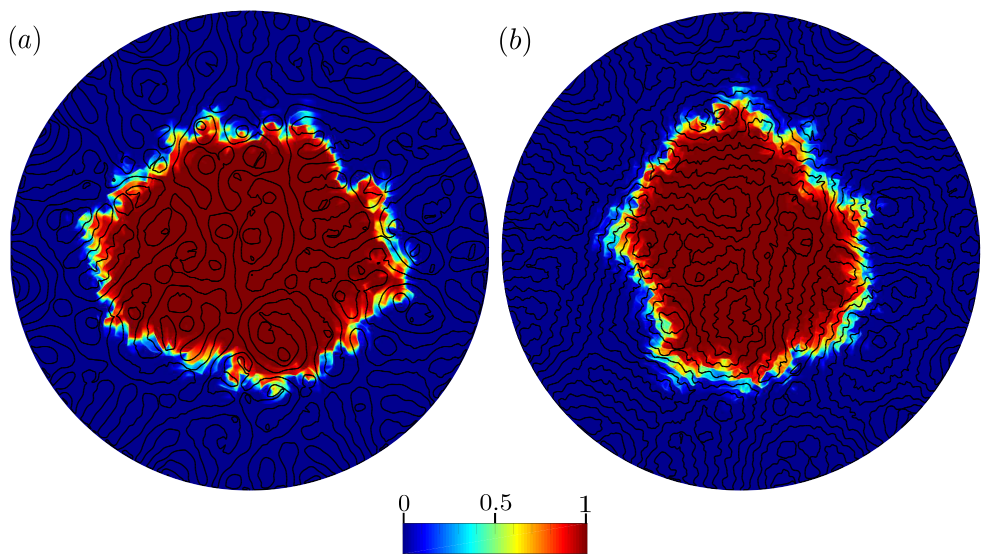

Figure 5.13: Fronts propagating in spatiotemporally chaotic and weakly turbulent flow fields for Le = 0.1 where (a) Ra = 9000 and (b) Ra = 13000. The color contours are of concentration at the horizontal midplane $c(x, y, z = 1/2, t)$ where red is pure products and blue is pure reactants. The snapshots of fronts are shown at different times from the initiation of the reaction at the center of the domain where (a) $t = 4$ and (b) $t = 3$.

5.2.1 Velocity of fronts

In this section we study and quantify the front velocity of propagating fronts shown through straight parallel rolls and chaotic flow fields as shown in Fig. 5.8-5.13. Quantifying the front velocity through disordered flow fields is challenging. We use an integral approach known as *bulk burning rate* defined in the Sec. 3.2 to quantify the front velocity.

Figure 5.14 shows a comparison between the front velocity obtained from bulk burning rate and simply tracking the $c = 1/2$ level-set as shown in Fig. 5.11. Figure 5.14 shows the time variation of the bulk burning rate velocity, shown in the color red, and the velocity obtained by tracking the front shown with blue color for a front propagating through straight parallel rolls at Ra = 3000. The dashed and dashed-dotted lines indicate the no-flow front velocity v_0 for Le = 1 and Le = 0.1 respectively. In practice, for computational ease, we do not use the full bulk burning rate integral as in Eq. 3.6, but rather compute the velocity in the midplane at $z = 1/2$. The modified bulk burning rate equation that we use is,

$$v_f(t) = \int_0^{\Gamma_x} \frac{\partial c}{\partial t}\Big|_{z=1/2} dx. \tag{5.1}$$

The use of the modified bulk burning rate equation results in an error that is less than 0.2% when compared to the full integral. As can be seen from Fig. 5.14 the tracked front velocity and the front velocity obtained from using bulk burning rate are in excellent agreement. Figure 5.14 also shows the enhancement of the front velocity due to the underlying flow velocity. The enhancement of front velocity from the no-flow velocity due to the convection rolls is $\bar{v}_f/v_0 = 1.26$ for Le = 1. The enhancement is more prominent for Le = 0.1, where $\bar{v}_f/v_0 = 2.61$ because of the increased effect of the fluid velocity on the front.

Figure 5.15 shows the time variation of bulk burning rate velocity for three different Rayleigh numbers at Le = 0.1. The asymptotic front velocity $\bar{v}_f$ is obtained by curve-fitting the data with an algebraic fit which follows Eq. 3.8. The algebraic fit is shown by the solid lines through the data points in Fig. 5.15.

We calculate the asymptotic front velocity $\bar{v}_f$ and the characteristic fluid velocity U for the convective flow fields at different Rayleigh number. Figure 5.16 shows the variation of $\bar{v}_f$ with U for fronts propagating in the straight parallel rolls. The data is categorized into two groups based on the Damköhler number, Da = ξ/U. The blue circles are results for fast reaction and slow advection regime where Da > 1 and the red squares are results for slow

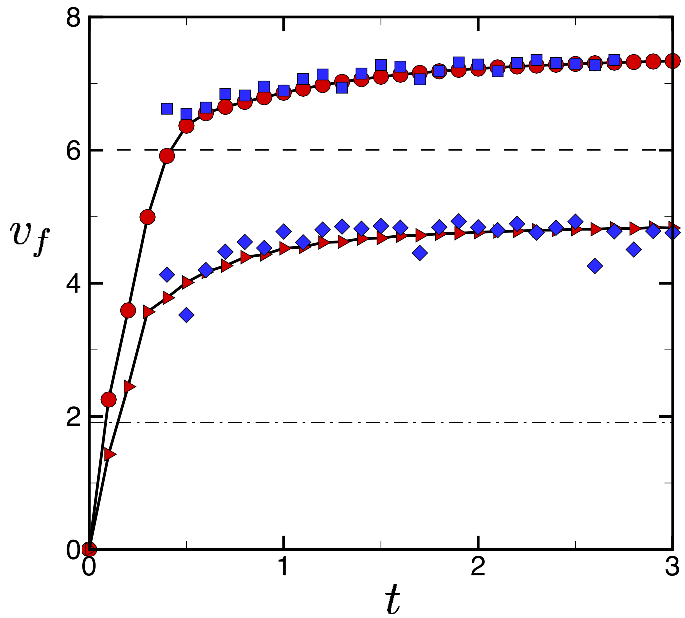

Figure 5.14: The time variation of front velocity $v_f(t)$ for fronts propagating in straight parallel convection rolls shown in Fig. 5.8 and Fig. 5.9. The straight parallel convection rolls are at Ra = 3000 as shown in Fig. 5.1 (b). The blue symbols are front velocities computed by tracking the level-set contour for $c = 1/2$ as shown in Fig. 5.10 with squares denoting front with Le = 0.1 and diamonds denoting front with Le = 1. The red symbols and solid lines are front velocity computed using bulk burning rate approach as defined in Eq. 3.6. The circles denote front at Le = 1 and triangles denote front at Le = 0.1. The dashed and dash-dotted lines indicate no-flow front velocity where $v_0 = 6$ for Le = 1 and $v_0 = 1.9$ for Le = 0.1 respectively. For these results we have $\bar{v}_f = 7.57$ for Le = 1 and $\bar{v}_f = 4.96$ for Le = 0.1.

reaction and fast advection regime where Da < 1.

Figure 5.16 (a) shows the data for Le = 1. The solid line through the blue circles in Fig. 5.16 (a) is a quadratic curve fit of the form $\bar{v}_f/v_0 = 1 + 0.09(U/v_0)^2$. This relation is in agreement with the Clavin-Williams relation of premixed flame propagation [83]. The quadratic variation of $\bar{v}_f$ with U can be recovered by expanding the concentration c with a small parameter U and solving Eq. 2.10 with a coupled cellular flow and freeslip boundary conditions. The solid line through the red data points in the fast advection regime in Fig. 5.16 (a) is a curve-fit of the form $\bar{v}_f/v_0 = 1.06(U/v_0)^{0.31}$. For these results the Péclet

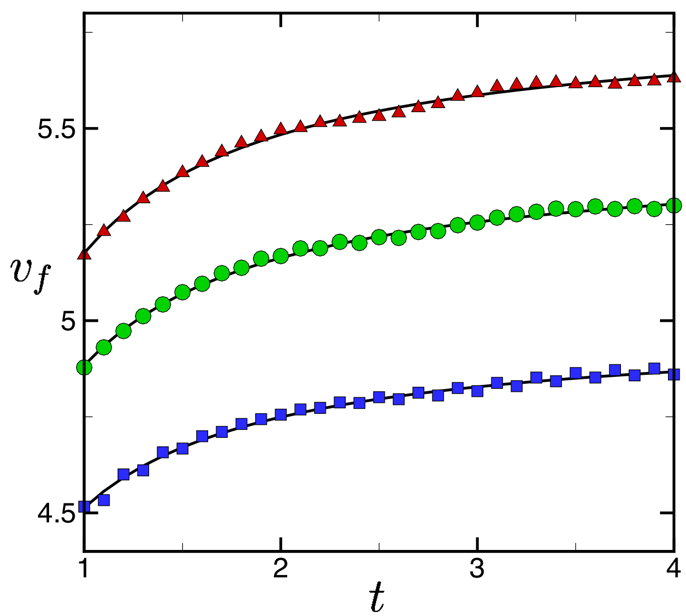

Figure 5.15: Variation of front velocity v_f with time and the determination of asymptotic front velocity $\bar{v}_f$ for propagating fronts in a field of straight parallel convection rolls where $\mathrm{Le} = 0.1$. The blue squares, green circles and red triangles are for $\mathrm{Ra} = 3000, 3600, 4200$ respectively. The solid lines are curve fits through the data using the algebraic relation given by Eq. 3.8. For these results the asymptotic front velocity yields $\bar{v}_f = 4.98, 5.44$ and 5.79 respectively.

number is $\mathrm{Pe} = U$.

Figure 5.16 (b) shows the variation of $\bar{v}_f$ with U for fronts propagating in straight parallel rolls with $\mathrm{Le} = 0.1$. The flow field has a larger effect on the dynamics of the propagating fronts for this case. This is evident from the Péclet number which is now an order higher $\mathrm{Pe} = 10U$. The solid line is a curve fit through the red square symbols of the form $\bar{v}_f/v_0 = 1.30(U/v_0)^{0.4}$. The increased value of the scaling exponent is an indicator of the larger effect of fluid flow on the front.

For fronts traveling through idealized cellular flow fields with freeslip boundary conditions, theoretical scaling parameters were found at the two limits of fast reaction and fast advection ($\mathrm{Da} \gg 1, \mathrm{Pe} \gg 1$) and slow reaction and fast advection ($\mathrm{Da} \ll 1, \mathrm{Pe} \gg 1$). It was found

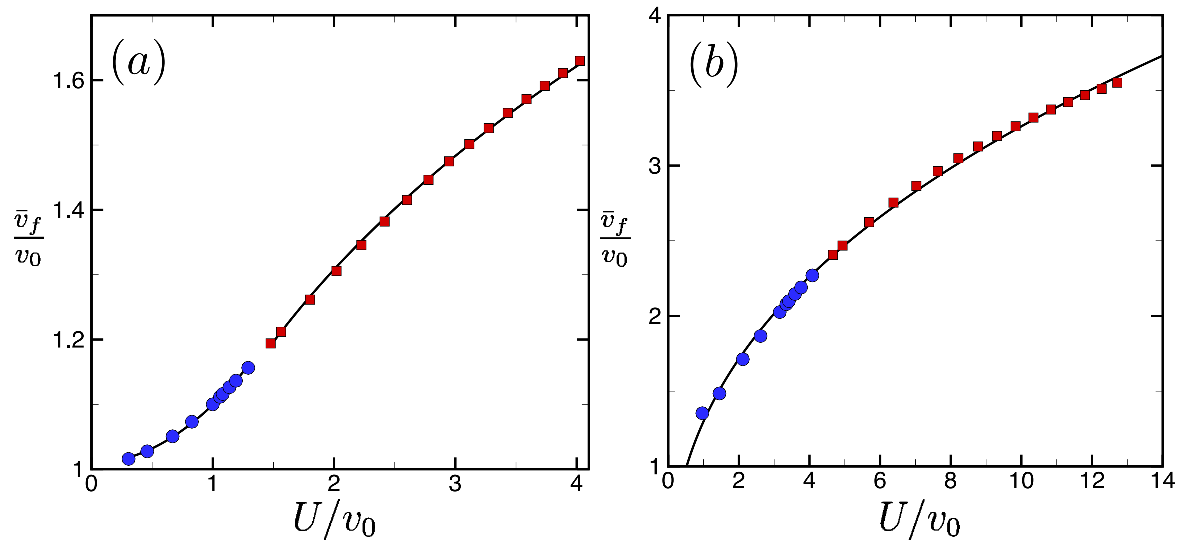

Figure 5.16: The variation of front velocity with the underlying fluid velocity through straight parallel convection rolls. The blue circles indicate $\mathrm{Da} > 1$ and the red squares indicate $\mathrm{Da} < 1$. (a) Shows the data for $\mathrm{Le} = 1$ where $\bar{v}_f/v_0 = 1 + 0.09(U/v_0)^2$ for $\mathrm{Da} > 1$ and $\bar{v}_f/v_0 = 1.06(U/v_0)^{0.31}$ for $\mathrm{Da} < 1$. For these results $0.375 \leq \mathrm{Da} \leq 4.9$, $0 < \mathrm{Pe} \leq 25$, $\mathrm{DaPe} = 9$, $v_0 = 6$. (b) Shows the data for $\mathrm{Le} = 0.1$. The solid line is a curve fit through the squares using $\bar{v}_f/v_0 = 1.30(U/v_0)^{0.4}$. For these results $0.375 \leq \mathrm{Da} \leq 4.9$, $0 < \mathrm{Pe} \leq 250$, and $v_0 = 6$.

that $\bar{v}_f$ scaled with the flow intensity or the characteristic fluid velocity as $\bar{v}_f \propto U^{\alpha_f}$, where α_f is the scaling exponent.

For slow reaction and fast advection limit ($\mathrm{Da} \ll 1, \mathrm{Pe} \gg 1$), the reaction time scale is the slowest and the advection and diffusion time scales are important. In this scenario, the RAD equation can be replaced with an effective reaction-diffusion equation with an enhanced diffusion coefficient, $\mathrm{Le}_{eff} = \sqrt{\mathrm{Le}U}$ [84]. Since, the front velocity scales as square root of the effective diffusion coefficient, for this limit we have $\bar{v}_f \propto U^{1/4}$ or $\alpha_f = 1/4$.

For fast reaction and fast advection ($\mathrm{Da} \gg 1, \mathrm{Pe} \gg 1$), the diffusion time scale is the largest and the two most important time scales that dictate the dynamics of front propagation are the advection and reaction time scales. The effective reaction rate for this case becomes $\xi_{\mathrm{eff}} = \mathrm{Da}^{-1/2}\xi$. The front velocity now scales as $\bar{v}_f \propto U^{3/4}$ or $\alpha_f = 3/4$.

The exponents that we have found are slightly larger than the exponent reported in the slow reaction limits. As discussed before in Sec. 3.2, we are away from these two limits since our Da $\sim \mathcal{O}(1)$ and we explore a range of Pe. Moreover, our flow fields are generated by Boussinseq convection and our material boundaries are rigid or no-slip. It was recently reported that fronts propagating through cellular rolls under free boundaries were faster than fronts propagating in rigid boundaries [85]. Since our Da $\sim \mathcal{O}(1)$, we get exponents which are near the theoretically predicted exponent of $\alpha_f = 1/4$. However, we have tried to reach the slow reaction limits of Da $\ll 1$, Pe $\gg 1$ by varying our reaction rate ξ.

Figure 5.17 plots the variation of the scaling exponent α_f with the reaction rate ξ for fronts propagating through fluids with Le $= 0.1$. We explored a range of $1 \leq \xi \leq 22$, which resulted in a range of Damköhler numbers $0.05 \leq$ Da $\lesssim 1$. For each value of ξ we performed numerical simulations to quantify the front velocity as a function of the fluid velocity in the range $3900 \leq$ Ra ≤ 5700. The range of Péclet numbers explored in the series is $145 \leq$ Pe ≤ 205. It is interesting that for $\xi = 1$ or Da $= 0.05$, we get a value of $\alpha_f = 0.3$ which is similar to the value of $\alpha_f = 1/4$ reported for Da $\ll 0.05$ and Pe $\gg 1$. As we increase the reaction rate ξ, we expect to reach the limit of Da $\gg 1$ and Pe $\gg 1$ where $\alpha_f = 3/4$. However increasing ξ is computationally challenging because increase in ξ makes the front thickness small and the front velocity large. We have not explored this computational bottleneck further and the highest ξ we could compute was $\xi = 22$.

Next we study the velocity of fronts propagating through chaotic flow fields as shown in Fig. 5.12-5.13. Figure 5.18 (b) shows the time variation of the front velocity for the chaotic flow field at Ra $= 7000$ and Le $= 0.1$. The front velocity for these radially propagating fronts is obtained by first obtaining the radial velocity at a direction v_r and then by calculating an azimuthal average of v_r. Again, we take the advantage of the fact that the integral at $z = 1/2$ is enough to quantify the front velocity without doing the full depth average. For

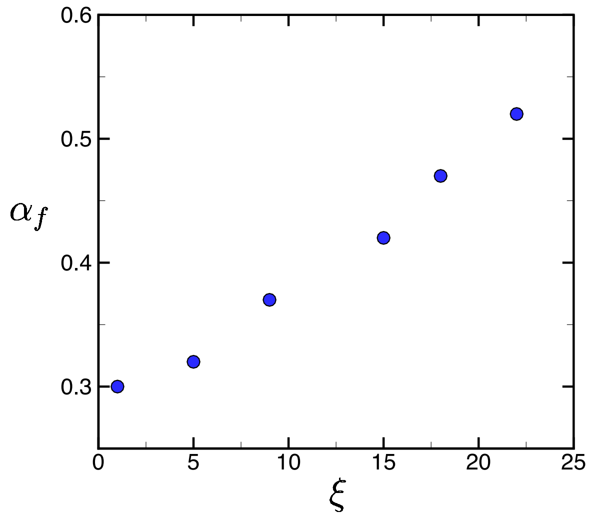

Figure 5.17: The scaling exponent α_f of the front velocity as a function of the reaction rate ξ for fronts traveling though straight-parallel convection rolls at Le$=$0.1. α_f at a particular value of ξ was determined by conducting seven numerical simulations for different values of U and then fitting the results with $\bar{v}_f \propto U^{\alpha_f}$ as in Fig. 5.16.

the chaotic flow fields we study this results in an error of less than 1%. Specifically we use a modified version of the bulk burning rate Eq. 3.7

$$v_r(\theta, t) = \int_0^\Gamma \frac{\partial}{\partial t} c(r, \theta, z{=}1/2, t) dr \tag{5.2}$$

to obtain v_r. The front velocity at an instant in time $v_f(t)$ is obtained by performing an azimuthal average on v_r. The effectiveness of using this approach is shown in Fig. 5.18 (a) where the black solid line is obtained from using this approach and the red solid line is obtained by using the full depth-averaged bulk burning rate equation in Eq. 3.7. The particular case investigated in Fig. 5.18 (a) is Ra $=$ 10000 and Le $=$ 0.1 which produces an asymptotic velocity of $\bar{v}_f = 7.86$. The irregularities and local dynamics of the chaotic flow field affects the front velocity and gives rise to oscillations in the time variation of the front velocity. To sample out the time variations we did three simulations of front propagation which were $t = 60$ times apart. The time variation of the three simulations is shown by the red, green and blue lines in Fig. 5.18 (b). The particular case investigated in Fig. 5.18 (b) is Ra = 7000 and Le = 0.1 which produces an asymptotic velocity of $\bar{v}_f = 6.41$. We then used the average of the three simulations to find the asymptotic front velocity. The black solid line is the average of the three numerical runs and the black dash-dotted line is the curve-fit of the form given by Eq. 3.8. We followed this procedure for all of our chaotic data.

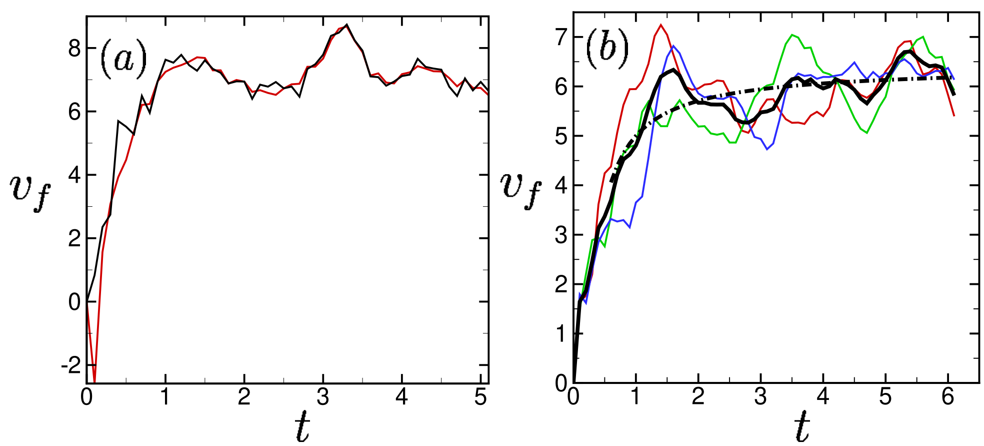

Figure 5.18: Temporal variation of the bulk burning rate front velocity v_f, comparing v_f obtained at the midplane with the depth averaged v_f and the determination of asymptotic front velocity $\bar{v}_f$ for a front propagating in a chaotic flow field. (a) Time variation of the front velocity for a front propagating in a chaotic flow field at Ra = 10000 and Le = 0.1. Comparing the front velocity obtained from the reduced definition of the bulk burning rate obtained from the azimuthal average of Eq. 5.2 at the horizontal midplane $z = 1/2$ with the full depth averaged definition in Eq. 3.7. The red solid line is the depth averaged front velocity while the black solid line is the front velocity obtained at the horizontal midplane. (b) Determination of asymptotic front velocity $\bar{v}_f$ for a front propagating in a chaotic flow field at Ra = 7000 and Le = 0.1. The front velocity is obtained by using a curve fit to Eq. 3.8, on the average data of three independent numerical runs. The three numerical runs are 60 vertical time units apart and are shown as red, green and blue lines. The average data is shown by the black solid line. The curve-fit through the data is shown by the dashed line. For these results, the asymptotic front velocity for (a) is $\bar{v}_f = 7.86$ and for (b) is $\bar{v}_f = 6.41$.

The variation of asymptotic front velocity $\bar{v}_f$ with the characteristic fluid velocity U for the chaotic flow fields is shown in Fig. 5.19. The open symbols are data for simulations in straight parallel rolls (previously shown in Fig. 5.16) for reference. All the filled symbols are for fronts propagating in chaotic flow fields. The square symbols are simulations at $\mathrm{Le} = 0.1$ and the circular symbols are for $\mathrm{Le} = 1$. The green data symbols are for $\mathrm{Ra} \geq 10^4$, where the flow field has undergone an oscillatory instability. The inverted triangles are for $\mathrm{Le} = 0.1$ and the diamond symbols are for $\mathrm{Le} = 1$. The dashed line through the the open squares and the dash-dotted line through the open circles are curve-fits for fronts propagating through straight parallel rolls discussed in Fig. 5.16. The solid lines are curve-fit through the data in the chaotic flow field. The solid line through the blue squares for $\mathrm{Le} = 0.1$ is of the form $\bar{v}_f = 1.29U^{0.48}$. The solid line through the red circles for $\mathrm{Le} = 1$ is of the form $\bar{v}_f = 3.77U^{0.27}$. Figure 5.19 (b) shows the same data plotted as a variation of Pe in a log-log plot. The power

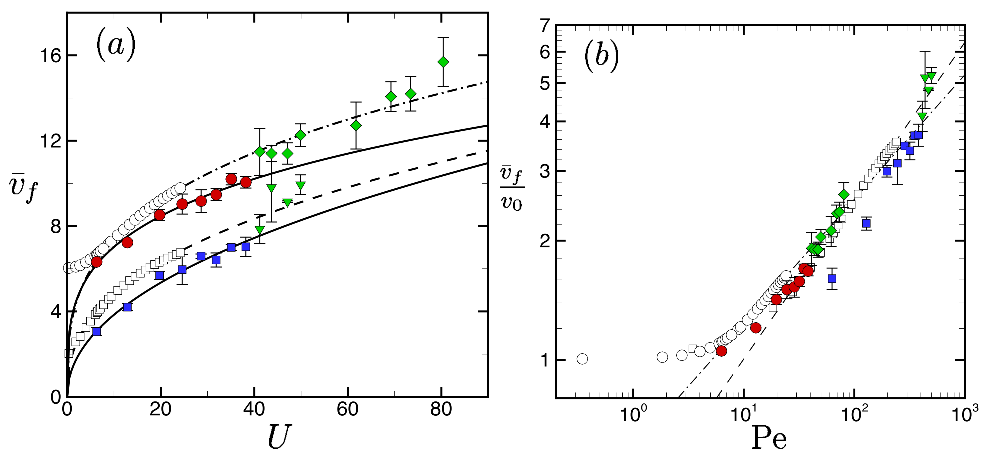

Figure 5.19: The asymptotic front velocity as a function of the characteristic fluid velocity U of the underlying flow field for fronts propagating through chaotic flow fields. Open symbols are for fronts traveling through a field of straight parallel rolls as shown in Fig. 5.16. The filled symbols are for fronts in chaotic flow fields in a cylindrical domain as shown in Fig. 5.12-5.13 where each data symbol is an average of 3 numerical simulations where the standard deviation is captured by the error bars. Circles and diamonds are for fronts propagating in flow fields with $\mathrm{Le} = 1$ and squares and triangles are for fronts propagating with in flow fields with $\mathrm{Le} = 0.1$. The green diamonds and triangles indicate flow fields that exhibiting oscillatory instability. The solid lines are curve fits through the data for fronts in chaotic flow field where $\bar{v}_f = 3.77U^{0.27}$ ($\mathrm{Le} = 1$) and $\bar{v}_f = 1.29U^{0.48}$ ($\mathrm{Le} = 0.1$). The dashed lines are curve fits through the data for fronts propagating in straight parallel rolls described in Fig. 5.16. (a) The front velocity as a function of the characteristic fluid velocity U. (b) The same data plotted as the normalized front velocity versus the Péclet number Pe in a log-log plot.

law scaling exponents for the different data are clearly shown by the straight lines in the plot. The different scaling exponents for fronts in straight parallel rolls and chaotic flow fields is tabulated in Table 5.1.

	Cellular flow	Chaotic flow
Le	α_f	α_f
1	0.31	0.27
0.1	0.40	0.48

Table 5.1: The scaling exponents α_f for several cases where $\bar{v}_f \propto U^{\alpha_f}$. These four cases are shown as the power-law curve fits in Fig. 5.19.

It is interesting to note that the fronts propagating through chaotic flow fields (filled symbols) are for the most part *slower* than fronts propagating through straight parallel rolls (open symbols) at the same value of U. The state of spiral defect chaos produces convection rolls of different orientation which slows down the front when compared with straight-parallel rolls. Front propagation is highly dependent on the orientation of the convection rolls as we will observe in the Sec. 5.2.2.

However, there is a significant increase in the front velocity when the flow field undergoes an oscillatory instability at Ra $\geq 10^4$ as shown by the green symbols. The fronts propagating through chaotic flow fields at Ra $\geq 10^4$ get a significant jump in the front velocity and get *faster* than fronts propagating in equivalent straight parallel cellular flow fields, at larger Ra. We could not maintain time independent cellular convection rolls in the rectangular domain with hot sidewalls for Ra > 6900. However, we have extended the curve-fits through the data to represent the equivalent scenario of straight parallel rolls at Ra > 6900 as shown by the dashed and dash-dotted line. This increment in front velocity for flow fields undergoing an oscillatory instability is related to the change in geometry of the front interface. The axially traveling oscillations along the convection rolls morphs the reaction interface and effectively increases the reaction area between products and reactants by imparting small scale features to the front interface. The geometry of the propagating fronts are further discussed in Sec. 5.2.3.

5.2.2 Orientation of convection rolls

The orientation of the convection rolls have a significant impact on the front propagation. For convective flow fields we use the local wave vector $\vec{q}(x, y, t) = (q_x, q_y)$ to determine the roll orientation. $\vec{q}$ is computed at the horizontal midplane $z = 1/2$ where q_x and q_y are the x and y components of the wave vector of the convection pattern. q_x and q_y are determined by taking spatial derivatives of the temperature field $T(x, y, z = 1/2, t)$ using an approach described in Ref. [86]. The local orientation of the convection rolls is defined as $\theta_l = \arctan(q_y/q_x)$ such that $0 \leq \theta_l \leq \pi$. At any time t we identify the reaction zone in the range of $0.1 \leq c \leq 0.9$. We then define the reaction zone angle ϕ in the spatial region consisting of the reaction zone to be

$$\phi = \begin{cases} \min\left(\tilde{\theta}, \left|\pi - \tilde{\theta}\right|\right), & \text{for } 0 \leq \theta \leq \pi \\ \min\left(\left|\pi - \tilde{\theta}\right|, \ \left|2\pi - \tilde{\theta}\right|\right), & \text{for } \pi < \theta \leq 2\pi \end{cases} \tag{5.3}$$

where $\tilde{\theta} = |\theta - \theta_l|$. Using Eq. 5.3 the reaction zone angle is over the range $0 \leq \phi \leq \pi/2$. The reaction zone angle is defined as the angle between the local wave vector $\vec{q}$ of the convection rolls and the radial direction in the region of the reaction zone in which the front is propagating with a velocity v_r.

To motivate the use of ϕ we first use an example of a front propagating radially in an extended field of straight parallel rolls as shown in Fig. 5.20. We will find the insights from this simplified problem to be very useful when discussing the orientation of chaotic convection rolls. Figure 5.20 shows fronts propagating in a field of straight parallel rolls in a rectangular domain which is extended in the y direction. The boundary conditions is the same as before, that is, all the quantities are periodic in the y-direction. The centers of the convection rolls are indicated by the solid lines. Figure 5.20 shows a front propagating radially outward at $\mathrm{Le} = 1$ and Fig. 5.20 (b) shows a front at $\mathrm{Le} = 0.1$. The fronts are initiated with the initial condition given by Eq. 3.4. The snapshots are taken at a time t when the front has reached its asymptotic velocity. The increased dependence of the flow field when $\mathrm{Le} = 0.1$ is evident by the complex geometry and elliptic structure of the front in Fig. 5.20 (b). The front shown in Fig. 5.20 (a) is less affected by the flow field which is apparent from the nearly circular geometry. Figure 5.21 shows the three dimensional visualization of the $c = 1/2$ level set at

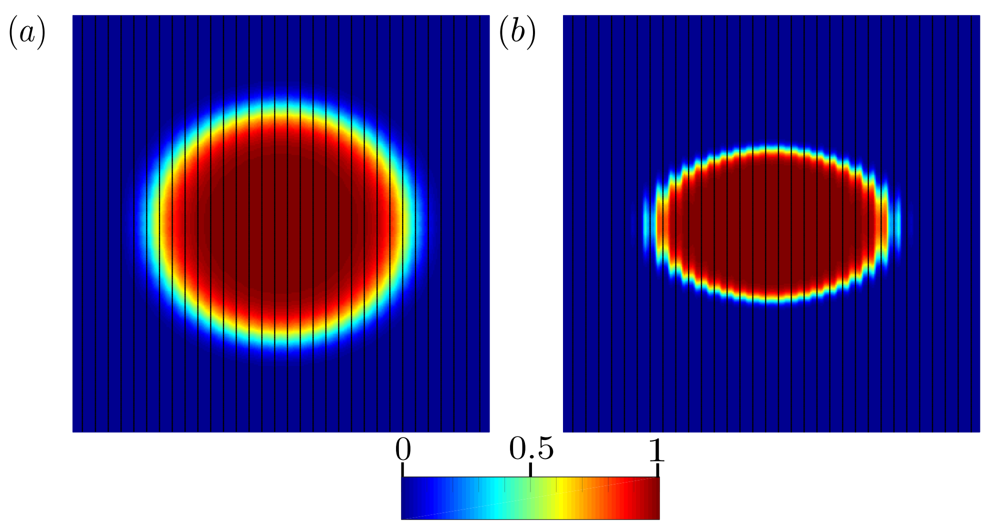

Figure 5.20: Snapshots in time of fronts propagating in a field of straight and parallel convection rolls at $\mathrm{Ra} = 2400$ in a box of aspect ratio $\Gamma = 30$, with (a) $\mathrm{Le} = 1$, $t = 1.5$ and (b) $\mathrm{Le} = 0.1$, $t = 2.0$ where t is measured from the initiation of the reaction at the center of the domain. The color contours are of the concentration field $c(x, y, z = 1/2, t)$ where red is pure products and blue is pure reactants. The solid black lines indicate the center line of the convection rolls.

three times from the initiation. Again, the increased dependence of the front on the flow field at smaller Lewis number is apparent in Fig. 5.21 (b) when compared with Fig. 5.21 (a).

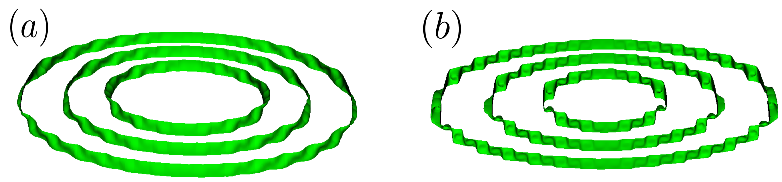

Figure 5.21: The three-dimensional spatial structure of the fronts shown in Fig. 5.20, where (a) Le $= 1$ and (b) Le $= 0.1$. The front is shown as the level-set surface where $c = 1/2$. The image is tilted at a small angle in order to improve visualization of the front. (a) $t = 1.0, 1.5, 2.0$, (b) $t = 1.0, 2.0, 3.0$.

The convection rolls in Fig. 5.20 are oriented in the x-direction and thus $\vec{q} = \vec{q_x}$ and $\theta_l = 0$. The reaction zone angle is easily calculated using Eq. 5.3 and varies from $0 \leq \phi \leq \pi/2$. The spatial variation of the reaction zone angle is shown in Fig. 5.22. The spatial average of the ϕ over the reaction zone is defined as $\langle\phi\rangle$. As expected the regions where the front is propagating in a direction perpendicular to the axis of the convection rolls yield $\langle\phi\rangle = 0$ (blue) while the regions where the front is parallel to the axis of the convection rolls yield $\langle\phi\rangle = \pi/2$. When $\langle\phi\rangle = \pi/2$, all the fluid velocity is acting in a direction perpendicular to the front propagation and as a result effectively the front propagates with the no-flow front velocity, $\bar{v}_f\,(\langle\phi\rangle = \pi/2) = v_0$. However, when $\langle\phi\rangle = 0$, the front velocity is enhanced.

The dependence of the front velocity on the reaction zone angle ϕ for fronts propagating in straight parallel rolls is shown in Fig. 5.23. Figure 5.23 (a) and (b) shows the variation of v_r as a function of $\langle\phi\rangle$ for fronts propagating with Le $= 1$ and Le $= 0.1$ respectively. As expected $\bar{v}_f(\langle\phi\rangle = \pi/2) = v_0$. The front velocity increases from $\langle\phi\rangle = \pi/2$ to $\langle\phi\rangle = 0$ with the maximum front velocity occurring at $\langle\phi\rangle = 0$. The increment is less for Le $= 1$ as expected since the front velocity is less affected by the fluid velocity as shown in Fig. 5.23 (a). The increment for Le $= 0.1$ is more and about twice the no flow front velocity as shown in

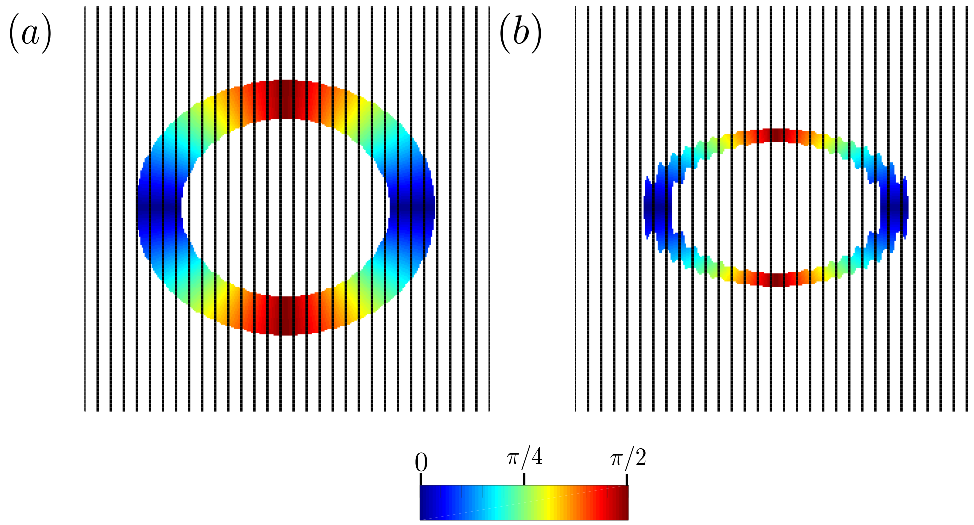

Figure 5.22: The spatial variation of the reaction zone angle ϕ for the fronts traveling through the straight parallel convection rolls shown in Fig. 5.20. ϕ is computed where the concentration is in the range $0.1 \leq c \leq 0.9$. The black lines indicate the location of the convection rolls. (a) Le$=$1 and (b) Le$=$0.1.

Fig. 5.23 (b). The oscillations in the data are related to the wavelength of the underlying convection rolls. The oscillations are exaggerated for Le $= 0.1$ where the effect of advection is significant. The solid lines through the data are Gaussian curve-fits of the form $v_r = 5.54 + 0.93e^{-\langle\phi\rangle^2}$ for Le $= 1$ and $v_r = 2.03(1 + e^{-2\langle\phi\rangle^2})$ for Le $= 0.1$. Currently, we do not have a theoretical explanation for these Gaussian trends and we leave this interesting problem for future research.

We next study the dependence of front velocity on convection roll orientation for the chaotic flow fields. Figure 5.24 shows the spatial variation of ϕ for chaotic flow fields at the horizontal midplane. The color contours are of ϕ and the black lines represent the line contour of $T = 1/2$ or the center of the convection rolls. The top panel shows the variation for Ra $= 3000$ where Fig. 5.24 (a) is for Le $= 1$ and Fig. 5.24 (b) is for Le $= 0.1$. The flow field pattern consists of patches of straight and curved parallel convection rolls. There are spatial regions where the flow field is disordered and contains defect structures such as dislocations, spirals,

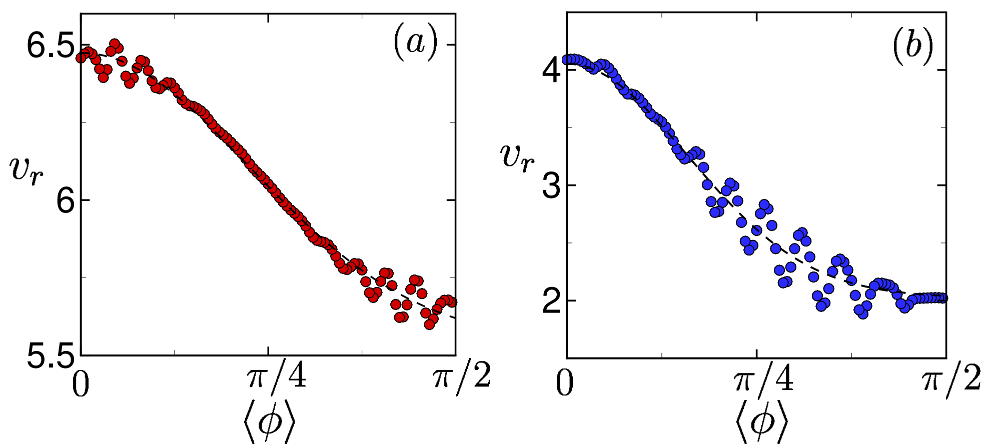

Figure 5.23: The instantaneous radial front velocity v_r as a function of the radially averaged reaction zone angle $\langle\phi\rangle$ for the fronts traveling through straight parallel rolls shown in Fig. 5.20, where (a) Le$=$1 and (b) Le$=$0.1. The dashed lines are Gaussian curve fits of the form (a) $v_r = 5.54 + 0.93e^{-\langle\phi\rangle^2}$ and (b) $v_r = 2.03(1 + e^{-2\langle\phi\rangle^2})$.

wall foci and grain boundaries. When Le $=$ 1, the reaction zone is thicker and spatial variation of the reaction zone angle is smoother as shown in Fig. 5.24 (a). When Le $=$ 0.1, the reaction zone is thinner and the spatial variation of the reaction zone angle is complicated due to the increased effect of advection.

The bottom panel is for Ra $=$ 9000 where Fig. 5.24 (c) is for Le $=$ 1 and Fig. 5.24 (d) is for Le $=$ 0.1 respectively. The flow field is now more disordered with fewer regions of parallel roll patches and many more defect structures. The spatial variation of the reaction zone angle is now much more complicated both in the radial and azimuthal directions.

Figure 5.25 shows the variation of the normalized radial velocity v_r/v_0 as a function of reaction zone angle ϕ for the flow fields in Fig. 5.24. The red circles are data for Le $=$ 1 and the blue squares are data for Le $=$ 0.1. The data shows a significant amount of scatter with the variation enhanced for Le $=$ 0.1 as expected.

Figure 5.25 (a) shows the variation of v_r against ϕ for the flow field at Ra $=$ 3000 as shown in the top panel of Fig. 5.24. The dislocation and defects in the chaotic rolls has morphed the

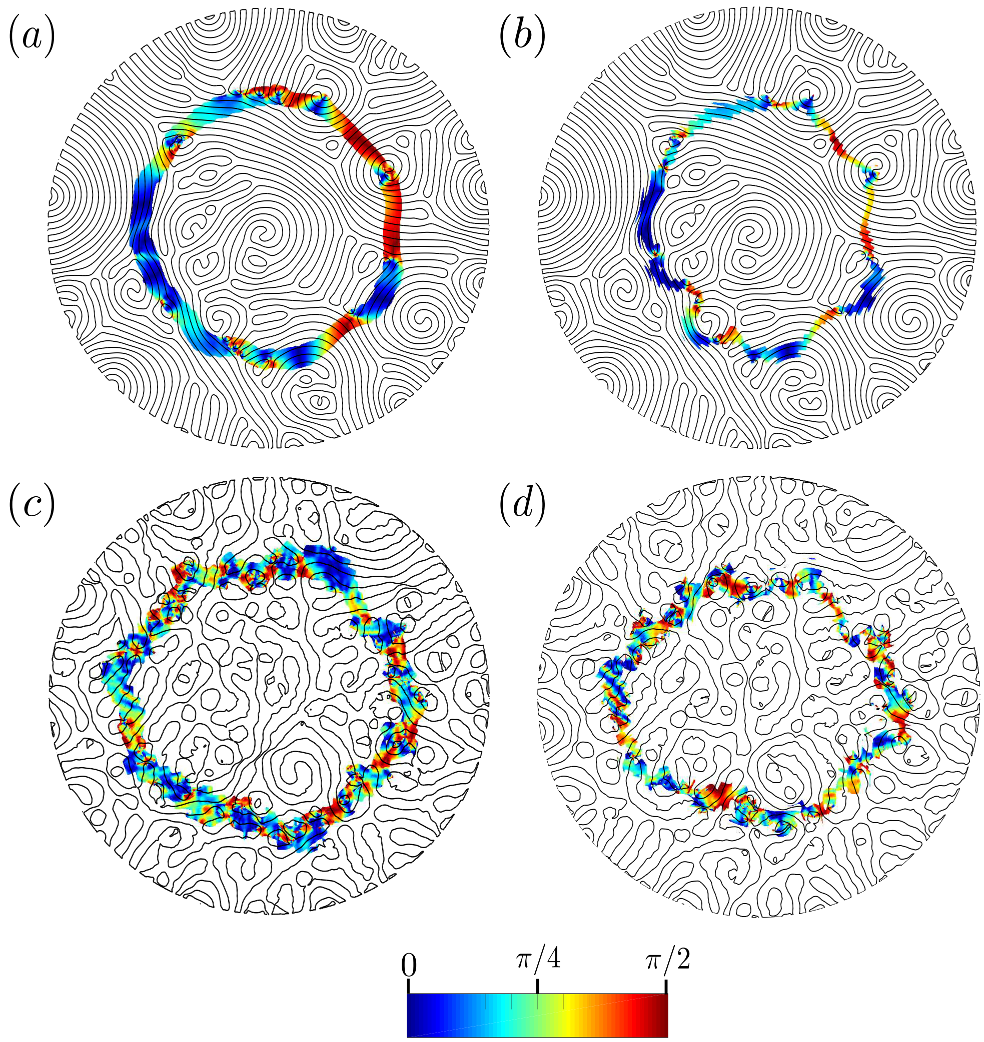

Figure 5.24: The spatial variation of the reaction zone angle ϕ for fronts propagating through chaotic convection rolls as shown in Figure 5.12-5.13. Color contours are of ϕ and the black lines are contours of $T(x, y, z = 1/2, t) = 1/2$ which indicates the location of convection rolls. The reaction zone angle is computed over the region where the concentration is within the range $0.1 \leq c \leq 0.9$. The top row is for $\mathrm{Ra} = 3000$ where (a) $\mathrm{Le} = 1$ and (b) $\mathrm{Le} = 0.1$. The bottom row is for $\mathrm{Ra} = 9000$ where (c) $\mathrm{Le} = 1$ and (d) $\mathrm{Le} = 0.1$.

smooth trend seen in Fig. 5.23. However a weak trend is still visible where v_r increases when ϕ decreases as expected. This suggests a weak trend of the front velocity on the reaction zone angle.

Figure 5.25 (b) shows the variation of v_r against ϕ for the flow field at $\mathrm{Ra} = 9000$ as shown in the top panel of Fig. 5.24. The data is now significantly scattered and there is no visible trend. There are no data points at $\langle\phi\rangle = \pi/2$ or $\langle\phi\rangle = 0$ which shows the absence of patches of straight parallel rolls. Moreover, we have a few instances where $v_r < 0$ indicating that the local fluctuations are pushing the front towards the center of the domain. These results suggest that the front velocity is not significantly dependent on the reaction zone angle. The flow field at Ra = 9000 consists of multiple defects and patches of straight parallel rolls are very few. The few instances of large magnitudes in v_r in Fig. 5.25 (b) coincide with locations where the local fluid velocity is large as shown in Fig. 5.5 (c) and (d). It is difficult to predict the location of large fluid velocity magnitudes as it is related to the topology of the flow pattern in a complicated way.

It is interesting to highlight that in Fig. 5.19 we found that the fronts propagating through straight parallel rolls were for the most part *faster* than their counterparts propagating in chaotic flow fields. The reason is as follows. For spatiotemporally chaotic rolls, the fronts encounter convection rolls at different orientations which effectively on an average reduce the front velocity, however for fronts propagating through straight parallel rolls, the convection rolls are always oriented in the direction of the front propagation. For example for Fig. 5.25 (b) the asymptotic front velocity $\bar{v}_f/v_0 = 1.68$ for Le = 1. This is obtained by the average velocity of all the red circles in Fig. 5.19 (b). The equivalent asymptotic front velocity for fronts propagating through straight parallel rolls is $\bar{v}_f/v_0 = 1.89$. The trend is similar for Le = 0.1 where $\bar{v}_f/v_0 = 3.7$ which is obtained by the average of all the blue squares in Fig. 5.19 (b). The equivalent asymptotic front velocity for fronts propagating through straight parallel rolls is $\bar{v}_f/v_0 = 4.32$. However, it is also interesting to note that there are regions where the fronts through the chaotic flow fields are locally faster than their counterparts in straight parallel rolls.

Overall, there are two competing mechanisms that affect the front propagation in disordered flows. These are the reaction zone angle and the geometry of the propagating fronts. A reaction zone angle away from zero *slows* down the front, while the increased complexity of the front interface increases the effective surface area of reaction and the front becomes faster. The geometry of the front interface is discussed in the next section.

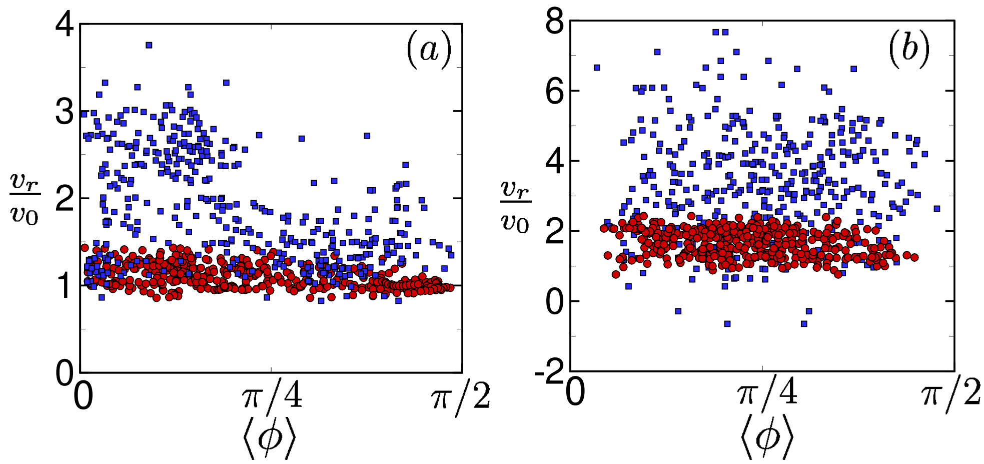

Figure 5.25: The instantaneous scaled radial front velocity $v_r(t)/v_0$ as a function of the radially averaged reaction zone angle $\langle\phi\rangle$ for a chaotic flow field, where the circles (red) are for Le = 1 and the squares (blue) are for Le = 0.1. (a) Ra = 3000, (b) Ra = 9000.

5.2.3 Geometry of fronts

In this section we quantify the geometry of the front interface. We use the level set of $c = 1/2$ at the horizontal midplane to locate the front. Figure 5.26 shows the fronts found in this manner at three instances of time starting from the initiation at the center. The top panel of Fig. 5.26 shows the front for Le = 1 where Fig. 5.26 (a) is at Ra = 9000 and Fig. 5.26 (b) is at Ra = 25000. The bottom panel of Fig. 5.26 are results for Le = 0.1 where Fig. 5.26 (c) is at Ra = 9000 and Fig. 5.26 (d) is at Ra = 13000. It is clear that the spatial structure of the front is extremely complex. The wrinkled front contains structures that are noncontagious and discontinuous. There are also spatially isolated patches of the $c = 0.5$ level set that are present. The wrinkling and spatial complexity increases for Le = 0.1 where the flow field has a significant impact on the front dynamics. These increased complexity is evident by comparing Fig. 5.26 (a) and (c), which are at the same Rayleigh number and the only difference being in the Lewis number.

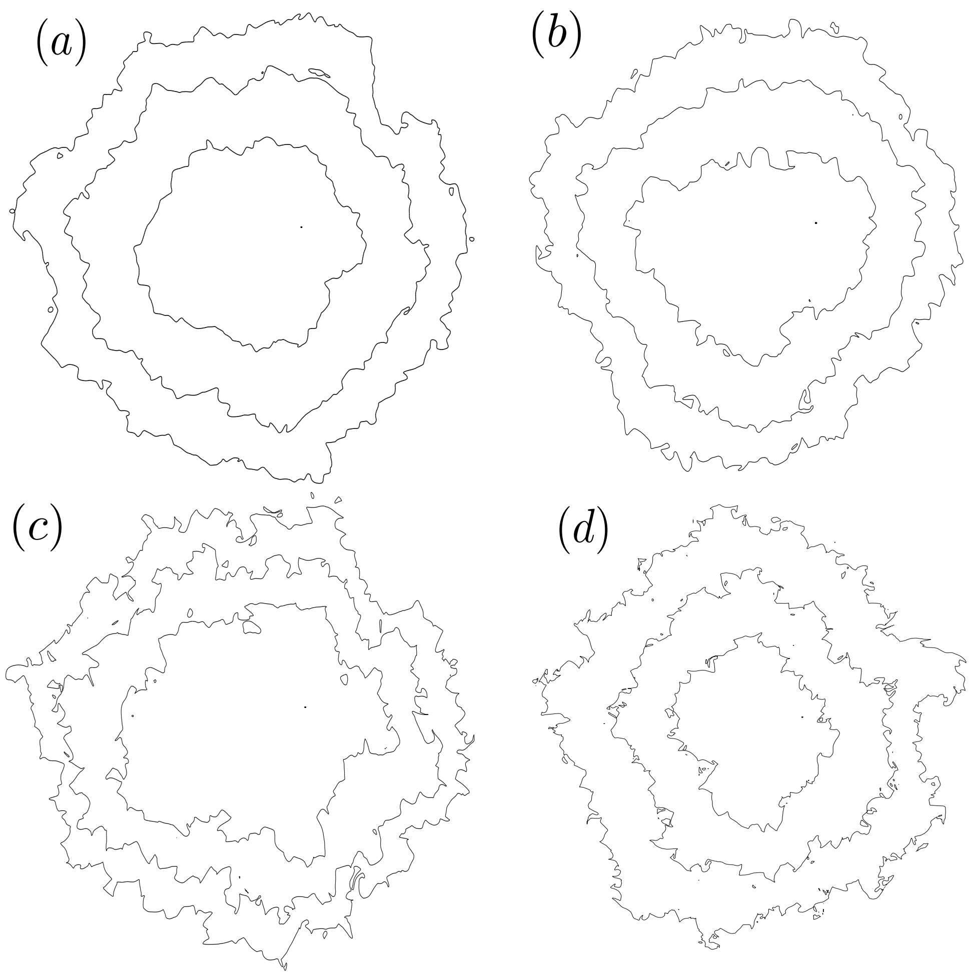

Figure 5.26: The geometry of fronts in chaotic flow fields shown in Fig. 5.13. The top row is for Le = 1 where (a) Ra = 9000 and (b) Ra = 25000. The bottom row is for Le = 0.1 where (c) Ra = 9000 and (d) Ra = 13000. The front is shown at the horizontal midplane using a black contour of the level-set $c(x, y, z = 1/2) = 1/2$. For each panel the front is shown for three different instances of time which appear as the three separate concentric objects. The front is shown at the following times: (a) $t = 2$, $t = 3$, $t = 3.7$; (b) $t = 1.5$, $t = 2$, $t = 2.4$; (c) $t=3$, $t=4$, $t=4.7$; (d) $t=2$, $t=3$, $t=4$.

In order to quantify the front geometry we use box counting dimension D_b [87]. The box counting dimension can be applied to complex, and not necessarily self-similar, geometries in two and three dimensions and thus is advantageous for our purposes. Many natural examples exist of objects that yield fractional values of the box counting dimension including fluid turbulence, cracking structures in a solid and the shapes of clouds, complex networks of blood vessels in the human body, coastlines and mountains to name a few [88, 89]. The idea behind box counting dimension is to compute the minimum number of boxes $N(\epsilon_b)$ of size ϵ_b to cover a geometrical object where features smaller than ϵ_b are ignored. For different values of ϵ_b one can then determines how $N(\epsilon_b)$ scales with ϵ_b as $\epsilon_b \to 0$. If this limit exists, the box counting dimension is given by

$$D_b = \lim_{\epsilon_b \to 0} \frac{\ln N(\epsilon_b)}{\ln(1/\epsilon_b)}. \tag{5.4}$$

We compute $N(\epsilon_b)$ over the range of numerically accessible values of ϵ_b and use $\ln N(\epsilon_b) \propto \ln(1/\epsilon_b)$ to determine if D_b has converged to a value for our smallest values of ϵ_b. We have conducted numerical tests to ensure that our computations yield the expected result for well known examples such as Euclidean areas, volumes, and various fractals such as the von Koch curve.

In all of our spectral element numerical simulations of propagating fronts in chaotic flow fields we have used 3072 hexahedral spectral elements with 16^{th} order Gauss-Lobatto-Legendre polynomials. This makes the smallest spatial feature that can be resolved in our computations have a length scale of approximately 0.08. Therefore, the smallest box size we use is $\epsilon_b \approx 0.08$.

Figure 5.27 is one of the results generated using this approach for a front propagating in a chaotic flow field where $R = 13000$ and $\text{Le} = 0.1$ (Fig. 5.26(c)). In this figure we have plotted the variation of $N(\epsilon_b)$ as a function of ϵ_b^{-1} on a log scale. As the value of ϵ_b decreases the results approach the straight dashed line, the slope of which provides the value of $D_b(t)$. For these results, we have $D_b(t) = 1.15$. We then compute the time variation of the box counting dimension of the front as it propagates radially outwards.

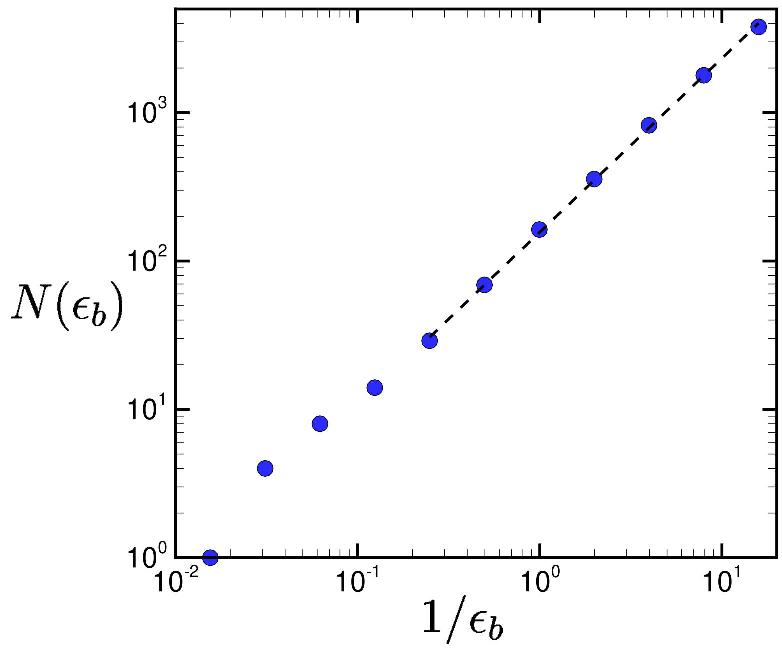

Figure 5.27: $N(\epsilon_b)$ as a function of ϵ_b for a front propagating in a chaotic flow field with Ra = 13000 and Le = 0.1 at a time $t = 3.6$ since the initiation of the reaction. The dashed line is a curve fit through the points which yields a box counting dimension of $D_b(t) = 1.15$ using Eq. 5.4

Figure 5.28 demonstrates the time variation of the box counting dimension and its dependence on the depth of the layer for the case of $R = 13000$ and Le = 0.1 which represents the most complex front we have explored here. Figure 5.28(a) shows the time-variation of the box counting dimension using the front that has been identified at the horizontal midplane $z = 1/2$. The front is located as the $c = 1/2$ level-set as shown in Fig. 5.26(d). The box counting dimension $D_b(t)$ fluctuates about its mean value of $\langle D_b \rangle = 1.15$ which is represented as the dashed line. The fluctuations about the mean have root-mean-squared value of 0.02.

$D_b(t)$ quickly approaches a steady value, on average, with small fluctuations about this mean value. This holds true for all of our calculations of $D_b(t)$.

In Fig. 5.28(b) the variation of the box counting dimension with the depth z. Results are presented for three different times during the front propagation where the front velocity has reached a steady value where circles (blue) are for $t = 2$, triangles (green) are for $t = 2.5$, and squares (red) are for $t = 3.0$. We have computed the box counting dimension at 11 equally spaced values of z over the range of $0 \leq z \leq 1$. The results indicate only a weak dependence on the value of D_b with the value of z used to determine location of the front. The front is actually the two dimensional ribbon structure shown in Fig. 5.29, however these results indicate that it is possible to estimate the box counting dimension of the front using only the slice of the front located at the midplane. This greatly reduces the amount of computations required to compute the box counting dimension of the fronts and we will use this approach in our analysis that follows.

Nevertheless, the true structure of the front is quite complex as shown in Fig. 5.29. The three green ribbon-like structures in Fig. 5.29 show the propagating front at three different times as it radially travels from the center of the domain outward. The entire image has been rotated to make it possible to visualize the intricate nature of the propagating front surface.

We have computed the box counting dimension of all of the fronts in the chaotic and weakly turbulent fluid flows that we have discussed. Figure 5.30 shows the variation of $\bar{D}_b$ with the reduced Rayleigh number ϵ. We define $\bar{D}_b$ using

$$\bar{D}_b = \langle D_b \rangle_t - 1. \tag{5.5}$$

The term $\langle D_b \rangle_t$ is the long-time average value of $D_b(t)$. The circles (red) and the diamonds

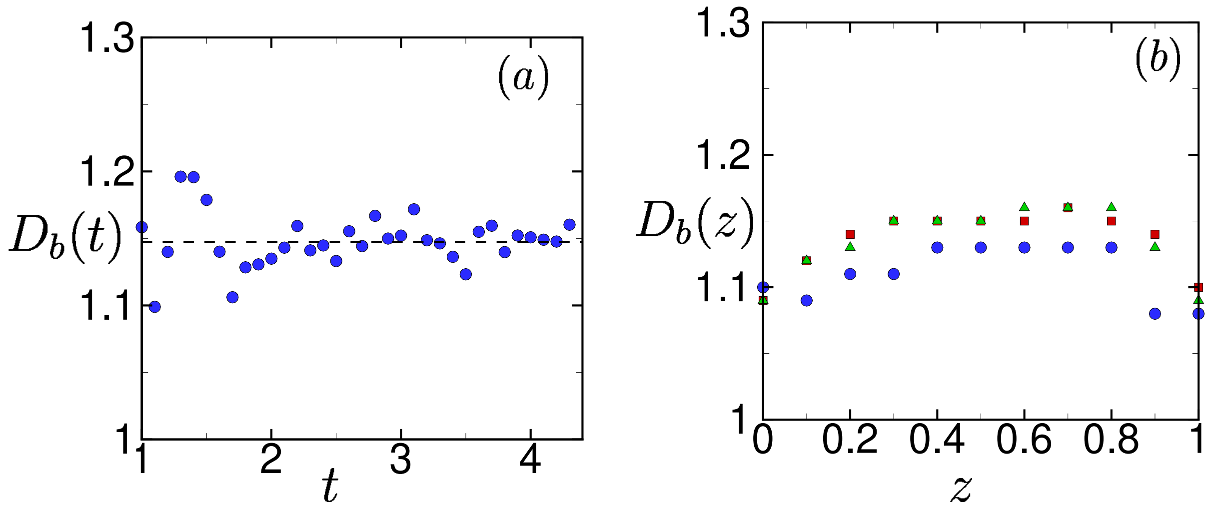

Figure 5.28: The temporal and depth variation of the box-counting dimension D_b. (a) The box counting dimension D_b as a function of time t using the front located at the horizontal midplane ($z = 1/2$) as shown in Fig. 5.26. The dashed line is the time averaged value of $\langle D_b \rangle_t = 1.15$. The root-mean-squared value of the fluctuations about the mean value is 0.02. (b) D_b as a function of the vertical coordinate z. Results are shown for three different times after the front has reached a steady front velocity where circles (blue) $t = 2.0$, triangles (green) $t = 2.5$, and squares (red) $t = 3.0$. For the results Ra = 13000, Le = 0.1, and images of the front are shown in Fig. 5.26(d).

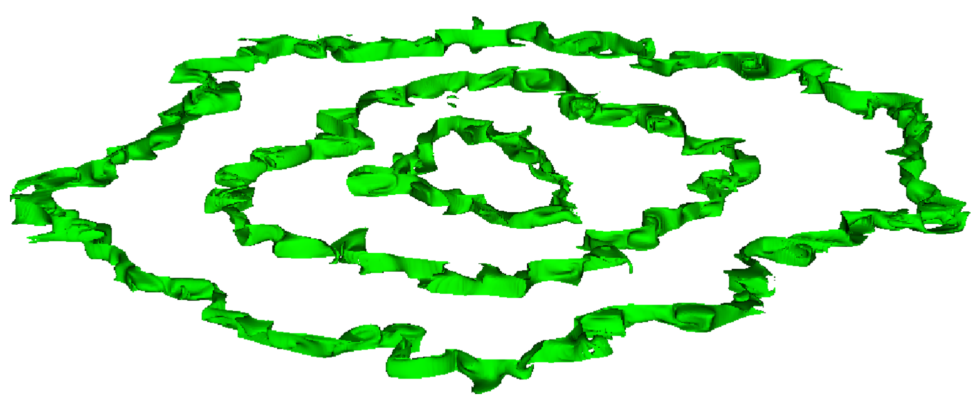

Figure 5.29: The three-dimensional spatial structure of the front in a chaotic flow for Le = 0.1 and Ra = 13000. The level-set of the concentration field at $c(x, y, z, t) = 1/2$ is shown in green at three different instances of time t where $t = 1, 2, 3$. The front is propagating from the center outwards and the domain is shown at an angle to show the spatial features of the front. This particular front is also represented in Fig. 5.13(b).

(green) are the results for Le = 1 and the squares (blue) and triangles (green) are for Le = 0.1. The diamonds and triangles (green) are for the weakly turbulent flows where the value of ϵ is above the threshold for the oscillatory instability. The error bars are the standard deviation of the dimension about its mean value. The variation of the dimension with the reduced Rayleigh number is described by the power-law scaling $\bar{D}_b \propto \epsilon^{\alpha_b}$ where the scaling exponent is $\alpha_b \approx 0.7$ for Le = 1 and $\alpha_b \approx 0.2$ for Le = 0.1. The curve fits are shown as the solid and dashed lines.

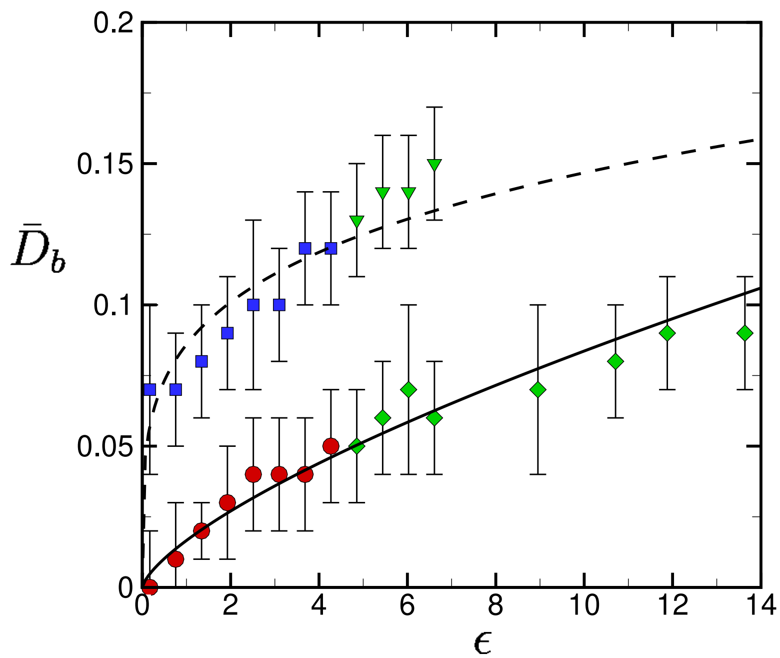

Figure 5.30: The variation of the reduced box counting dimension $\bar{D}_b$ with the reduced Rayleigh number ϵ. The squares (blue) and triangles (green) are for Le = 0.1 and the circles (red) and diamonds (green) are for Le = 1. Errors bars are included which represent the standard deviation about the mean value. The solid and dashed lines are power-law curve-fits through the data where $\bar{D}_b = 0.02\epsilon^{0.7}$ and $\bar{D}_b = 0.08\epsilon^{0.23}$, respectively. An oscillatory instability is present for $\epsilon \gtrsim 4.85$ which are indicated as the triangles and diamonds (green).

The box counting dimension exhibits an increasing trend with increasing ϵ, since the flow field becomes more complex with ϵ. Also, $\bar{D}_b$ for Le = 0.1 is always larger than $\bar{D}_b$ for Le = 1. This indicates that the stronger effect of advection of the flow field for a smaller

Lewis number increases the complexity of the front geometry.

For both the $\mathrm{Le} = 1$ and $\mathrm{Le} = 0.1$ results, the asymptotic front velocities $\bar{v}_f$ for the three largest values of ϵ shown in Fig. 5.30 exceed the front velocity through straight and parallel convection rolls with a reaction zone angle of zero. Figure 5.30 suggests that this front velocity enhancement is due, at least in part, to the increased complexity of the front geometry.

This enhancement to the front velocity is expected to increase as ϵ is increased further. However, using our results it is unclear if the power-law curve fits continue to be useful for much larger values of ϵ since the flow field characteristics are expected to change significantly as turbulence is approached.

It is interesting to compare our results with the results in the literature that find fractal dimensions of $D_f = 7/3$ for a wide range of conditions and flow fields [13, 31, 90, 91]. A value of $D_f = 7/3$ would be equivalent to $\bar{D}_b = 1/3$ using our notation. There is an increasing trend in our results that does not appear to be approaching a steady value for large ϵ. Although it is possible that our results may also approach a value of $1/3$ at larger ϵ, we are not able to make any quantitative predictions using our present results and this interesting question remains open.

Chapter 6

Front propagation with solutal feedback

In this chapter, we focus on reacting fronts whose products are less dense than the reactants and where the front travels horizontally with respect to gravity through a shallow layer of fluid. The results discussed in this chapter have been published in Ref. [39]. We assume that the reaction is isothermal such that the reaction does not remove or generate heat. Specifically, this makes the following changes in the governing equations with feedback shown by Eq. 2.14-2.16. We have $\eta = 0$, $\mathrm{Ra} \geq 0$ and $\mathrm{Ra}_s \geq 0$. The products, being less dense than the reactants, generate fluid motion due to buoyancy. We will refer to this two-way coupling between the concentration and the fluid flow as solutal coupling or feedback. The solutal coupling is two-way because the concentration changes affect the flow field which can then affect the concentration field and so on.

The chapter is organized as follows. We first explore propagating fronts with solutal feedback only, that is, in the absence of thermal convection $\mathrm{Ra} = 0$, in Sec. 6.1. All of the fluid motion in this case is a result of the solutal feedback caused by the density changes due to the chemical reaction. We are also interested in the front and fluid dynamics for small solutal driving where we use a perturbation approach, and for large solutal driving where we examine the presence of scaling ideas. This provides insights which we use to study fronts with solutal feedback that propagate through a field of convection rolls generated by

Rayleigh-Bénard convection in Sec. 6.3.

We use a two dimensional domain as shown in Fig. 6.1 to study solutal feedback in initially quiescent fluids and fluids undergoing Rayleigh-Bénard convection. The advantages of using a two dimensional domain is the ease of theoretical understanding of the feedback mechanism using stream-function and vorticity formulation as done in Sec. 6.2. The other advantage is that we can now increase the number of hexahedral spectral elements in the mesh as well as the spatial resolution within the limits of our computations. For this study we have used a Lewis number of $\mathrm{Le} = 0.01$ which we could not study for the three-dimensional domains in Ch. 5 due to computational constraints which are discussed in Ch. 4. When $\mathrm{Le} = 0.01$ the fluid advection is significantly more important than diffusion and the front is more dependent on the flow field. The front as usual is initiated in the left wall with pulled front initial conditions given in Eq. 3.3. The front then propagates towards the right as shown by the arrow in Fig. 6.1. For our results we use $\Gamma_x = 30$. For a few scenarios where $\mathrm{Ra}_s \gg 1$, we have extended the domain to $\Gamma_x = 60$ to quantify the front in its asymptotic state.

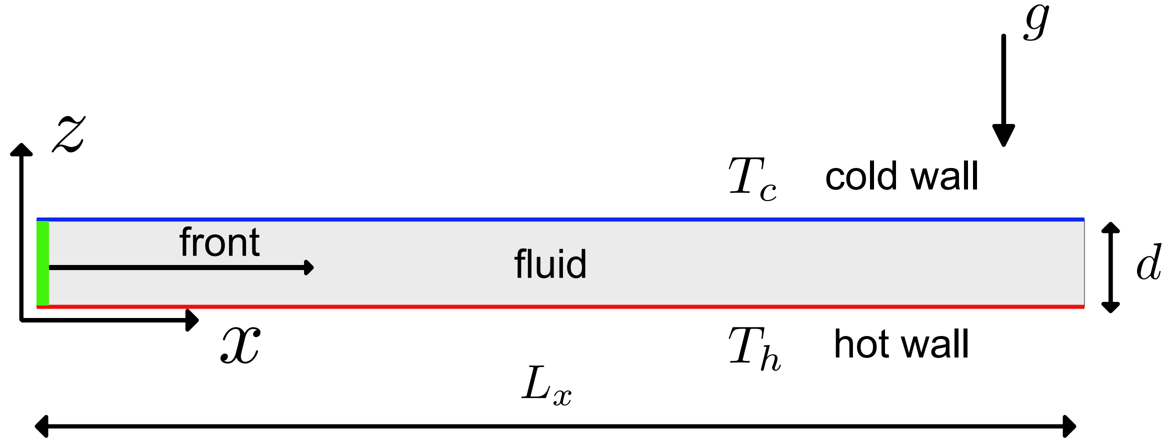

Figure 6.1: Schematic of the two-dimensional domain used to study propagating fronts with feedback. The fluid layer has a depth d and length L_x where the bottom wall is hot (red) at temperature T_h and the top wall is cold (blue) at temperature T_c. The coordinate directions (x, z) are shown where z opposes gravity g. The aspect ratio is $\Gamma_x = L_x/d$ and the reaction is initiated at the left wall and propagates to the right in the x direction.

6.1 Fronts with solutal feedback only

We first explore propagating fronts with solutal feedback through an initially quiescent fluid layer. Figure 6.2 illustrates several fronts over the range of solutal Rayleigh numbers $0 \leq \mathrm{Ra}_s \leq 3000$ where the thermal Rayleigh number $\mathrm{Ra} = 0$. The snapshots are taken at a time where the front has asymptotically reached a fixed shape and propagates toward the right at a constant velocity. Each panel shows a zoomed spatial view of the region $4 \leq x \leq 21.5$. The arrows are vectors of the fluid velocity that is generated by the solutal feedback.

Figure 6.2(a) shows a front without solutal feedback $\mathrm{Ra}_s = 0$. In this case, the front interface remains vertical, there is no generation of fluid motion, and the front velocity is given by Eq. 3.2 as $v_0 = 0.6$ for $\mathrm{Le} = 0.01$. Panels (b)-(h) are for increasing values of Ra_s. For $\mathrm{Ra}_s > 0$, a self-organized solutally induced convection roll is formed with a clockwise rotation that propagates with the front. All images are at time $t = 5$ where the front was initiated at $t = 0$, therefore the relative location of the fronts indicate that the front velocity increases with increasing Ra_s. As Ra_s increases, the front tilts to the right, is stretched over a larger distance, and develops positive and negative curvature. We will find the mixing-length L_s to be an useful quantity to quantify the stretching of the fronts. The mixing length is a measure of the axial distance over which the reaction occurs and is defined in terms of the vertical average of the concentration field as shown in Eq. 3.10 and Sec. 3.2.

The variation of $L_s(t)$ is shown in Fig. 6.3. Each curve illustrates the mixing length as a function of time for different values of Ra_s. In general, $\bar{L}_s$ increases monotonically with increasing Ra_s. Throughout this chapter we will find it useful to separate our results into the three ranges of low, intermediate, and large Ra_s where: $0 \leq \mathrm{Ra}_s \leq 1$ is low, blue, and uses circles; $1 < \mathrm{Ra}_s \leq 1000$ is intermediate, green, and uses diamonds; and $1000 < \mathrm{Ra}_s \leq 8000$ is large, red, and uses squares. Figure 6.3 (a) shows the mixing length L_s as a function of

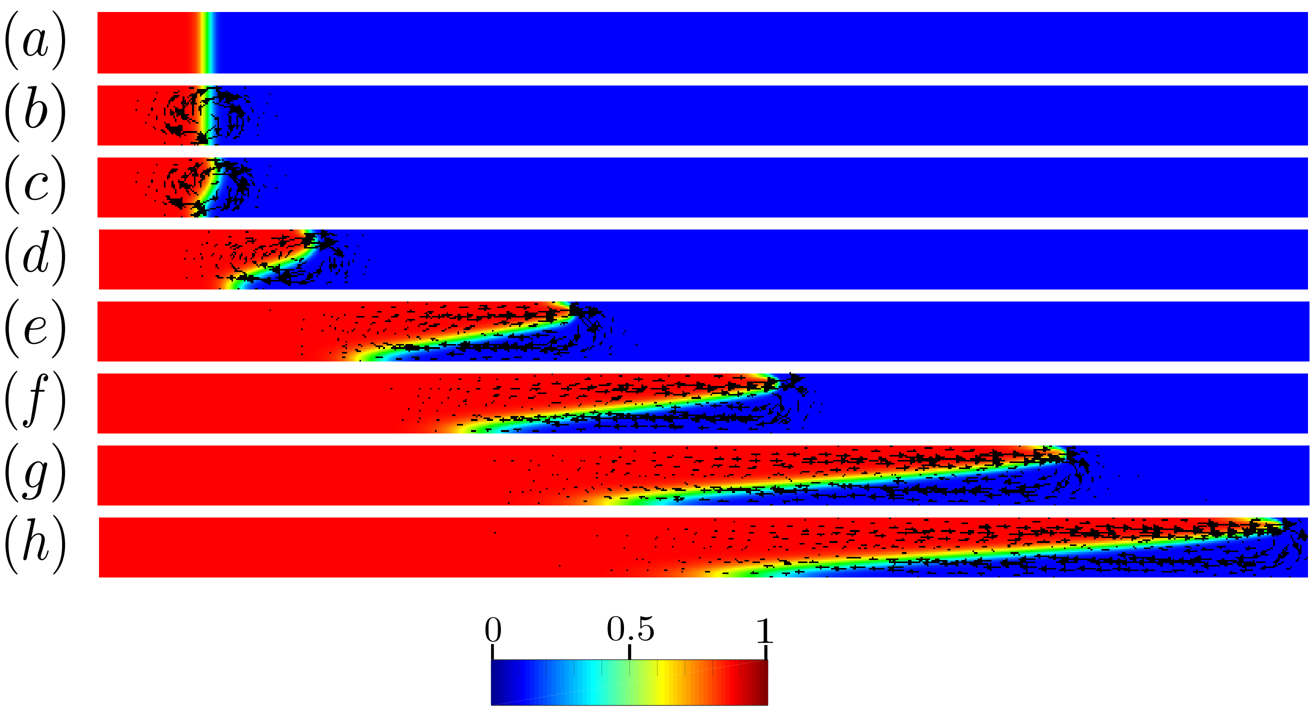

Figure 6.2: Fronts with solutal feedback propagating through an initially quiescent fluid, (a) without solutal feedback $\mathrm{Ra}_s = 0$ and (b)-(h) with solutal feedback $\mathrm{Ra}_s > 0$. Color contours are of the concentration c with the usual color convention where red is pure products and blue is pure reactants. The front is traveling from left to right. The arrows are the fluid velocity vectors generated by the front through solutal feedback. Only a portion of the layer is shown where the left boundary is at $x = 4$ and the right boundary is at $x = 21.5$. For all panels $t = 5$ and $\mathrm{Ra} = 0$. (a)-(h): $\mathrm{Ra}_s = \{0, 0.1, 10, 100, 500, 1000, 2000, 3000\}$.

time. As seen in the figure, L_s reaches its asymptotic value quite quickly in time. We call this asymptotic value as $\bar{L}_s$. Figure 6.3(b)-(c) illustrates the variation of $\bar{L}_s$ as a function of Ra_s. For positive values of Ra_s, the front tilts to the right and stretches which results in the increase in $\bar{L}_s$ as shown in Fig. 6.2(b)-(h). In Fig. 6.3(c) we show the same results on a log-log plot where the mixing length has been normalized using L_0. For small values of Ra_s, the normalized mixing length scales quadratically as $(\bar{L}_s - L_0)/L_0 = 8.55 \times 10^{-3}\mathrm{Ra}_s^2$ which is indicated by the solid line. For large values of Ra_s, the results follow a square root scaling given by $(\bar{L}_s - L_0)/L_0 = 0.316\mathrm{Ra}_s^{1/2}$. The square root scaling for large Ra_s (red points) is in agreement with previous studies of solutal feedback [64]. In addition, we have found a transition from the quadratic to square-root scaling for our results.

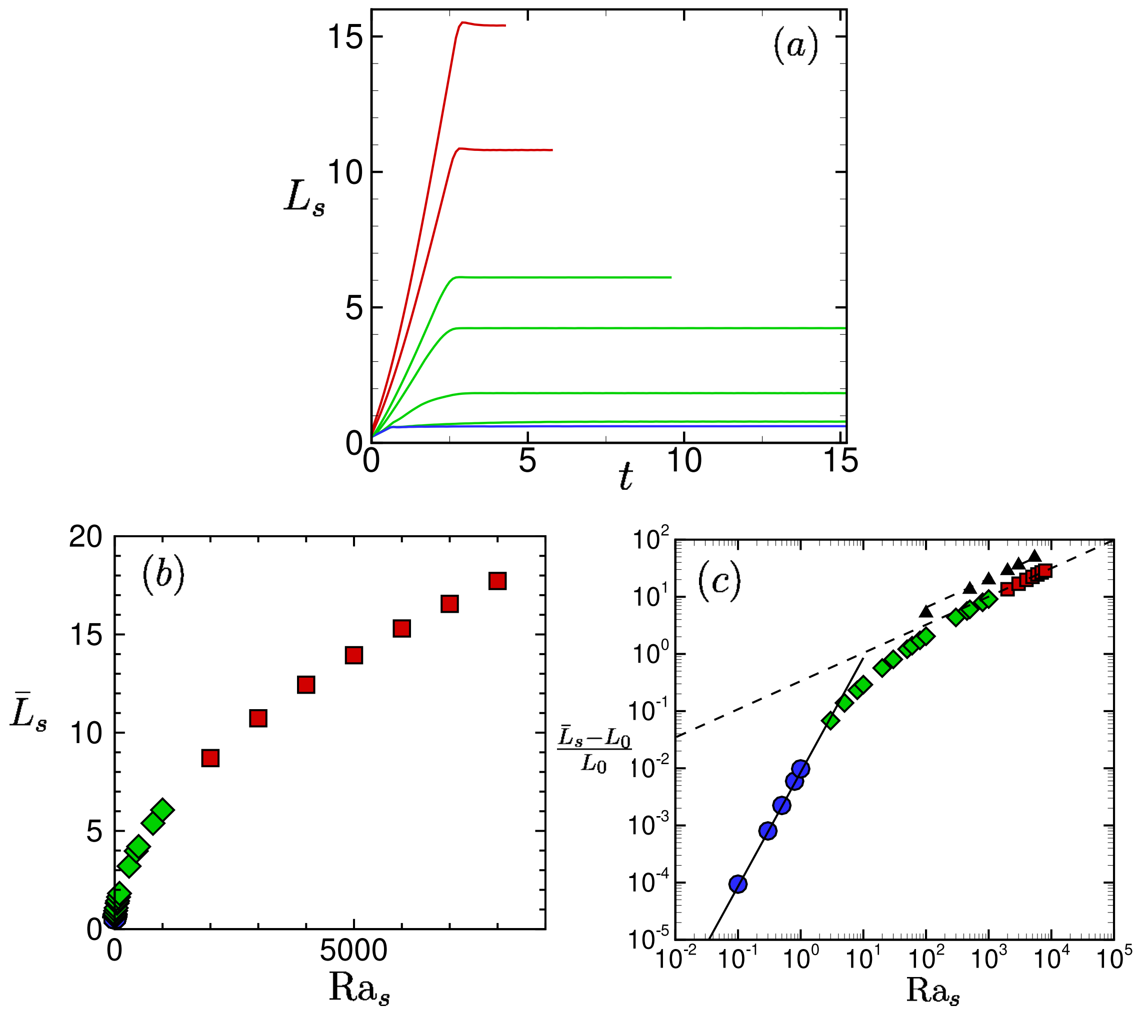

Figure 6.3: The variation of the mixing length L_s described using Eq. 3.10 in Sec. 3.2 for for fronts with solutal feedback propagating through an initially quiescent fluid ($\mathrm{Ra}_s > 0$ and $\mathrm{Ra} = 0$). Examples of front images are shown in Fig. 6.2. (a) L_s as a function of time t for $\mathrm{Ra}_s = \{1, 10, 100, 500, 1000, 3000, 6000\}$. (b) $\bar{L}_s$ as a function of Ra_s. (c) The scaled mixing length as a function of Ra_s where $L_0 = \bar{L}_s(\mathrm{Ra}_s = 0) = 0.598$. The solid line indicates $(\bar{L}_s - L_0)/L_0 = 8.55 \times 10^{-3}\mathrm{Ra}_s^2$ for $\mathrm{Ra}_s \leq 1$ and the dashed lines indicate $(\bar{L}_s - L_0)/L_0 = 0.316\mathrm{Ra}_s^{1/2}$ for $\mathrm{Ra}_s > 1000$. The black triangles are results using a cubic autocatalytic reaction.

The variation of the horizontal fluid velocity u with z is shown in Fig. 6.4(a)-(b). Each curve is $u(x, z, t)$ where the location x is chosen at a point where the horizontal fluid velocity is maximum at that time t. The position x coincides with a region near the leading edge of the front where the fluid velocity of the solutally induced convection roll is largest.

Figure 6.4(a) shows profiles of u for $0 \leq \mathrm{Ra}_s \leq 8000$. As described in Ref. [64] these curves yield a self-similar description at large Ra_s when the fluid velocity is scaled by its maximum value u_{max}. Our results also indicate this scaling as shown by the red curves in Fig. 6.4(b).

We also find a self-similar structure to the flow field at small Ra_s which is shown by the blue curves. The fluid velocity contours for the intermediate values of Ra_s do not collapse onto a single curve and represent the transition between the low and high Ra_s results. The horizontal and vertical dashed lines are included to illustrate the nearly antisymmetric shape of the low Ra_s results about the midplane where $z = 1/2$. The asymmetry of the curves increase as Ra_s is increased.

Figure 6.4(c)-(d) illustrate the shape of the front where the front has been identified as usual as the isocontour of the concentration field where $c = 1/2$. In this case, the fronts have been centered using the coordinate x_c where $x_c = x - (x_{\mathrm{max}} + x_{\mathrm{min}})/2$. $(x_{\mathrm{min}}, x_{\mathrm{max}})$ are the minimum and maximum values of x for the isocontour describing the front and, as a result, the center of each front is located at $x_c = 0$. Figure 6.4(d) shows the same results where we have scaled the front position such that the front location at the far right side is unity using $\bar{x}_c = x_c / x_{c,\mathrm{max}}$ where $x_{c,\mathrm{max}}$ is the largest value of x_c for each curve in Fig. 6.4(c). When plotted this way the fronts show a self-similar front shape for small (blue) and large (red) solutal Rayleigh numbers. The maximum horizontal velocity of the fluid increases with increasing values of Ra_s as shown in Fig. 6.4(a). It can also be seen that the location of this maximum occurs near the upper boundary.

In Fig. 6.5(a)-(b) we show how the fluid velocity scales with Ra_s where Ra_s varies over five orders of magnitude. The characteristic fluid velocity U is defined as usual and for this two

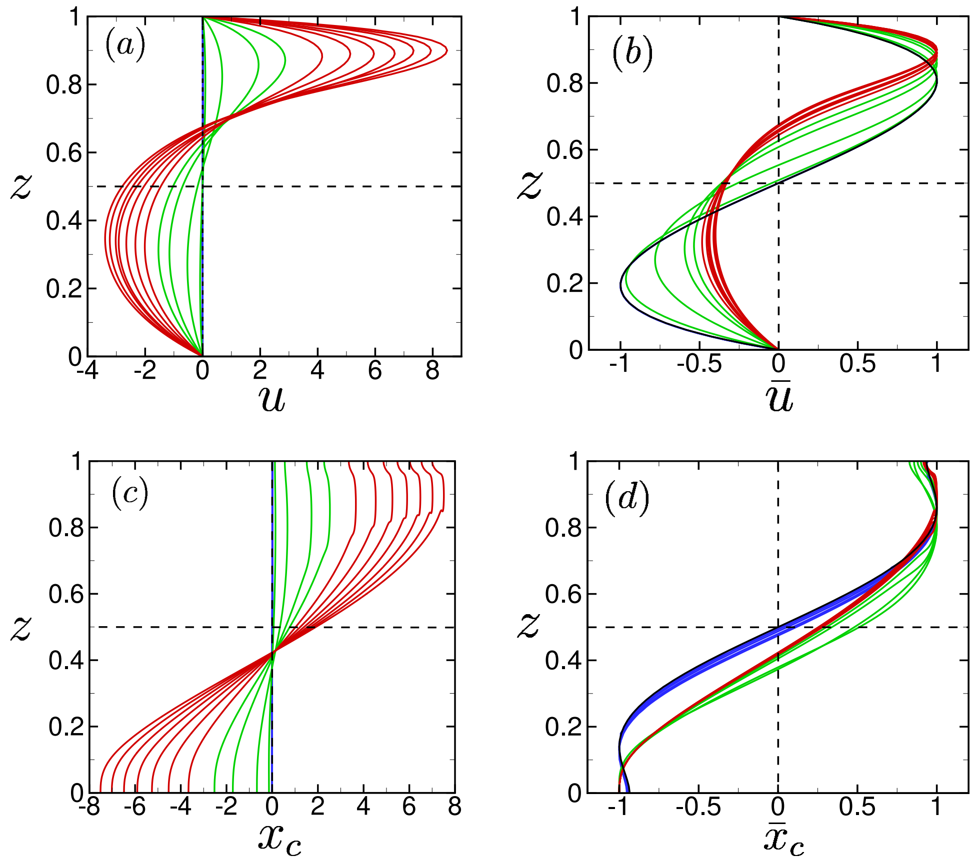

Figure 6.4: Self-similar features of the flow field and front in the presence of solutal feedback. All fronts have reached their asymptotic velocity and shape. The blue, green, and red curves are for small, intermediate, and large values of Ra_s where $0 \le \mathrm{Ra}_s \le 1$ (blue), $1 < \mathrm{Ra}_s \le 1000$ (green), $1000 < \mathrm{Ra}_s \le 8000$ (red). Images of the fronts are in Fig. 6.2. (a) The variation of the axial fluid velocity u with the vertical coordinate z. The slice in the z direction is taken at the x location where u is at its maximum value $u_{\max}$. (b) The same data plotted as a function of the normalized axial velocity $\bar{u} = u/u_{\max}$. (c) The variation of the front shape where the front is plotted as the isocontour where $c = 1/2$. The fronts are centered using x_c where $x_c = 0$ is the center location of the front. (d) The normalized front shapes using the scaled coordinate $\tilde{x}_c$. The black curves in (b)-(d) are for $\mathrm{Ra}_s = 10^{-3}$ which have been computed using a perturbation approach.

dimensional domain it is maximum value of the fluid velocity $|\vec{u}|$ over the entire domain when the front has reached its asymptotic propagating state. For fronts with $\mathrm{Ra} = 0$ we have $U \approx u_{\max}$ where $u_{\max}$ can be determined from Fig. 6.4(a).

Figure 6.5(a)-(b) indicates that for $\mathrm{Ra}_s \lesssim 1$ the flow field is in the Stokes flow regime where

Re $\ll$ 1 while for the larger values of Ra_s that we explore we have Re $\lesssim$ 10. There are

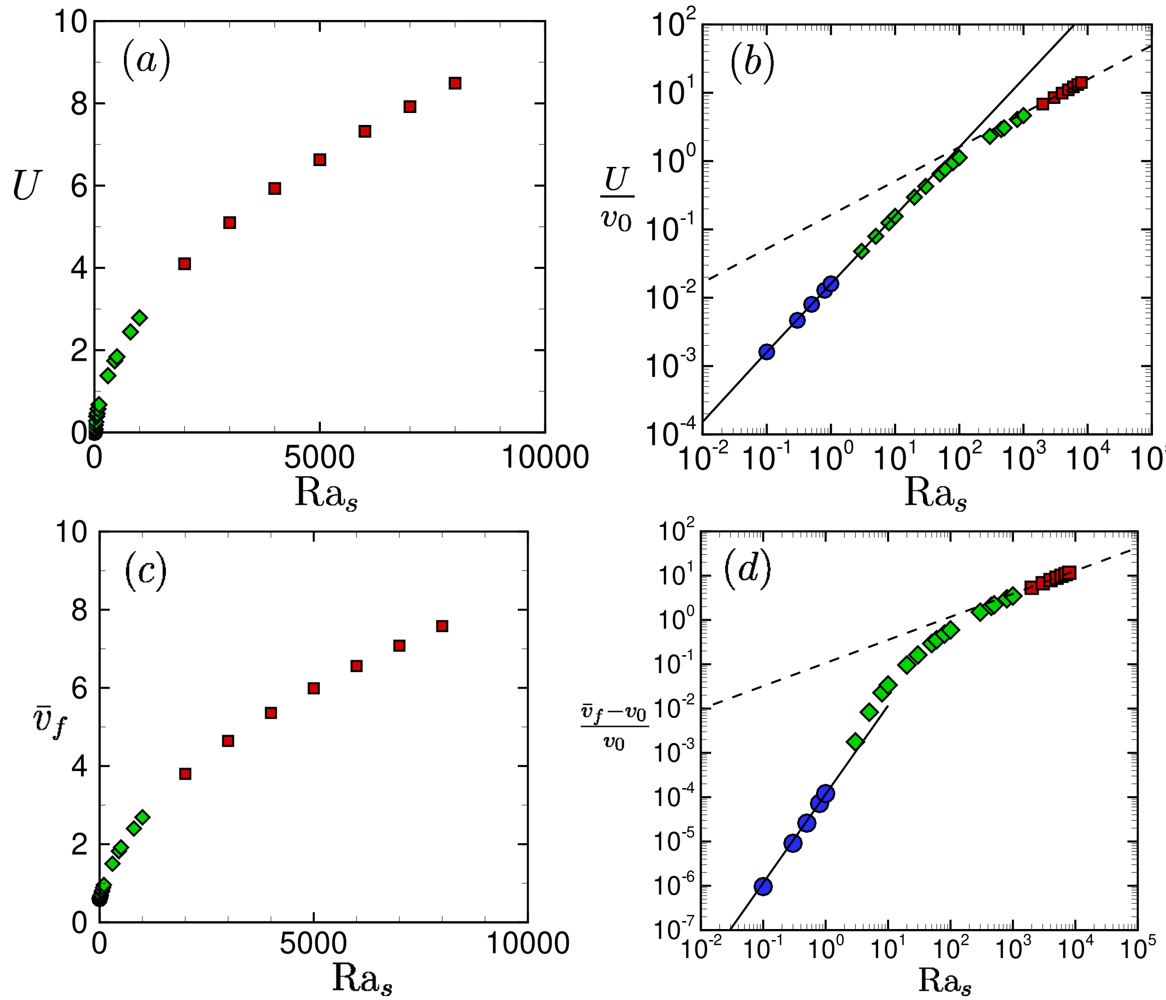

Figure 6.5: The variation of the characteristic fluid velocity U and the asymptotic front velocity $\bar{v}_f$ with the solutal Rayleigh number Ra_s for fronts propagating in the absence of thermal convection ($\mathrm{Ra}=0$) as shown in Fig. 6.2. (a) U as a function of Ra_s. (b) U/v_0 as a function of Ra_s where v_0 is the bare front velocity that is found when $\mathrm{Ra}_s=\mathrm{Ra}=0$. The solid line indicates $U/v_0 \propto \mathrm{Ra}_s$ for small Ra_s and the dashed line indicates $U/v_0 \propto \mathrm{Ra}_s^{1/2}$ for large Ra_s. (c) $\bar{v}_f$ as a function of Ra_s. (d) The scaled front velocity as a function of Ra_s. The solid line indicates a Ra_s^2 scaling and the dashed line indicates a $\mathrm{Ra}_s^{1/2}$ scaling. The circles (blue), diamonds (green), and squares (red) are results for small, intermediate, and large values of Ra_s, respectively.

several trends which can be seen in Fig. 6.5(a)-(b). For small values of the solutal Rayleigh number $\mathrm{Ra}_s \leq 1$, shown as the blue circles, the characteristic velocity U scales linearly with

Ra_s. The linear scaling $U = 9.6 \times 10^{-3}\mathrm{Ra}_s$ is indicated by the solid line in Fig. 6.5(b). The scaling then transitions to $U/v_0 \propto \mathrm{Ra}_s^{1/2}$ for larger values where $\mathrm{Ra}_s > 1000$ as shown by the red squares and the dashed line. Figure 6.5(c)-(d) illustrates how the asymptotic front velocity $\bar{v}_f$ varies with Ra_s. Figure 6.5(d) indicates that the scaled front velocity scales as $(\bar{v}_f - v_0)/v_0 = 1.635 \times 10^{-4}\mathrm{Ra}_s^2$ for $\mathrm{Ra}_s \leq 1$ as shown by the solid line through the circles (blue). The front velocity then transitions to a $\mathrm{Ra}_s^{1/2}$ scaling which is shown by the dashed line through the squares (red). Again the square root scaling of the velocities are in agreement with previous studies of solutal feedback in Stokes flow [64]. However, we found that for small solutal Rayleigh numbers, the fluid velocity scales linearly and the front velocity scales quadratically. As Ra_s increases, there is a transition to the square-root scaling.

6.2 Perturbation analysis for $\mathrm{Ra}_s < 1$

We explore the problem perturbatively for $\mathrm{Ra}_s \ll 1$ in order to gain insight into the scalings $U \propto \mathrm{Ra}_s$, $\bar{L}_s \propto \mathrm{Ra}_s^2$, and $\bar{v}_f \propto \mathrm{Ra}_s^2$ at small solutal Rayleigh number. In this section we describe the mathematical approach and the physical insights we can draw from using the perturbation approach.

We will first recast Eqs. 2.14-2.16 using a two-dimensional stream-function vorticity formulation to remove the pressure variable. The stream-function vorticity formulation also ensures that mass is conserved without the need of an extra equation. We note that Ra $= 0$ and $\eta = 0$. This yields

$$\sigma^{-1}\left(\frac{\partial \omega}{\partial t} - \frac{\partial \psi}{\partial z}\frac{\partial \omega}{\partial x} + \frac{\partial \psi}{\partial x}\frac{\partial \omega}{\partial z}\right) = \frac{\partial^2 \omega}{\partial x^2} + \frac{\partial^2 \omega}{\partial z^2} - \mathrm{Ra}_s\frac{\partial c}{\partial x}, \tag{6.1}$$

and

$$\frac{\partial c}{\partial t} - \frac{\partial \psi}{\partial z}\frac{\partial c}{\partial x} + \frac{\partial \psi}{\partial x}\frac{\partial c}{\partial z} = \mathrm{Le}\left(\frac{\partial^2 c}{\partial x^2} + \frac{\partial^2 c}{\partial z^2}\right) + \xi c(1-c) \tag{6.2}$$

where $\omega(x,z,t) = (\vec{\nabla} \times \vec{u}) \cdot \hat{y} = \partial u/\partial z - \partial w/\partial x$ is the y-component of the fluid vorticity vector and $\hat{y}$ is a unit vector in the y-direction. The stream function $\psi(x,z,t)$ is defined by $u = -\partial\psi/\partial z$ and $w = \partial\psi/\partial x$.

The vorticity and the stream function are related by the Poisson equation

$$\omega = -\left(\frac{\partial^2\psi}{\partial x^2} + \frac{\partial^2\psi}{\partial z^2}\right). \tag{6.3}$$

The boundary conditions for ω are computed using ψ and Eq. 6.3 evaluated at the boundaries. The initial conditions are no fluid motion such that $\psi = \omega = 0$ everywhere with a concentration profile given by $c(x,z,t=0) = e^{-(\xi/\mathrm{Le})^{1/2}x}$.

We expand ψ, ω and c as a power series using Ra_s as the small parameter

$$\psi(x,z,t) = \psi_0(x,z,t) + \mathrm{Ra}_s\psi_1(x,z,t) + \ldots \tag{6.4}$$

$$c(x,z,t) = c_0(x,z,t) + \mathrm{Ra}_s c_1(x,z,t) + \ldots \tag{6.5}$$

$$\omega(x,z,t) = \omega_0(x,z,t) + \mathrm{Ra}_s\omega_1(x,z,t) + \ldots \tag{6.6}$$

These expansions are inserted into Eqs. 6.1-6.3 and the equations are solved numerically for ψ_i, c_i, and ω_i at each order i of Ra_s^i using the appropriate boundary and initial conditions.

At $\mathcal{O}(0)$, Eq. 6.1 yields the trivial solution $\omega_0 = \psi_0 = 0$ indicating no fluid motion $u = w = 0$ as expected in the absence of solutal feedback. In this case, Eq. 6.2 becomes the reaction-diffusion equation for c_0,

$$\frac{\partial c_0}{\partial t} = \mathrm{Le}\left(\frac{\partial^2 c_0}{\partial x^2} + \frac{\partial^2 c_0}{\partial z^2}\right) + \xi c_0(1 - c_0). \tag{6.7}$$

The boundary conditions are $\partial c_0/\partial x = 0$ at $x = 0, \Gamma$ and $\partial c_0/\partial z = 0$ at $z = 0, 1$. The initial condition is $c_0(x,z,t=0)=e^{-(\xi/\mathrm{Le})^{1/2}x}$. For our boundary conditions and initial condition, c_0 is independent of z such that $c_0(x,t)$ and, as a result, Eq. 6.7 reduces further to the one dimensional reaction diffusion equation

$$\frac{\partial c_0}{\partial t} = \mathrm{Le}\frac{\partial^2 c_0}{\partial x^2} + \xi c_0(1-c_0). \tag{6.8}$$

This yields a vertically oriented front traveling with a front velocity of $v_0 = 2\sqrt{\mathrm{Le}\xi}$. For the FKPP nonlinearity there is not a general explicit analytical solution for $c_0(x,z,t)$ (*c.f.* [72, 73]) and Eq. 6.8 must be solved numerically.

The spatial variation of c_0 for a front at its asymptotic long-time state is shown in Fig. 6.6(a). The solid lines are equally spaced isocontours of c_0 with a spacing of $\Delta c_0 = 0.1$ where the contour to the furthest left is $c_0 = 0.9$ and the contour to the furthest right is $c_0 = 0.1$. The axial position of the front is plotted using the coordinate x_c where x_c is the position relative to the location of the isocontour of $c_0 = 1/2$. Therefore, using this convention, $x_c = 0$ is the location of the $c_0 = 1/2$ isocontour. We highlight that $c_0(x)$ is asymmetric about $x_c = 0$ which is evident by the variation of the spacing between the contour lines in Fig. 6.6(a). The mixing length $\bar{L}_s$ at $\mathcal{O}(0)$ is the axial distance between the 0.01 and 0.99 contours which yields a value of $L_0 = 0.608$.

The equations at $\mathcal{O}(1)$ are,

$$\sigma^{-1}\frac{\partial \omega_1}{\partial t} = \frac{\partial^2 \omega_1}{\partial x^2} + \frac{\partial^2 \omega_1}{\partial z^2} - \frac{\partial c_0}{\partial x} \tag{6.9}$$

and

$$\frac{\partial c_1}{\partial t} - \frac{\partial \psi_1}{\partial z}\frac{\partial c_0}{\partial x} = \mathrm{Le}\left(\frac{\partial^2 c_1}{\partial x^2} + \frac{\partial^2 c_1}{\partial z^2}\right) + \xi c_1(1-2c_0) \tag{6.10}$$

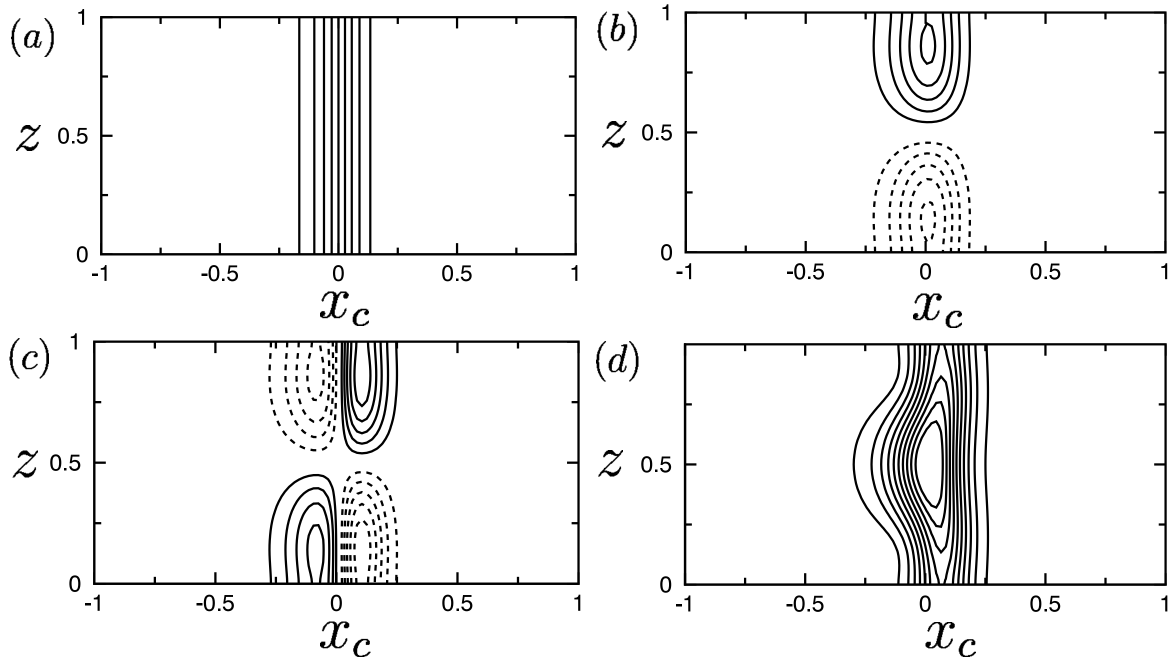

Figure 6.6: The spatial variation of concentration field at different orders of perturbation. The spatial variation of (a) c_0, (b) c_1, (c) $\frac{\partial c_1}{\partial t}$, and (d) c_2 for a front at its asymptotic state for $\mathrm{Ra}_s \ll 1$. Isocontours of the concentration are shown as solid (dashed) lines for positive (negative) values. The x axis is scaled such that the isocontour $c_0(x,t) = 1/2$ is located at $x_c = 0$. (a) The isocontours of c_0 are shown between 0.9 (left) and 0.1 (right) with a contour spacing of 0.1. c_0 is asymmetric about x_c. (b) The isocontours of c_1 are antisymmetric about $z = 1/2$. Solid and dashed lines are equally spaced contours in $0.014 \le c_1 \le 0.07$ and $-0.07 \le c_1 \le -0.014$, respectively. The closed contour near the top (bottom) is the largest (smallest) value and the magnitude decreases (increases) monotonically moving outward. (c) Isocontours of $\frac{\partial c_1}{\partial t}$ are antisymmetric about $z = 1/2$. Solid lines are equally spaced contours in $0.05 \le \frac{\partial c_1}{\partial t} \le 0.25$. Dashed lines are equally spaced contours in $-0.05 \le \frac{\partial c_1}{\partial t} \le -0.25$. (d) Equally spaced isocontours of c_2 between $0.001 \le c_1 \le 0.0145$. The largest value is located at the closed contour in the center and the magnitude decreases going outward. The curved front shape $c(x,z)$ that these variations in c_0, c_1 and c_2 yield for $\mathrm{Ra}_s = 10^{-3}$ is shown by the blue curve in Fig. 6.4.

where the vorticity and stream function are related by

$$\omega_1 = -\left(\frac{\partial^2 \psi_1}{\partial x^2} + \frac{\partial^2 \psi_1}{\partial z^2}\right). \tag{6.11}$$

The vorticity $\omega_1(x, z, t)$ is nonzero and is driven by the spatial variation of $c_0(x, t)$ in the x-direction as indicated by Eq. 6.9. This results in a clockwise vortex of fluid motion as shown by the streamlines in Fig. 6.7(a). The center of this vortex occurs at $x_c < 0$ indicating that it is slightly to the left of the axial location of the $c_0 = 1/2$ isocontour line.

Therefore, the leading order contribution to the fluid motion is at $\mathcal{O}(1)$. The magnitude of the maximum contribution to the fluid velocity at $\mathcal{O}(1)$, which we will refer to as $u_{1,\max}$, is the axial velocity that occurs near the top and bottom of the domain. The location of $u_{1,\max}$ is shown by the two circles (red) in Fig. 6.7(a) and has a value of $u_{1,\max} = 9.6 \times 10^{-3}$.

Using our definition of the characteristic velocity U as the maximum fluid velocity, we can represent U to $\mathcal{O}(1)$ as $U = u_{1,\max}\mathrm{Ra}_s$. This yields $U = 9.6 \times 10^{-3}\mathrm{Ra}_s$ which is indicated by the solid line in Fig. 6.5(b). The agreement is excellent with the results from the full numerical simulations shown as the circles (blue). Therefore, the linear scaling of the fluid velocity is due to the axial variation of the concentration of the bare front which drives the vorticity field.

Equation 6.10 indicates that the concentration c, through the variations of c_1, will now be altered from the vertical stripe structure of c_0 by the vortical flow field generated by ψ_1. The spatial variation of $c_1(x, z)$ is shown in Fig. 6.6(b). c_1 is asymmetric in the x-direction about $x_c = 0$ and is antisymmetric about the horizontal midplane $z = 1/2$. The antisymmetry about the midplane has several important implications.

The variations of $c_1(x, z, t)$ cause the front to tilt toward the right and to develop some curvature at $\mathcal{O}(1)$. However, the mixing length is computed using the vertical average of the concentration field given by Eq. 3.10. Since $c_1(x, z)$ is antisymmetric about $z = 1/2$, the z-average of c_1 will vanish and, as a result, the spatial variation of c_1 will not affect the value of the mixing length $\bar{L}_s$.

Similarly the variation of the front velocity $\bar{v}_f$ is also unaffected by the variations of c_1 because of symmetry. The $\mathcal{O}(1)$ contributions to the front velocity depend upon the z-average of $\frac{\partial c_1}{\partial t}$ as indicated by Eq. 3.6. The spatial variation of $\frac{\partial c_1}{\partial t}$ is shown in Fig. 6.6(c) illustrating that it is antisymmetric about the horizontal midplane. As a result, the z-average of $\frac{\partial c_1}{\partial t}$ will vanish and there will not be an $\mathcal{O}(1)$ contribution to the front velocity. At $\mathcal{O}(2)$ the equations are

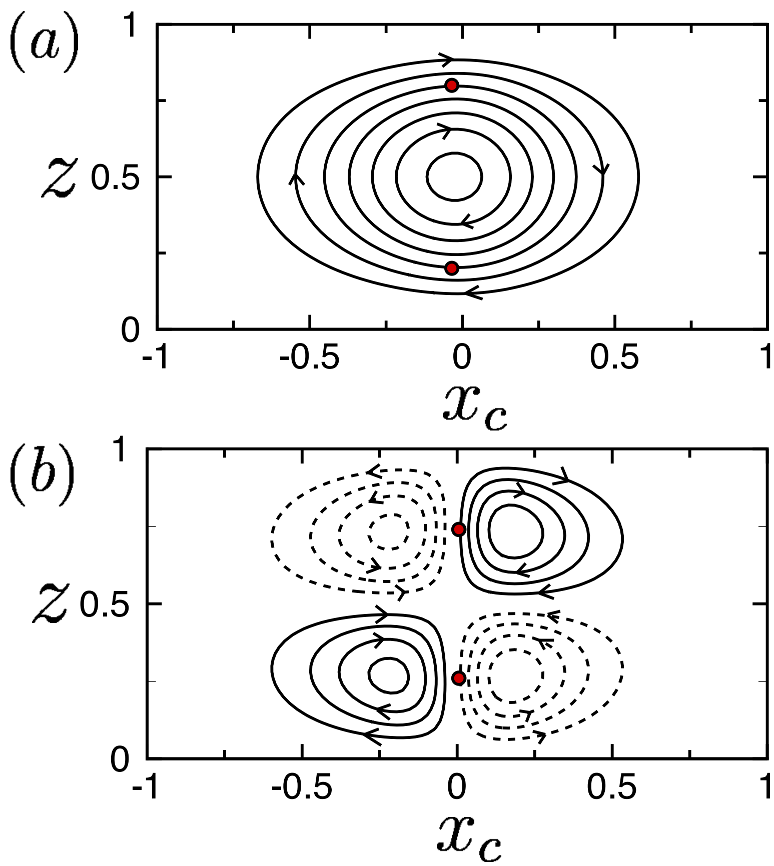

Figure 6.7: The spatial variation of the stream function at different orders of perturbation. The spatial variation of (a) $\psi_1(x, z)$ and (b) $\psi_2(x, z)$ for a front at its asymptotic state for $\mathrm{Ra}_s \ll 1$. Isocontours of the stream function are shown as solid (positive) and dashed (negative) lines and the arrows indicate the direction of fluid motion. The x axis is scaled as in Fig. 6.6. (a) ψ_1 is a vortical flow rotating clockwise. The circles (red) indicate the location of the maximum fluid velocity. Equally spaced isocontours are shown for $3 \times 10^{-3} \leq \psi_1 \leq 6 \times 10^{-4}$. ψ_1 is largest at the center of the vortex and decreases with distance from the center. (b) ψ_2 is a quadrupole of fluid flow. Equally spaced isocontours are shown for $-2 \times 10^{-5} \leq \psi_2 \leq 2 \times 10^{-5}$ where the largest positive and negative values are located at the centers of the vortex structures.

$$\sigma^{-1}\left(\frac{\partial\omega_2}{\partial t}-\frac{\partial\psi_1}{\partial z}\frac{\partial\omega_1}{\partial x}+\frac{\partial\psi_1}{\partial x}\frac{\partial\omega_1}{\partial z}\right)=\frac{\partial^2\omega_2}{\partial x^2}+\frac{\partial^2\omega_2}{\partial z^2}-\frac{\partial c_1}{\partial x}, \tag{6.12}$$

and

$$\frac{\partial c_2}{\partial t}-\frac{\partial\psi_2}{\partial z}\frac{\partial c_0}{\partial x}-\frac{\partial\psi_1}{\partial z}\frac{\partial c_1}{\partial x}+\frac{\partial\psi_1}{\partial x}\frac{\partial c_1}{\partial z}=\mathrm{Le}\left(\frac{\partial^2 c_2}{\partial x^2}+\frac{\partial^2 c_2}{\partial z^2}\right)+\xi(c_2(1-2c_0)-{c_1}^2) \tag{6.13}$$

with the relevant Poisson equation that is similar to Eq. 6.11 but is now in terms of ω_2 and ψ_2. In Eqs. 6.10 and 6.13 we have used the fact that c_0 is not a function of z to simplify the expressions. The spatial variation of $c_2(x,z)$ and $\psi_2(x,z)$ are shown in Figs. 6.6(d) and 6.7(b), respectively.

The stream function ψ_2 is a quadrupole of fluid motion as indicated by the streamlines in Fig. 6.7(b). From the streamlines it is evident that ψ_2 is asymmetric about its center in the x-direction and it is antisymmetric about the midplane $z = 1/2$. The center of ψ_2 aligns with the center of ψ_1 which is slightly to the left of $c_0 = 1/2$ contour. The largest magnitude of the fluid velocity at $\mathcal{O}(2)$ occurs in the lobes of the closed contours located at $x_c > 0$ and are indicated by the red circles. A plot of the total streamfunction ψ at $\mathcal{O}(2)$, where $\psi = \psi_0 + \mathrm{Ra}_s\psi_1 + \mathrm{Ra}_s^2\psi_2$, would yield an image similar to what is shown in Fig. 6.7(a) since $\psi_0 = 0$ and $|\psi_2| \ll |\psi_1|$.

The concentration field c_2 is asymmetric in both the x and z directions. In particular, z averages of c_2 and $\frac{\partial c_2}{\partial t}$ are nonzero and lead to contributions to $\bar{L}_s$ and $\bar{v}_f$. To $\mathcal{O}(2)$ this yields the following expression for the mixing length $(\bar{L}_s - L_0)/L_0 = 8.55 \times 10^{-3}\mathrm{Ra}_s^2$ which is indicated by the solid line in Fig. 6.3(c). Similarly, the front velocity to $\mathcal{O}(2)$ is given by $(\bar{v}_f - v_0)/v_0 = 1.635 \times 10^{-4}\mathrm{Ra}_s^2$ which is indicated by the solid line in Fig. 6.5(d). The agreement between the perturbation analysis and the full numerical simulations is excellent. Overall, these results indicate that the absence of $\mathcal{O}(1)$ contributions to $\bar{L}_s$ and $\bar{v}_f$ is due to the antisymmetry of $c_1(t)$ and $\partial c_1/\partial t$ about the horizontal midplane which leads to the quadratic scaling where this symmetry is broken.

Using the perturbation solution to $\mathcal{O}(2)$ we can also represent the axial fluid velocity and the front shape for $\mathrm{Ra}_s \ll 1$. These are shown in Fig. 6.4(b) and (d) for the case of $\mathrm{Ra}_s = 10^{-3}$ by the solid black lines. The perturbation results are in excellent agreement with the results from the full numerical simulations.

6.2.1 Numerical approach used for perturbation analysis

In this section we describe our numerical approach used to simulate the equations discussed in the perturbation analysis for $\mathrm{Ra}_s \ll 1$. The equations for ψ, c, and ω are numerically solved to $\mathcal{O}(2)$. We utilize a fully-explicit finite-difference approach that is first order accurate in time and second order accurate in space. We numerically solve Eqs. 6.7, 6.9-6.13 with the appropriate boundary and initial conditions described in Sec. 6.2. We use an equally spaced grid where $\Delta x = \Delta z = 0.02$ on a domain with an aspect ratio of $\Gamma_x = 12$. For time derivatives we use a first-order forward Euler time difference with a time step of $\Delta t = 1 \times 10^{-4}$. For spatial derivatives we used second order central time differencing.

We use the following procedure to evolve forward the variables for the concentration, stream function, and vorticity from time step n to $n+1$ at each order of Ra_s. We evolve the equations in the sequence $\mathcal{O}(0)$, $\mathcal{O}(1)$, and then $\mathcal{O}(2)$.

We first evolve forward Eq. 6.7 for the concentration to yield its value at the next time step $c_0^{(n+1)}$. We next solve Eq. 6.9 for the vorticity $\omega_1^{(n+1)}$ at all interior grid points. The stream function $\psi_1^{(n+1)}$ is then evaluated over the entire domain using Eq. 6.11 and a Gauss-Seidel iterative solver. With $\psi_1^{(n+1)}$ computed, we then evaluate the vorticity $\omega_1^{(n+1)}$ at the boundaries using Thom's formula [92, 93]. The concentration $c_1^{(n+1)}$ is then evaluated using

Eq. 6.10.

A similar procedure is followed at $\mathcal{O}(2)$. The vorticity $\omega_2^{(n+1)}$ at all interior points is computed using Eq. 6.12 and $\psi_2^{(n+1)}$ is computed over the entire domain using the Poisson equation relating the stream function and vorticity at $\mathcal{O}(2)$. Finally, $\omega_2^{(n+1)}$ is computed at the boundaries using Thom's formula and $c_2^{(n+1)}$ is evaluated over the entire domain using Eq. 6.13. We repeat the procedure to integrate the concentration, stream function, and vorticity variables forward in time.

6.3 Fronts with solutal feedback in convective flow fields

In this section we discuss how solutal feedback affects a front that propagates through a cellular convective flow field. In order to establish a convective flow field we used a thermal Rayleigh number of Ra = 3000. We first ran a long-time simulation of the flow field at this value of Ra to establish a steady field of counterrotating convection rolls over the entire domain. We accomplished this by using a hot-wall boundary condition at the sidewalls of the domain as usual. We start with initial conditions such that we get 30 pairs of counterrotating convection rolls as before. For Rayleigh number Ra = 3000 we get $U_c = 10.81$ as shown in Fig. 5.2 and Fig. 5.4. We write U_c to denote the characteristic fluid velocity caused by Rayleigh-Bénard convection in the absence of solutal feedback. Like before in Ch. 5, our Damköhler number of $\mathrm{Da} = \xi/U_c \approx 1$ which indicates that the convection and reaction time scales are comparable. Unlike before, here we take the advantage of high spatial resolution to run simulations at Le = 0.01. This yields a Péclet number of $\mathrm{Pe} = U_c/\mathrm{Le} \approx 1000$ indicating that the thermal convection driven fluid velocity is significant. Snapshots of the flow fields and propagating fronts are shown in Fig. 6.8.

Figure 6.8(a) shows a front for $\mathrm{Ra}_s = 0$ where there is no solutal feedback which results

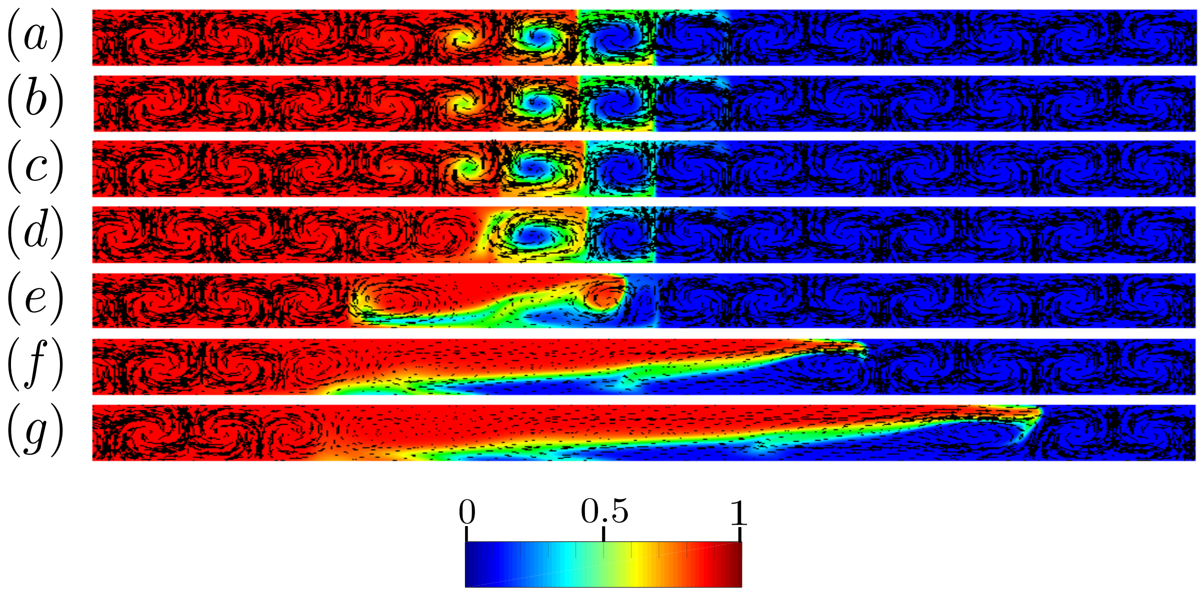

Figure 6.8: Fronts traveling through a convective flow field with solutal feedback. The Rayleigh number is fixed at the value of $\mathrm{Ra}=3000$ for all the panels and each panel is for a different value of Ra_s at time $t=3$. Color shows concentration (c) where red is products ($c=1$) and blue is reactants ($c=0$). The black arrows are of the fluid velocity $\vec{u}$. (a)-(g): $\mathrm{Ra}_s=\{0,100,500,700,1000,2000,3000\}$, respectively. A zoomed-in view is shown where $3\leq x\leq 17$.

in an unchanging flow field as shown. In addition, it is clear that the front dynamics are affected by the flow field which causes it to spiral toward the cores of the convection rolls while propagating toward the right.

Figure 6.8(b)-(g) shows results for $\mathrm{Ra}_s > 0$ where there is a complex interplay between the thermal convection and the solutal feedback caused by the reacting front. For small values of Ra_s, the solutally induced convection roll is weak compared to the convective rolls. As a result, panels (a) and (b) of Fig. 6.8 are quite similar. However, as Ra_s increases the strength of the solutal convection roll increases and its interactions with the convection rolls causes distortions in the flow field near the front as shown in Fig. 6.8(c)-(d). For further increases in Ra_s, the solutal convection roll dominates the thermal convection rolls as shown in Fig. 6.8(e)-(g). For large values of Ra_s, the solutal convection roll extends for many convection roll widths and annihilates the convective motion over the region spanned by the front. After the front passes through a location, the convection rolls reemerge due to the convective instability. This is illustrated by the convection rolls to the left of the front in the region occupied by pure products. The convection rolls formed propagate inside the spatial void which has been left by the solutally driven fluid roll and which now consists of pure products. This front of convection rolls is an example of a pattern forming front which we will study in greater detail in Ch. 8.

Figure 6.9 shows the mixing length as a function of Ra_s for fronts propagating through convection rolls. The mixing length varies in time due to the interactions with the convection rolls. In Fig. 6.9 we show the time average value $\bar{L}_s$ using the filled symbols where the error bars indicate the standard deviation of the oscillations about the mean value.

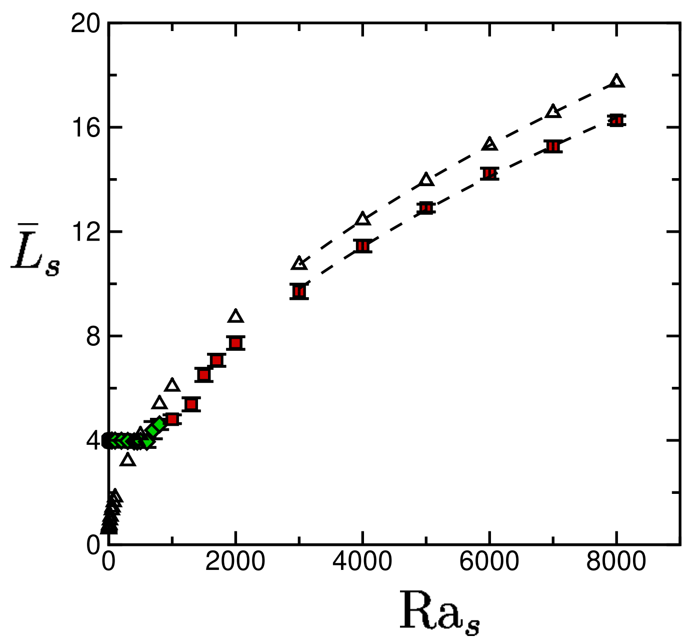

Figure 6.9: The mixing length $\bar{L}_s$ for a front propagating through a convective flow field ($\mathrm{Ra} = 3000$), with solutal feedback, as a function of Ra_s using our convention of circles (blue), diamonds (green), and squares (red) for low, intermediate, and large value of Ra_s, respectively. The mixing length for $\mathrm{Ra} = 0$ are included as the triangles for reference. The dashed lines indicate a scaling of $\bar{L}_s \propto \mathrm{Ra}_s^{1/2}$.

For $\mathrm{Ra}_s = 0$ the value of the mixing length is $\bar{L}_s = 4.0 > L_0$ which represents the mixing length enhancement due to the convective flow field alone. A mixing length of 4 corresponds to two pairs of convection rolls since the width of a convection roll is approximately unity. From Fig. 6.8(a) it is clear that the reaction zone spans approximately 4 convection rolls. The mixing length remains approximately at this value for all results where $\mathrm{Ra}_s \lesssim 700$ which includes the circles (blue) and some of the diamonds (green) in Fig. 6.9. As the solutal Rayleigh number increases $\mathrm{Ra}_s \gtrsim 700$ the mixing length begins to grow as shown by the remaining diamonds (green) and the squares (red). For large values of Ra_s the data scales as $\bar{L}_s \propto \mathrm{Ra}_s^{1/2}$ as indicated by the dashed line. The mixing length results, in the absence of thermal convection ($\mathrm{Ra} = 0$), are included as the triangles for comparison. The presence of the thermal convection causes $\bar{L}_s$ to be larger for very small Ra_s and then smaller for larger values of Ra_s.

The variation of the characteristic fluid velocity $U(t)$ is shown in Fig. 6.10. As defined before in Sec. 3.2 we define the characteristic fluid velocity $U(t)$ as the maximum fluid velocity that occurs in the spatial region around the front that we have previously identified as the mixing length L_s. In Fig. 6.10(a)-(b) we present the results using the normalized characteristic fluid velocity $U_n(t)$ where $U_n(t) = (U(t) - U_c)/U_c$ where U_c is the characteristic fluid velocity of the convective flow field in the absence of solutal feedback. In Fig. 6.10(c) we plot the variation of the time average $\bar{U}_n$ where $\bar{U}_n = (\bar{U} - U_c)/U_c$. When presented this way, a positive (negative) velocity of $U_n(t)$ or $\bar{U}_n$ indicates a characteristic velocity that is larger (smaller) than the background convective flow field.

In Fig. 6.10(a)-(b) we show $U_n(t)$ for several representative examples which demonstrate the oscillatory fluid dynamics that occur due to the solutal feedback of the propagating front. Figure 6.10(c) shows the time average of the characteristic fluid velocity $\bar{U}_n$ over a large range of Ra_s where the error bars are the standard deviations about the mean value of the oscillations.

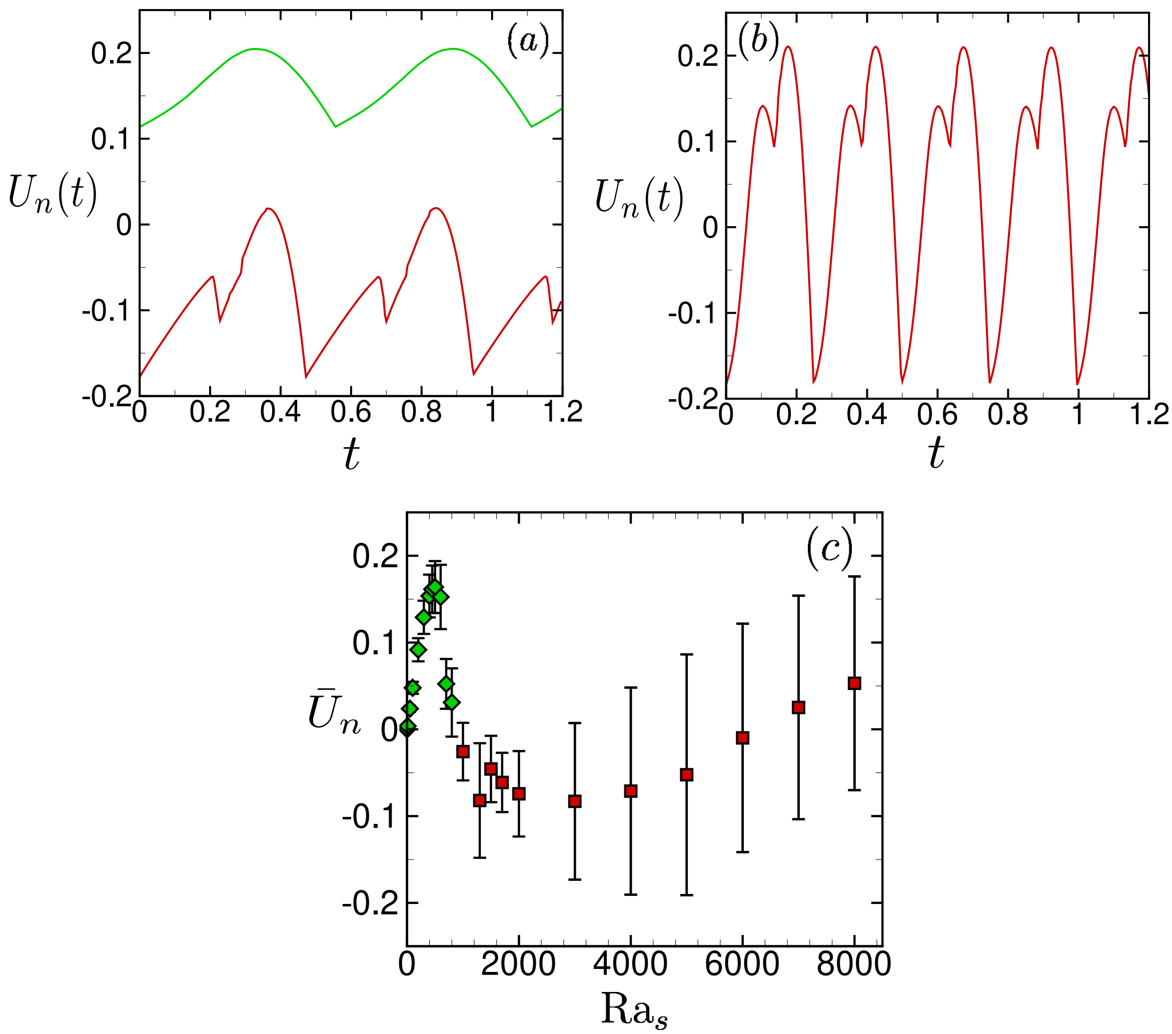

Figure 6.10: The variation of the scaled characteristic fluid velocity for a front propagating through a convective flow field with Ra$=$3000. The characteristic velocity of the background convective flow field in the absence of a front is $U_c=10.81$. (a) The normalized fluid velocity $U_n(t) = (U(t)-U_c)/U_c$ as a function of time for $\mathrm{Ra}_s = 500$ (upper, green) and $\mathrm{Ra}_s = 2000$ (lower, red) and in (b) for $\mathrm{Ra}_s = 8000$. In these plots time has been adjusted such that $t=0$ at the beginning of a period of the oscillatory dynamics for easier comparison. (c) The characteristic fluid velocity $\bar{U}_n = (\bar{U} - U_c)/U_c$ as a function of Ra_s where the error bars represent the standard deviation of $U(t)$ about the mean value. Flow field images for these fronts are shown in Fig. 6.8.

The upper curve (green) of Fig. 6.10(a) illustrates the periodic dynamics of $U_n(t)$ for $\mathrm{Ra}_s =$

500 which corresponds to the case where the peak occurs in Fig. 6.10(c). For this case, $U(t)$ is greater than the characteristic velocity of the background convective flow for all time. This indicates that the solutal feedback is increasing the fluid velocity. The characteristic fluid velocity rises and then falls periodically. The periodic oscillation is due to the counterrotating convection rolls. The leading edge of the propagating front is near the upper wall for $\mathrm{Ra}_s > 0$ as shown in Fig. 6.8. When the leading tip of the front approaches the left side of a counterclockwise convection roll, the directions of the front and the fluid velocity are opposing. This interaction results in a reduction in $U_n(t)$ and the troughs of the green curve occur at these times. When the leading tip of the front approaches the left side of clockwise convection roll, the front and convective velocity are cooperative and this results in an increase in $U_n(t)$ and the peak values of the green curve in Fig. 6.10(a).

The convection rolls have a spatial wavelength of $\lambda \approx 2$ since two rolls of unity width are required for the convective flow field to repeat. Therefore, we can use $U_n(t)$ to provide an estimate of the front velocity as $\bar{v}_f \approx \lambda/t_p$ where t_p is the period of time for $U_n(t)$ to repeat in Fig. 6.10(a). For the upper curve (green) this yields $\bar{v}_f \approx 2/0.56 = 3.57$. This is approximate since the solutal feedback will distort the convection rolls that interact with the leading tip of the front such that λ may change significantly for large values of Ra_s. For comparison, the actual front velocity is shown quantitatively in Fig. 6.11, where $\bar{v}_f = 3.62$ for $\mathrm{Ra}_s = 500$, indicating that the approximate value is very accurate in this regime.

The lower curve (red) of Fig. 6.10(a) shows $U_n(t)$ for $\mathrm{Ra}_s = 2000$ which corresponds to the case where $\bar{U}_n$ is near its most negative value in Fig. 6.10(c). For this case, $U(t)$ is less than the convective fluid velocity except for a brief time near its peak. In this case, the interaction of the solutal feedback with the convection rolls results in a decrease in the fluid velocity on average. The overall periodic rise and fall of $U_n(t)$ is again due to the interaction of the leading tip of the front with the convection rolls. However, in this case there are now two peaks in $U_n(t)$ within each cycle of the periodic dynamics. The first peak and its small neighboring trough, for example near $t \approx 2$ in Fig. 6.10(a), is due to the distortion of the convection rolls by the leading tip of the front through solutal feedback at the location where $U_n(t)$ occurs. It is clear that the lower curve (red) repeats over a shorter duration than the upper curve (green) which suggests that the front velocity is larger for this case. For this case we find $\bar{v}_f \approx 2/0.47 = 4.26$ which is larger as expected and also in very good agreement with the actual value of the front speed $\bar{v}_f = 4.29$.

Figure 6.10(b) illustrates $U_n(t)$ for the large value of $\mathrm{Ra}_s = 8000$. In this case, the periodic dynamics again contain two peaks due to the interaction of the leading tip of the front with the counterrotating convection rolls. The maximum value is positive and the minimum value is negative and the front is clearly now much faster. An estimate of the front velocity gives $\bar{v}_f \approx 2/0.25 = 8.0$. It is interesting to point out that this approximate value of $\bar{v}_f$ has an error of less than 1% when compared with the correct value given in Fig. 6.11(b) of $\bar{v}_f = 7.93$.

The solutally driven flow for $\mathrm{Ra}_s = 8000$ is quite strong, for example a flow field for $\mathrm{Ra}_s = 3000$ is shown in Fig. 6.8(g) which exhibits the same general features. There is a large spatial region where the solutal convection roll has destroyed the underlying convection rolls which includes most of the spatial region occupied by the front yet the leading tip of the front interacts with distorted convection rolls. The velocity $U(t)$ occurs in the region occupied by the leading tip of the front. Since the leading tip of the front interacts with distorted convection rolls this approximation remains quite accurate.

Figure 6.10(c) illustrates the trend that $\bar{U}_n$ initially increases and reaches a peak value near $\mathrm{Ra}_s \approx 500$. For larger values of the solutal Rayleigh number, $\bar{U}_n$ decreases and reaches a minimum near $\mathrm{Ra}_s \approx 3000$. Further increases of Ra_s yields increasing values of $\bar{U}_n$ for the range of our calculations.

The variation of the front velocity is shown in Fig. 6.11. Figure 6.11(a) shows $v_f(t)$ for several illustrative examples. The black curve is the front velocity for $\mathrm{Ra}_s = 0$ and is the front velocity in the absence of solutal feedback. Small oscillations are evident due to the front getting convected by the fluid motion. The green curve shows $v_f(t)$ for $\mathrm{Ra}_s = 500$ which is very similar to $v_f(t)$ in the absence of solutal feedback. It is interesting to point out that the characteristic fluid velocity has a peak value at this value of Ra_s as shown in Fig. 6.10(c). The lower red curve shows $v_f(t)$ for $\mathrm{Ra}_s = 2000$ which yields clear temporal oscillations. Lastly, the upper red curve shows results for $\mathrm{Ra}_s = 8000$.

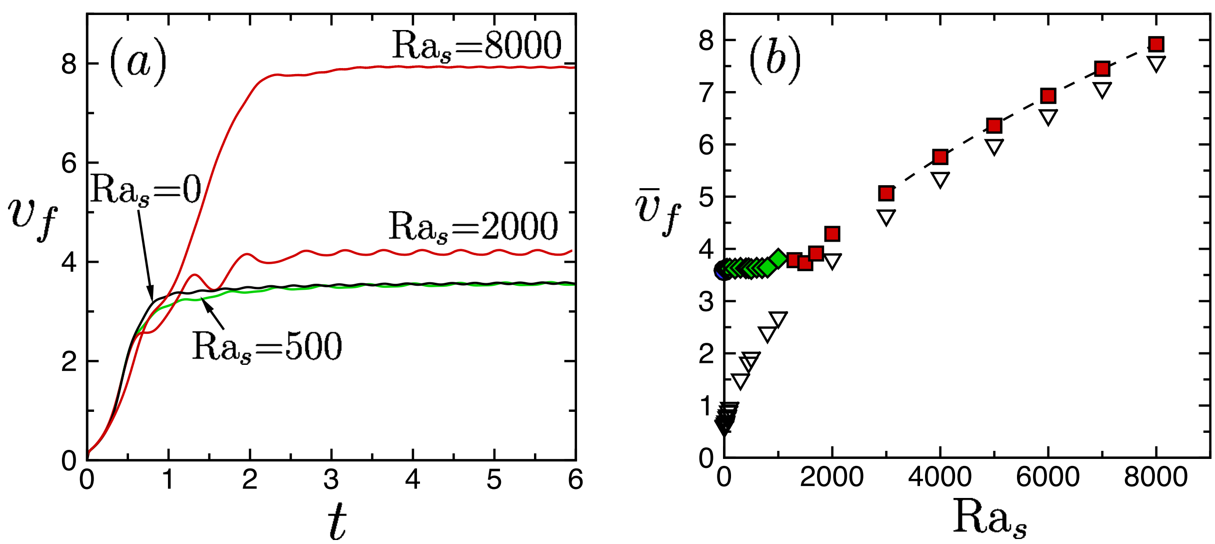

Figure 6.11: The variation of the front velocity for fronts propagating with solutal feedback through convection rolls with $\mathrm{Ra} = 3000$. (a) The front velocity $v_f(t)$ as a function of time t for different values of Ra_s where $\mathrm{Ra}_s = 0$ (black), $\mathrm{Ra}_s = 500$ (green), $\mathrm{Ra}_s = 2000$ (lower red) and $\mathrm{Ra}_s = 8000$ (upper red). (b) The variation of asymptotic front velocity $\bar{v}_f$ with Ra_s. The front velocity when $\mathrm{Ra}_s = 0$ is $\bar{v}_f = 3.59$. The dashed line represents a scaling of $\mathrm{Ra}_s^{1/2}$. Flow field images corresponding to these results are shown in Fig. 6.8. The open triangles are the results for the front velocity in absence of convection from Fig. 6.5(c) and are included here for comparison.

Figure 6.11(b) shows the asymptotic front velocity over a large range of Ra_s. The filled symbols are results for fronts traveling through convection rolls. We do not include error bars here since the magnitude of the oscillations of $v_f(t)$ are on the order of the symbol size used in the figure. The open triangles are the results in the absence of thermal convection ($\mathrm{Ra}=0$) and are included here for comparison. It is clear that for small and intermediate values of Ra_s, shown by the green diamonds and the one blue circle at $\mathrm{Ra}_s = 0$, that the front velocity remains constant in this regime.

However, for larger values of Ra_s, Fig. 6.11(b) shows that the front velocity increases and eventually is described by the $\mathrm{Ra}_s^{1/2}$ scaling indicated by the dashed line. It is clear that in comparison with the front velocities in the absence of thermal convection (the open symbols in Fig. 6.11 (b)) that the fronts with thermal convection have an increased velocity for all values of Ra_s. The increase in velocity is approximately constant where $\Delta\bar{v}_f = \bar{v}_f - \bar{v}_f(\mathrm{Ra}=0) \approx 0.5$ for $\mathrm{Ra}_s \gtrsim 2000$.

Overall, we find that propagating fronts with solutal feedback in the presence of counterrotating thermal convection rolls have a decreased mixing length, an increased front velocity, an oscillating characteristic fluid velocity, and increased oscillations in the front velocity. These results are due to the complex interactions between the solutal feedback and the fluid dynamics.

The interactions between the front and the fluid dynamics can be further visualized using space-time plots of the concentration field. In Fig. 6.12 we show space-time plots of the concentration field at the horizontal midplane $c(x, z=1/2, t)$ where x is the horizontal axis and t is the vertical axis with positive time in the downward direction. Red is products, blue is reactants, and the reaction zone is the green/yellow region. The vertical lines in Fig. 6.12(b)-(d) indicate the locations of the centers of the convection rolls in the fluid before the front passes through where solid (dashed) indicates a clockwise (counterclockwise) rotating convection roll. A space-time plot for the case of $\mathrm{Ra}_s = \mathrm{Ra} = 0$ would simply yield a green/yellow region that is a line from the upper left to the lower right where the inverse

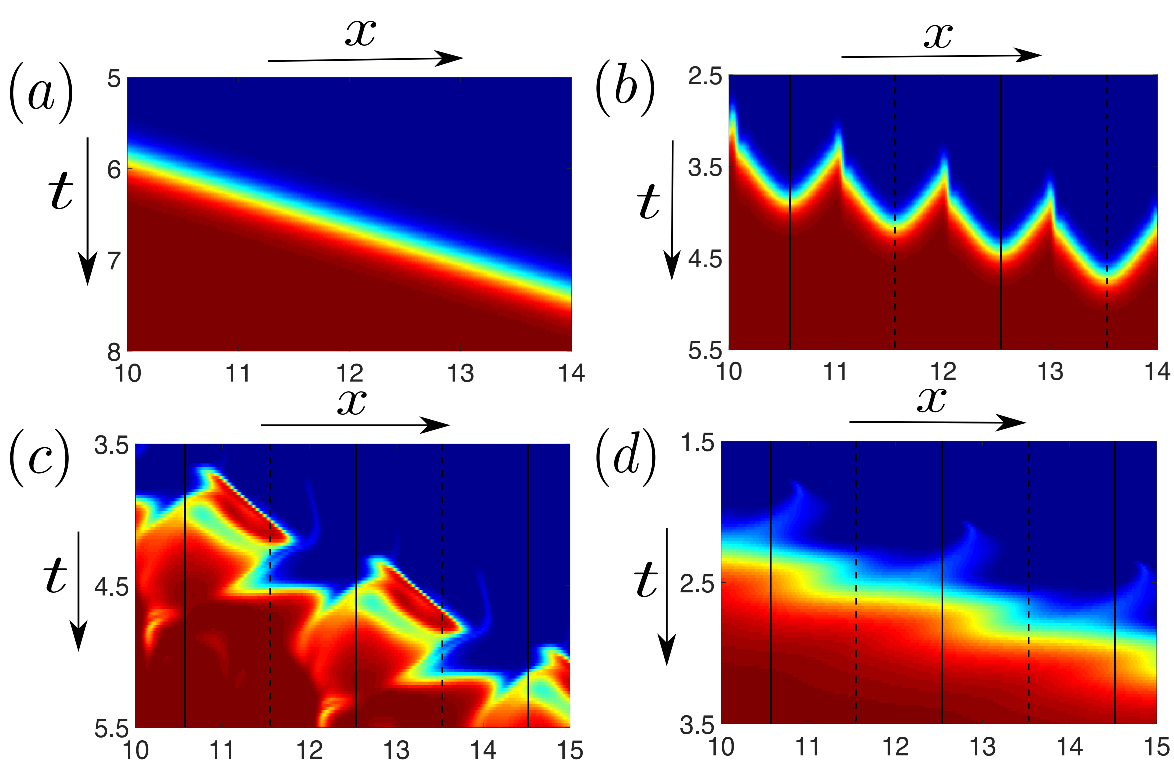

Figure 6.12: The spatiotemporal features of propagating fronts with solutal feedback in the presence of convection. Space-time plots are shown of the concentration at the horizontal midplane $c(x, z = 1/2, t)$ where x is the horizontal axis and t is the vertical axis. The spatial location of the thermal convection rolls are indicated by the vertical lines with the centers of convection rolls with a clockwise (counterclockwise) rotation are shown with solid (dashed) lines. Only a small portion of space and time are shown in order to visualize the complex features. Color shows concentration (c) where red is products ($c = 1$) and blue is reactants ($c = 0$). (a) Solutal feedback without thermal convection ($\text{Ra}_s = 1000$, $\text{Ra} = 0$). (b) No solutal feedback with thermal convection ($\text{Ra}_s = 0$, $\text{Ra} = 3000$). Solutal feedback and thermal convection (c) $\text{Ra}_s = 1000$, $\text{Ra} = 3000$; and (d) $\text{Ra}_s = 6000$, $\text{Ra} = 3000$.

slope of the line is the asymptotic front velocity $\bar{v}_f$. A similar result is obtained for $\text{Ra}_s > 0$ with $\text{Ra} = 0$ as shown in Fig. 6.12(a) for the specific case of $\text{Ra}_s = 1000$ and $\text{Ra} = 0$.

The case with thermal convection, but without solutal feedback, is shown in Fig. 6.12(b). The space-time plot yields a periodic structure with triangular features. The troughs are located at the center of the convection rolls because the front spirals inward toward the roll centers which requires extra time. The peaks of the triangular structures occur at locations between convection rolls where the fluid velocity is either a maximum in the upward or downward directions. For example, in Fig. 6.12(b) a maximum downflow occurs at $x = 11$ and a maximum upflow occurs at $x = 12$. In the absence of solutal feedback, the upflow and downflow regions yield symmetric triangular features in the space-time plot.

A horizontal slice through Fig. 6.12(b) at any time t would yield the spatial variation of the midplane concentration at that time. For example, one horizontal slice of Fig. 6.12(b) corresponds to a midplane slice through the image shown in Fig. 6.8(a) where it is clear that the convection roll edges are the first to complete the reaction whereas the centers of the convection rolls are the last. A vertical slice through Fig. 6.12(b) at any position x would yield $c(t)$ at that location. It is clear that any vertical slice of Fig. 6.12(b) would yield a monotonically increasing dependence for $c(t)$ with increasing time as the reaction goes from reactants to products at any particular location x.

This picture changes significantly in the presence of solutal feedback. Figure 6.12(c) shows the space-time plot for a front with both solutal feedback ($\mathrm{Ra}_s = 1000$) and thermal convection ($\mathrm{Ra} = 3000$). There are now significant changes to the spatial and temporal variations of the concentration field. This front is also shown in Fig. 6.8(e). An interesting feature is the emergence of temporal oscillations in the concentration field at particular x locations. For example, a vertical slice at $x = 11.5$ which corresponds with the vertical dashed line would yield a concentration that oscillates in time as it goes from reactants to products. There are also spatially complicated regions in the product region where the reaction is slow to reach completion, for example near $x \approx 12$ at time $t \approx 5.5$.

Figure 6.12(d) shows the space-time plot for a case where Ra_s is large and the convective flow is dominated by the solutally driven flow. In this case, the space and time features are much smoother. However, small temporal oscillations of $c(t)$ are still present for some choices of x such as $x \approx 13$. Although the front annihilates the convection rolls as it passes through, the leading edge of the front does interact directly with the convection rolls which leads to the wisp-like structures in light blue that indicate the locations where the reaction first takes place. For example, a wisp is located near $x \approx 11$ and $t \approx 2$.

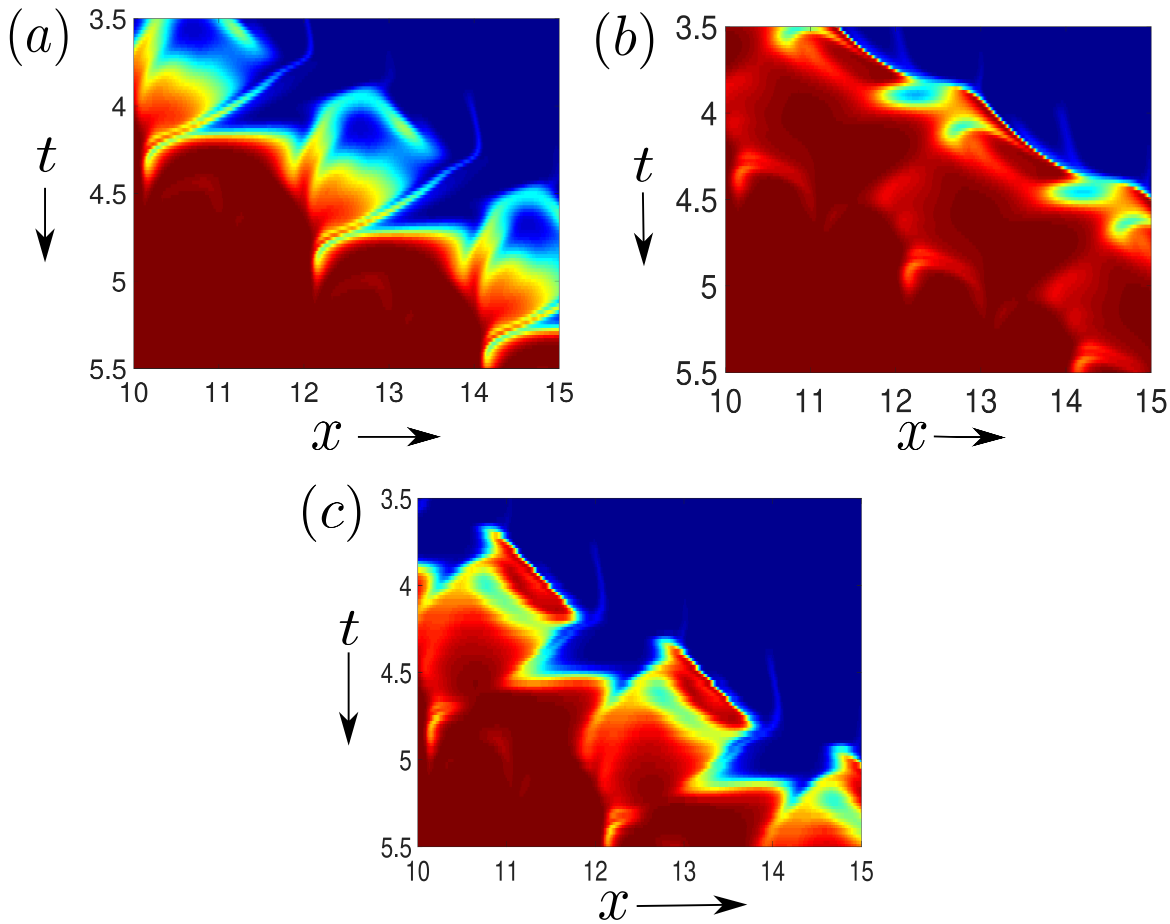

Figure 6.13: Zoomed-in view of space-time plots at different z-slices for a front propagating with $\mathrm{Ra} = 3000$ and $\mathrm{Ra}_s = 1000$. Color shows concentration (c) where red is products ($c = 1$) and blue is reactants ($c = 0$). (a) Zoomed-in view of the space-time plot at $z = 0.3$ (b) at $z = 0.7$ (c) at $z = 1/2$ which is same as Fig. 6.12(c)

Figure 6.13 shows the space-time plot for $\mathrm{Ra} = 3000$ and $\mathrm{Ra}_s = 1000$ at different z slices. Figure 6.13 (a) shows the space-time plot at $z = 0.3$, where the dynamics is extremely rich. At this slice, the heavier reactants invade into the products to create isolated patches of reactants. Figure 6.13 (b) shows the space-time plot at $z = 0.7$, where the dynamics is comparatively smoother. This slice goes through the leading edge seen in Fig. 6.8 (e) It is clear that the slice at $z = 1/2$ is insightful representations of the bulk as well as the front-tip dynamics.

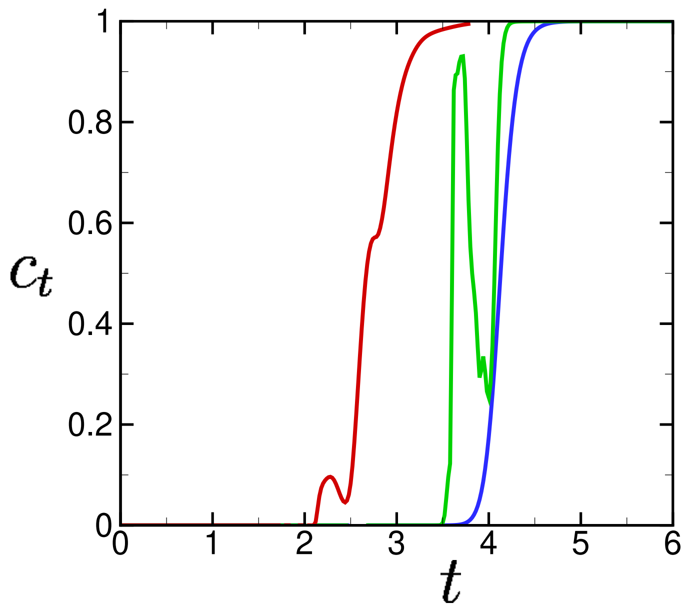

Figure 6.14: Temporal oscillations of the concentration of products, $c_t(t) = c(x = x_s, z = 1/2, t)$, for fronts propagating with solutal feedback in convective flow fields. x_s is the slice through the x-locations in Fig. 6.12. The red solid line is for $\mathrm{Ra}_s = 6000$ where the slice is taken at $x_s = 13$. The green solid line is for $\mathrm{Ra}_s = 1000$ where the slice is taken at $x_s = 11.5$. The blue solid line is for $\mathrm{Ra}_s = 0$ where the slice is taken at $x_s = 11.5$.

Figure 6.14 shows the temporal oscillations in the concentration. Here concentration is plotted as $c_t(t) = c(x = x_s, z = 1/2, t)$ where x_s is the slice through the x-locations in Fig. 6.12. As discussed in Fig. 6.12, a slice through $x_s = 11.5$ through Fig. 6.12 (c), where $\mathrm{Ra}_s = 1000$, shows strong oscillations as seen by the green solid lines with diamond symbols. Similarly, a slice through $x_s = 13$ through Fig. 6.12 (d), where $\mathrm{Ra}_s = 6000$, shows weak oscillations. Any slice through Fig. 6.12 (b) will produce a monotonic increase of c_t as evident from the blue solid lines with circular symbols. For reference we show a slice of $x_s = 11.5$. Figure 6.14 also shows that increasing solutal Rayleigh number helps to complete the reaction

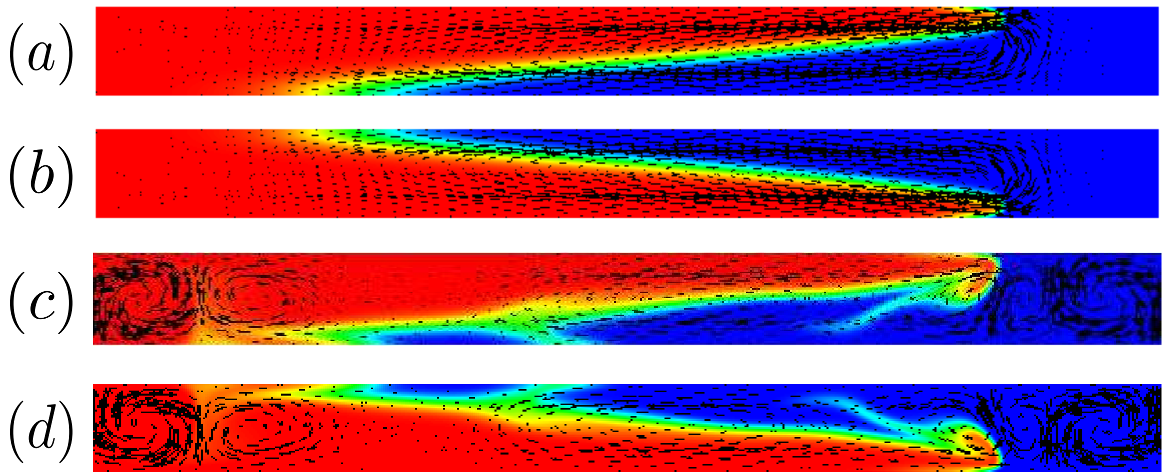

Figure 6.15: Symmetry of propagating fronts for $\mathrm{Ra}_s = 2000$ and $\mathrm{Ra}_s = -2000$ in initially quiescent flow fields and flow fields undergoing convection. A zoomed-in spatial view is shown for better visualization. (a) Propagating fronts for $\mathrm{Ra}_s = 2000$ and $\mathrm{Ra} = 0$. (b) Propagating fronts for $\mathrm{Ra}_s = -2000$ and $\mathrm{Ra} = 0$. (c) Propagating fronts for $\mathrm{Ra}_s = 2000$ and $\mathrm{Ra} = 3000$. (d) Propagating fronts for $\mathrm{Ra}_s = -2000$ and $\mathrm{Ra} = 3000$. The time has been adjusted such that the fronts are aligned horizontally in (c) and (d) as explained in the text. Color shows concentration (c) where red is products ($c = 1$) and blue is reactants ($c = 0$). The flow field vectors are visualized by arrows.

faster. Overall, our results indicate that fronts with solutal feedback in convective flow fields induce chemical oscillations.

Figure 6.15 shows the symmetry of propagating fronts for $\mathrm{Ra}_s > 0$ and $\mathrm{Ra}_s < 0$. Figure 6.15 (a) and (b) shows the symmetry for propagating fronts with solutal feedback in an initially quiescent fluid. The case for $\mathrm{Ra}_s < 0$ forms an anticlockwise roll that propagates with the front. Figure 6.15 shows the symmetry for propagating fronts with solutal feedback in convective flow fields for $\mathrm{Ra}_s > 0$ and $\mathrm{Ra}_s < 0$. Here we have to adjust the time for $\mathrm{Ra}_s < 0$ to align the propagating fronts. The adjustment is required because the first convection roll that the fronts encounter is a clockwise convection roll at the hot left sidewall. Fronts for $\mathrm{Ra}_s > 0$ form a clockwise roll and thus get a boost at the initiation. The scenario is opposite for fronts propagating with $\mathrm{Ra}_s < 0$ and an anticlockwise propagating roll because

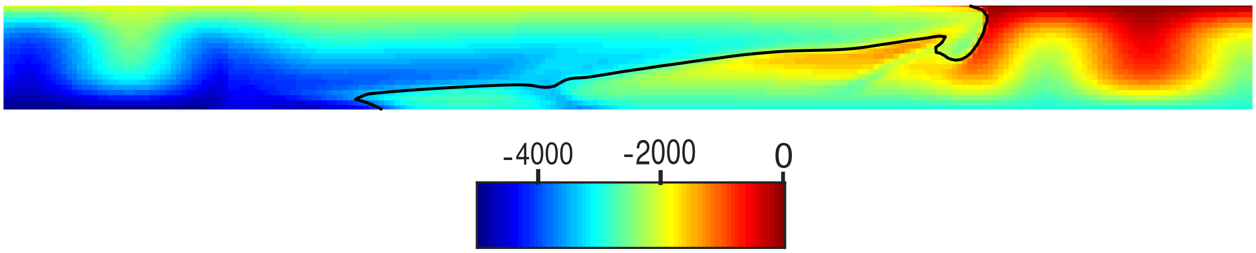

Figure 6.16: Color contour of the nondimensional density $\rho(c,T)$ for a front propagating with solutal feedback at Ra = 3000 and $\mathrm{Ra}_s = 2000$. The nondimensional density is given by Eq. 2.19 and is negative. The level set of $c = 1/2$ is shown by the black solid line indicating the location of the front.

they encounter a roll moving in the opposite direction and the fronts are inhibited at the beginning. The front and fluid velocity magnitudes do not change if the sign of Ra_s is reversed.

Figure 6.16 shows the nondimensional density $\rho(c,T)$ given by Eq. 2.19. The level set of $c = 1/2$ is shown by the black solid line. The nondimensional density is negative. Ahead of the front, the fluid consists of heavier reactants. The fluid is convectively unstable and the density is $\rho(c,T) = -\mathrm{Ra}T$. The hot and lighter fluid goes up and is shown in red color. The heavier fluid goes down and is shown by green color. The region behind the front or to the left side of the figure consists of lighter products after the reaction. The lighter products are still convectively unstable as shown by the lighter fluid in green and yellow going up and the heavier descending fluid in blue. The propagating front invades the spatial region consisting of heavier reactants and leaves a trail of lighter products behind which then form rolls again because of the convective instability.

Chapter 7

Front propagation with thermal feedback from the reaction

In this chapter we explore reacting fronts where the products and reactants are of different density and the reaction is exothermic. To analyze this scenario, we make the following changes to the governing equation given by Eqs. 2.14-2.16. We use $\eta > 0$, $\mathrm{Ra} > 0$ and $\mathrm{Ra}_s \geq 0$ or $\mathrm{Ra}_s \leq 0$. There are two possible scenarios that can be realized for $\eta \geq 0$ [61].

1. We can have a reaction where the products are lighter than the reactants and the reaction releases heat or is exothermic. In this case, both heat release η and solutal coupling Ra_s are positive and reduce the net density of the fluid as given by Eq. 2.19. This case is referred to as *cooperative* because both the solutal and thermal coupling have a positive contribution towards decreasing the density of the fluid.

2. We may have a scenario where products are heavier than the reactants in an exothermic reaction. In this case the solutal feedback increases the density of the fluid and the thermal feedback decreases it. Here we have $\mathrm{Ra}_s < 0$ and $\eta > 0$. This case is referred to as *antagonistic*.

Endothermic autocatalytic reactions are not known to exist which is why we consider $\eta \geq 0$ only for this study. However our numerical approach is quite flexible and we can study the scenario of $\eta \leq 0$ by simply changing the sign of η in Eq. 2.14.

7.1 Fronts with thermal feedback from the reaction

We first study fronts with thermal feedback when $\mathrm{Ra}_s = 0$, that is when reactants and products are of the same density but the reaction is exothermic. We study these fronts with thermal feedback propagating through an initially quiescent flow field with $\mathrm{Ra} = 1000$, which is below the thermal Rayleigh number for convective instability, $\mathrm{Ra}_c = 1708$. Thermal feedback from the reaction causes a local hotspot at the front. This hotspot causes the fluid to locally rise and then descend forming a pair of counterrotating convection rolls, which propagate with the front.

Figure 7.1 shows the color contours of the concentration field for $\eta \geq 0$ and $\mathrm{Ra}_s = 0$ at $\mathrm{Ra} = 1000$. The Lewis number is $\mathrm{Le} = 0.01$. All of the snapshots are at $t = 6$ in a zoomed-in spatial region. This shows that larger values of η increases the front velocity. The aspect ratio for the full domain is $\Gamma = 30$ which is shown in Fig. 6.1. At small values of η, the double roll is almost symmetric, in the sense that the two rolls are nearly of the same size as seen in Fig. 7.1 (a) and (b) which are at $\eta = 1$ and $\eta = 5$ respectively. At larger values of η, this symmetry is broken. The front in this scenario gets tilted and stretched to the right hand side. The fluid roll on the right hand side associated with the front gets stretched in this scenario as can be seen in Fig. 7.1 (c)-(e) which are at $\eta = 7$, 10 and 20 respectively.

At even larger values of η, the flow field gets further distorted and we have increased spatiotemporal distortion of the concentration field as shown in Fig. 7.2. The front is now extended in both the directions and there exists secondary stretched fluid rolls along with the primary couplet of rolls in both the directions. Figure 7.2 shows this scenario for $\eta = 50$ and $\eta = 100$ in Fig. 7.2 (a) and (b) respectively. For large values of η, the temperature of the local hotspot is slightly larger than the bottom wall at $T = 1$. For $\eta = 50$ the maximum temperature generated is $T_{\max} = 1.26$ and for $\eta = 100$ the maximum temperature is

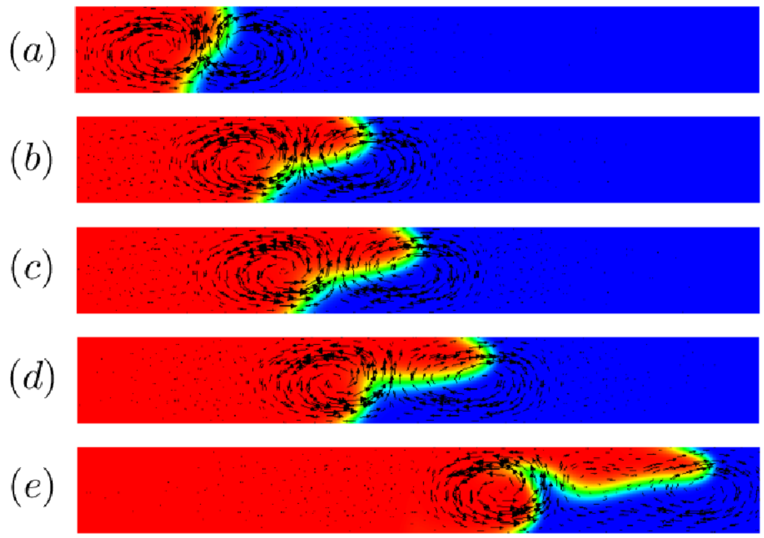

Figure 7.1: Color contours of concentration with background fluid velocity field shown by arrows for fronts with thermal feedback from the reaction. Color contours of concentration with background fluid velocity field shown by arrows for different values of η when $\mathrm{Ra}_s = 0$, $\mathrm{Ra} = 1000$. (a) $\eta = 1$ (b) $\eta = 5$ (c) $\eta = 7$ (d) $\eta = 10$ (e) $\eta = 20$. All the contours are at time, t = 6. Color shows concentration (c) where red is products ($c{=}1$) and blue is reactants ($c{=}0$). The flow field vectors are visualized by arrows. Shown is a zoomed-in view covering the spatial extent $2.5 \leq x \leq 10$. The maximum temperature for each case is $T = 1$.

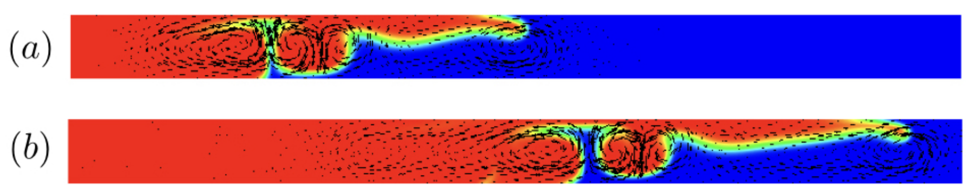

Figure 7.2: Snapshots of concentration fields for larger magnitudes of thermal feedback from the reaction. Color contours of concentration with background fluid velocity field shown by arrows for different values of η when $\mathrm{Ra}_s = 0$, $\mathrm{Ra} = 1000$. (a) $\eta = 50$ (b) $\eta = 100$. All the contours are at time, t = 6. Color shows concentration (c) where red is products ($c = 1$) and blue is reactants ($c = 0$). The flow field vectors are visualized by arrows. Shown is a zoomed-in view for $9 \leq x \leq 22$. The maximum temperature for (a) is $T_{\max} = 1.26$ and for (b) is $T_{\max} = 1.67$, which are hotter than the temperature of the bottom wall.

$T_{\max} = 1.67$.

We plot the variation of the characteristic fluid velocity U and the asymptotic front velocity

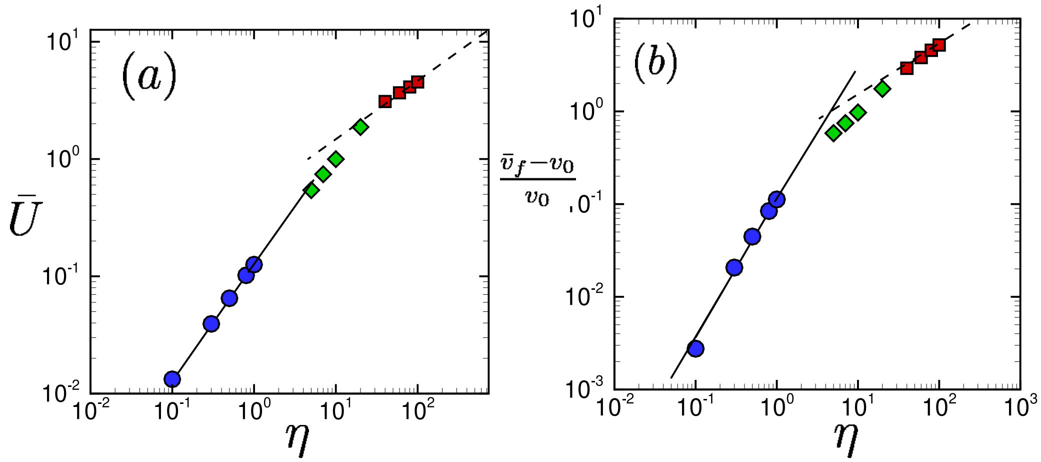

Figure 7.3: The variation of the fluid and the front velocity as a function of the heat release parameter. (a) Variation of characteristic fluid velocity $\bar{U}$ with η for $\mathrm{Ra}_s = 0$, $\mathrm{Ra} = 1000$. The blue circular symbols represent $0 \leq \eta \leq 1$ and the red square symbols represent $\eta > 20$. The intermediate regime is shown by greed diamond symbols. The solid line is a curve-fit through the blue symbols of the form $\bar{U} = 0.127\eta$. The dashed line is a curve-fit through the red squares of the form $\bar{U} = 0.465\eta^{1/2}$. (b) The variation of the normalized asymptotic front velocity as a function of η. The data is grouped similarly as Fig. (a). The solid line is a curve-fit through the blue circles of the form $(\bar{v}_f - v_0)/v_0 = 0.151\eta^{3/2}$. The dashed line is a curve fit through the red square symbols of the form $(\bar{v}_f - v_0)/v_0 = 0.503\eta^{1/2}$.

$\bar{v}_f$ with the heat release parameter η in Fig. 7.3. The characteristic fluid velocity is oscillatory in time for $\eta \geq 0.5$. The oscillations are of the order $\mathcal{O}(10^{-1})$ and increase with larger values of η. We use the mean of the characteristic fluid velocity $\bar{U}$ to quantify the flow. We then plot the variation of $\bar{U}$ with η in Fig. 7.3 (a). We again see a transition in scaling where $\bar{U}$ scales as $\bar{U} = 0.127\eta$ for $0 \leq \eta \leq 1$ and as $\bar{U} = 0.465\eta^{1/2}$ for $\eta > 20$. The linear regime is shown by blue circles and the square-root regime is shown by red squares. The intermediate transitional regime is shown by green diamonds.

Figure 7.3 (b) shows the variation of the asymptotic front velocity $\bar{v}_f$ with η. The asymptotic front velocity in this case is normalized with the no-flow front velocity v_0. We observe a transition in the scaling of $\bar{v}_f$ as a function of η for increasing values of η. The black solid line through the blue circles is a curve-fit of the form $(\bar{v}_f - v_0)/v_0 = 0.151\eta^{3/2}$. The dashed line is a curve fit of the form $(\bar{v}_f - v_0)/v_0 = 0.503\eta^{1/2}$ through larger values of η.

We presently do not have a theoretical explanation for these scaling behaviors. However, a natural direction forward would be to use the perturbation expansion for small values of η and solve the subsequent orders of perturbation to understand the scaling behaviors.

7.2 Fronts with cooperative and antagonistic feedback in an initially quiescent flow field

In this section we explore cooperative and antagonistic feedback through an intially quiescent fluid. We use $\eta = 10$ and $\mathrm{Ra}_s = \pm 60$. Figure 7.4 shows the representative color contours of the concentration field at a time $t = 7.98$. Figure 7.4 (a) shows a front with cooperative feedback where $\eta = 10$ and $\mathrm{Ra}_s = +60$. The combined effect of solutal and thermal feedback has made the products lighter than the reactants and the front gets elongated and tilted as a result. The double roll is still visible with one roll coinciding with the leading edge of the front. The front in this case maintains a steady profile as it propagates. The front propagating with antagonistic feedback at $\eta = 10$ and $\mathrm{Ra}_s = -60$ has an oscillatory nature because of the dynamics of the snout like leading edge of the front in Fig. 7.4 (b).

The oscillatory behavior of the front is further illustrated in the space-time plots shown in Fig. 7.5. The horizontal black dotted lines through the space-time plots are at time $t = 7.98$ for which is used in Fig. 7.4. Overall, we do not find oscillations for the cooperative case as shown by the smooth transition from products to reactants in Fig. 7.5 (a). The case of only $\eta = 10$ and $\mathrm{Ra}_s = 0$ is shown in Fig. 7.1 (d).

Figure 7.5 (b) shows a non-smooth transition from products to reactants where we find repeating rounded features. The emergence of spatiotemporal oscillations in the antagonistic case is due to the competition between the solutal and thermal feedback of the reaction.

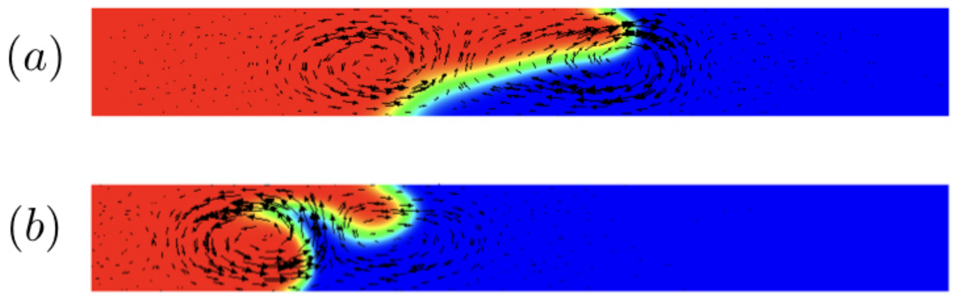

Figure 7.4: Snapshots in time for the cooperative and antagonistic concentration field at $\mathrm{Ra} = 1000$, $\mathrm{Ra}_s = \pm 60$ and $\eta = 10$. Color contours of cooperative and antagonistic concentration field with background fluid velocity field shown by arrows. Color shows concentration (c) where red is products $(c = 1)$ and blue is reactants $(c = 0)$. The flow field vectors are visualized by arrows. (a) Cooperative feedback, $\mathrm{Ra} = 1000$, $\mathrm{Ra}_s = 60$, $\eta = 10$. (b) Antagonistic feedback, $\mathrm{Ra} = 1000$, $\mathrm{Ra}_s = -60$, $\eta = 10$. The images are at time $t = 7.98$. Shown is a zoomed-in spatial view where $6 \le x \le 13$.

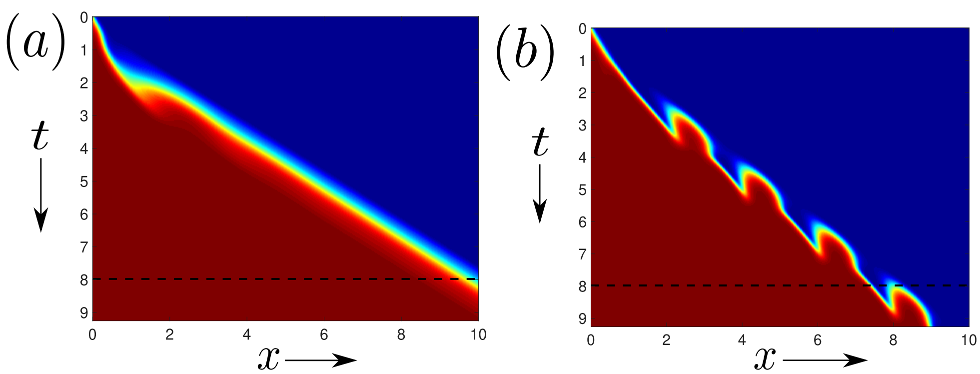

Figure 7.5: Space-time plots for the midplane slice of the concentration field shown in Fig. 7.4 for the cooperative and antagonistic cases at $\eta = 10$ and $\mathrm{Ra}_s = \pm 60$. Color shows concentration (c) where red is products $(c=1)$ and blue is reactants $(c=0)$. The horizontal dashed lines are at time $t = 7.98$ which is used in Fig. 7.4. (a) Cooperative feedback, $\mathrm{Ra} = 1000$, $\mathrm{Ra}_s = 60$ and $\eta = 10$. (b) Antagonistic feedback, $\mathrm{Ra} = 1000$, $\mathrm{Ra}_s = -60$ and $\eta = 10$.

The solutal feedback for this case converts the reactants into heavy products. The thermal feedback from the reaction tries to convect the products and the reactants to the top wall. The heavier products form a leading edge, however since the products are heavy the leading edge is unstable and falls down. This mechanism of turning over of the heavier leading edge repeats and yields the oscillatory space-time plot shown in Fig. 7.5 (b).

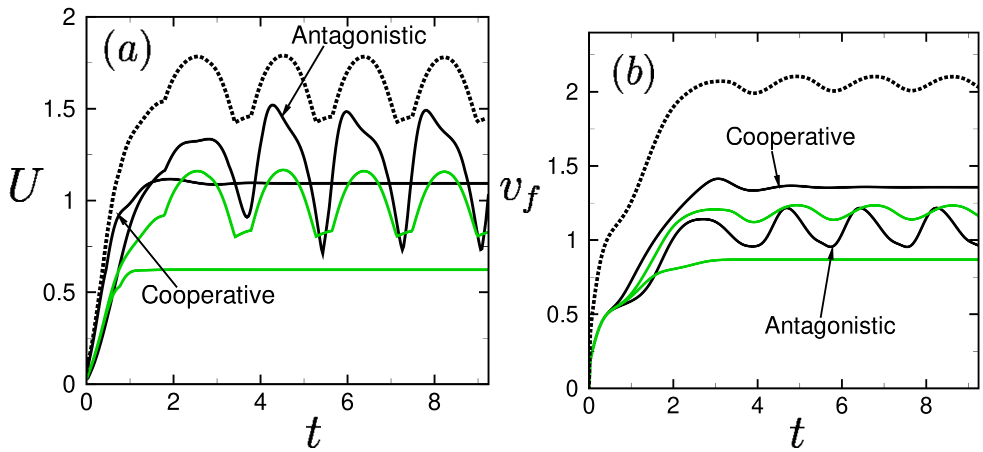

Figure 7.6: The time variation of the fluid and the front velocity for cooperative and antagonistic feedback at Ra = 1000. We examine cooperative feedback at $\mathrm{Ra}_s = +60, \eta = 10$ and antagonistic feedback at $\mathrm{Ra}_s = -60, \eta = 10$. The black solid lines are labelled for cooperative and antagonistic feedback. The lower green solid lines are for results with only solutal feedback ($\mathrm{Ra}_s = 60$ and $\eta = 0$). The upper green lines are for results with only thermal feedback from the reaction ($\mathrm{Ra}_s = 0$ and $\eta = 10$). The black dotted lines are obtained by adding the cases of only solutal feedback and only thermal feedback (the summation of the two green lines). (a) The time variation of the characteristic fluid velocity. (b) The time variation of the front velocity.

Figure 7.6 (a) and (b) show the time variation of the characteristic fluid velocity and the front velocity for fronts with cooperative and antagonistic feedback as shown in Fig. 7.4. The results from the cooperative and antagonistic cases are shown by the black solid lines, where the oscillating lines denotes results from the antagonistic case. The relatively straight black lines (at larger times) represent results for the cooperative case where we do not find any oscillations for parameters $\mathrm{Ra}_s = 60$ and $\eta = 10$. The case of only thermal feedback from the reaction ($\eta = 10$ and $\mathrm{Ra}_s = 0$) is shown by the upper green oscillating line in both plots. The green color is chosen because $\eta = 10$ lies in the intermediate regime in Fig. 7.3. The case of only solutal feedback ($\mathrm{Ra}_s = 60$ and $\eta = 0$) is shown by the lower green lines. Here again, the green line is chosen because $\mathrm{Ra}_s = 60$ lies in the intermediate regime shown in Fig. 6.5. Lastly, the black dotted lines are results from simply adding the cases of only solutal feedback and only thermal feedback and is plotted as a reference.

Figure 7.6 (a) plots the variation of the characteristic fluid velocity with time for fronts cooperative and antagonistic feedback at $\mathrm{Ra}_s = \pm 60$ and $\eta = 10$. Fronts with antagonistic feedback create the largest magnitude of fluid flow on average for these parameters. The characteristic fluid velocity is oscillatory with a period that is related to the turning over of the leading edge of the heavier products as described above. The relatively steady solid black line represents the characteristic fluid velocity for fronts with cooperative feedback. The front shape for the cooperative feedback is steady and there are no oscillations present. The oscillating green line represents $U(t)$ for the case of only thermal feedback at $\eta = 10$ which is shown in Fig. 7.1 (d). The relatively steady solid green line is the case for $\mathrm{Ra}_s = 60$ or only solutal feedback. As explained before in Ch. 6, the scenario where $\mathrm{Ra}_s = -60$ yields the same value of the front velocity in the absence of thermal feedback. The characteristic fluid velocity for both the cases of only solutal or only thermal feedback are less than the cooperative and antagonistic scenarios. This suggests that any change in the density between the products and the reactants combined with the exothermic heat release *increases* the fluid velocity. Lastly, for reference, the black dotted line is obtained by adding the data from the individual thermal and solutal feedback. The black dotted line has an average magnitude of U which is larger than all the cases. It is interesting to note that the velocities for combined thermal and solutal feedback (shown by black solid lines) are less than the linear sum of the individual feedback mechanisms. This is expected, since the problem is nonlinear and the complicated interactions of thermal and solutal feedback cannot be represented by a linear sum.

Figure 7.6 (b) shows the variation of the front velocity with time for fronts with cooperative and antagonistic feedback at $\mathrm{Ra}_s = \pm 60$ and $\eta = 10$. The color convention used is the same as in Fig. 7.6 (a). For this case the front velocity in the scenario of cooperative feedback is the largest for these parameters. Fronts with antagonistic feedback are slower than the cooperative feedback as well as the case of only thermal feedback from the reaction. This suggests that adding a negative contribution to the density jump across the front interface reduces the front velocity. The additive scenario of the individual feedback mechanisms is also shown by the black dotted line. Since the problem is nonlinear, the front velocities obtained for the combined thermal and solutal feedback is less than the linear sum of the two individual effects.

The parameter space for studying feedback is vast as we can vary three parameters η, Ra and Ra_s independently. For example, increasing the values of Ra_s and η can result in more complicated and oscillatory dynamics. One such scenario is shown in Fig. 7.7 where $\eta = 50$ and $\mathrm{Ra}_s = \pm 300$. The dynamics are now more complicated as seen by the elongated fluid rolls, double convection rolls and isolated spatial regions between products which consist of reactants. The snapshots are taken at the same time $t = 5.97$ which shows that the mixing length and the front velocity for the cooperative case exceeds the antagonistic case as expected. Figure 7.7 (a) shows a scenario similar to the case where we have high η shown in Fig. 7.2. In this case, there is a counterrotating pair of convection rolls along with two more stretched rolls located ahead and behind the front. The fluid roll ahead of the double roll is stretched to a large extent with the front to form a snout like feature. The shape of the leading edge is steady with time as the front propagates but complicated dynamics is present at the tail of the leading edge where there are in total three convection rolls.

Figure 7.7 (b) shows the scenario for antagonistic feedback. Here we see three convection rolls, a stretched leading edge consisting of heavier products and isolated patches of reactants inside the products. The leading edge that forms for this case consists of heavier products which then descend down and yield complicated oscillatory dynamics. The heavier leading edge traps reactants inside it as it descends down and we get isolated regions of reactants inside the products.

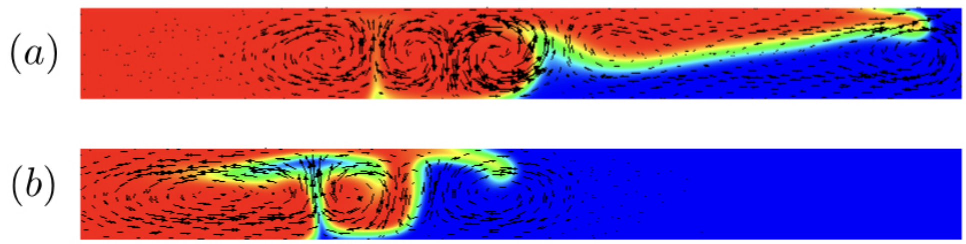

Figure 7.7: Color contours of the concentration field for fronts with cooperative and antagonistic feedback in the absence of background convection. The background fluid velocity field shown by arrows. Parameters are Ra $= 1000$, Ra$_s = \pm 300$ and $\eta = 50$. Color shows concentration (c) where red is products ($c\!=\!1$) and blue is reactants ($c\!=\!0$). The flow field vectors are visualized by arrows. (a) Cooperative feedback, Ra $= 1000$, Ra$_s = 300$, $\eta = 50$. (b) Antagonistic feedback, Ra $= 1000$, Ra$_s = -300$, $\eta = 50$. Red is pure products and blue is pure reactants. The images are at time $t = 5.97$. Shown is a zoomed-in spatial view for $8 \leq x \leq 17$.

In Fig. 7.8 we further probe the complicated dynamics using space-time plots at the midplane for the concentration fields shown in Fig. 7.7. Figure 7.8 (a) shows the space-time plot for the cooperative case. For this scenario we observe spatiotemporal oscillations for the cooperative case as well. Figure 7.8 (b) shows the space-time plot for the antagonistic case and it consists of jagged and sharp features.

Figure 7.9 shows the temporal variation of U and v_f for this case. The black lines are the cases of cooperative and antagonistic feedback as labelled in the figure. It is interesting to note that the cooperative case also shows oscillations for these parameters. The temporal variation of U is plotted in Fig. 7.9(a) and the temporal variation of v_f is plotted in Fig. 7.9(b). For cooperative feedback, the temporal variation of the fluid and front velocities show a single repeating pattern. The antagonistic case, on the other hand, shows two modes of oscillations. This two modal oscillation is related to the competing thermal and solutal feedback. The leading edge for the antagonistic feedback consists of heavier products which tumbles down

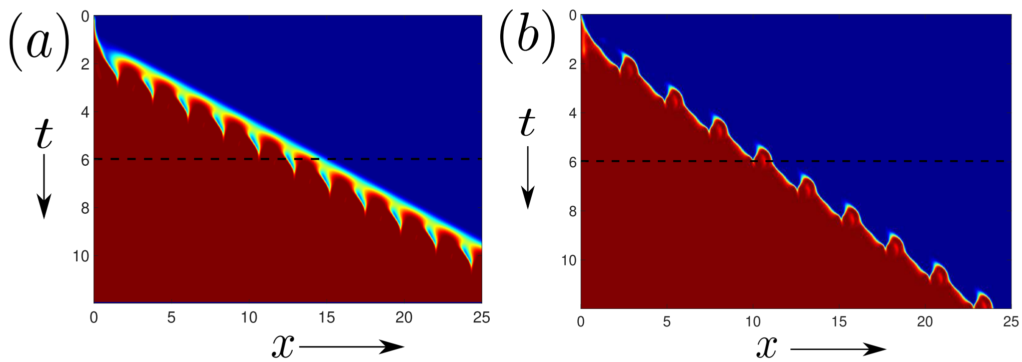

Figure 7.8: Space-time plots for the midplane slice of the concentration field shown in Fig. 7.7 for the cooperative and antagonistic case at $\eta = 50$ and $\mathrm{Ra}_s = \pm 300$. The horizontal dashed lines are at time $t = 7.98$ which is same as Fig. 7.7. Color shows concentration (c) where red is products ($c = 1$) and blue is reactants ($c = 0$). (a) Cooperative feedback, Ra = 1000, $\mathrm{Ra}_s = 300$ and $\eta = 50$. (b) Antagonistic feedback, Ra = 1000, $\mathrm{Ra}_s = -300$ and $\eta = 50$.

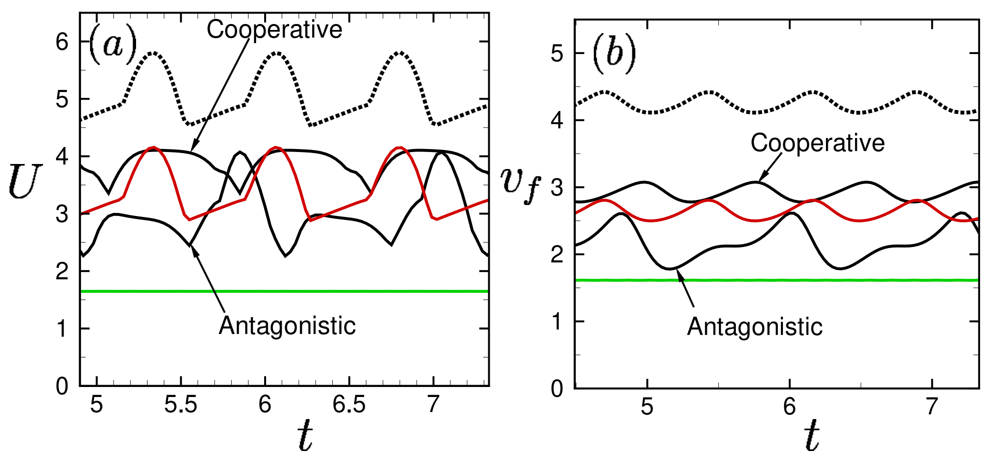

Figure 7.9: The time variation of the fluid and the front velocity for cooperative and antagonistic feedback at Ra = 1000, $\mathrm{Ra}_s = \pm 300$ and $\eta = 50$. The thermal Rayleigh number is fixed at Ra = 1000. We examine a case where we expect cooperative feedback at $\mathrm{Ra}_s = +300, \eta = 50$ and antagonistic feedback at $\mathrm{Ra}_s = -300, \eta = 50$. The black oscillating lines are for cooperative feedback and antagonistic feedback with arrows pointing to the respective cases. The lower green lines are for results from only solutal feedback ($\mathrm{Ra}_s = 300$ and $\eta = 0$). The red oscillating lines are for results from only thermal feedback from the reaction ($\mathrm{Ra}_s = 0$ and $\eta = 50$). The upper black dotted lines are for results which are obtained by adding the cases of only solutal feedback and only thermal feedback or the green and red lines. (a) The time variation of the characteristic fluid velocity. (b) The time variation of the front velocity.

and results in complicated dynamics shown in Fig. 7.7(b). The scenario with only thermal feedback at $\eta = 50$ is shown by the red oscillating line. The color red is chosen because $\eta = 50$ lies in the regime of by large η in Fig. 7.3. Similarly, the case with only solutal feedback at $\mathrm{Ra}_s = 300$ is shown by the green line because this value of Ra_s lies in the transitional regime shown in Fig. 6.5. Lastly, the dotted line represents the scenario where we have added the cases of only thermal feedback (red line) and only solutal feedback (green line). The sum of the two individual effects again does not represent the actual combined scenario and overestimates the value. This is expected because of the nonlinearities in the system. For these parameters, the antagonistic feedback yields a slower front and fluid velocity than the scenario for only thermal feedback.

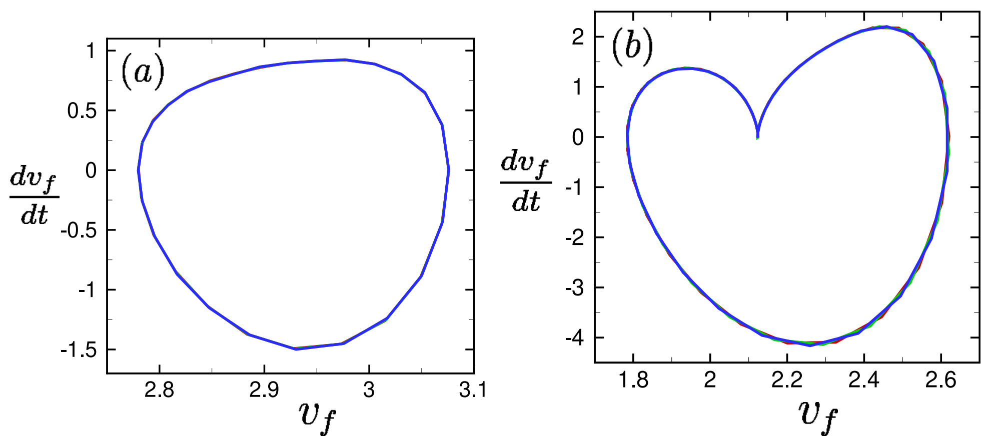

Figure 7.10: Phase portrait of the front velocity for fronts with cooperative and antagonistic feedback at $\eta = 50$ in the absence of background convection at $\mathrm{Ra} = 1000$. The time variation of the front velocities for this case are shown in Fig. 7.9 (b). Three repetitions are shown by red, green and blue lines. (a) Cooperative feedback, $\mathrm{Ra}_s = 300$. (b) Antagonistic feedback, $\mathrm{Ra}_s = -300$.

Figure 7.10 shows the phase portraits for fronts with cooperative and antagonistic feedback at $\mathrm{Ra}_s = \pm 300$ and $\eta = 50$ in the absence of background convection. Phase portraits help in the quantification of periodic dynamics in phase space. The quantity that is used to draw the phase portrait is the front velocity obtained using the bulk burning rate. The temporal variation of front velocity is shown in Fig. 7.9 (b). We plot the time derivative of the front velocity dv_f/dt as a function of the front velocity to obtain the phase portrait.

Figure 7.10 (a) shows the phase portrait for fronts with cooperative feedback at $\mathrm{Ra}_s = 300$ and $\eta = 50$ in the absence of background convection. The single repeating pattern is represented by the oval trajectories on the phase portrait. We have plotted three repeating trajectories by red, blue and green lines. The overlap of the trajectories suggest the presence of periodic dynamics. The time period of oscillation for cooperative feedback at these parameters is approximately $t \approx 0.81$. The periodic dynamics is associated with the counterrotating convection roll.

Figure 7.10 (b) shows the phase portrait for fronts with antagonistic feedback at $\mathrm{Ra}_s = -300$ and $\eta = 50$ in the absence of background convection. The two modal oscillation observed in Fig. 7.9 results in the double lobed oval shape of the trajectories in the phase portrait. The left lobe results from the fast turn-over dynamics of the extended leading edge which consists of heavy products shown in Fig. 7.7. The right lobe results from the slower dynamics due to the counterrotating convection roll. The time period for one entire repetition is approximately $t \approx 1.23$.

7.3 Fronts with cooperative and antagonistic feedback in a convective flow field

We now study cooperative and antagonistic feedback in the presence of background convection. We first study the scenario in the usual two dimensional convection domain having 15 pairs of counterrotating convection rolls at $\mathrm{Ra} = 3000$. We use a Lewis number of $\mathrm{Le} = 0.01$ where the flow field has a large effect on the front. We study cooperative and antagonistic feedback at $\mathrm{Ra}_s = \pm 300$ and $\eta = 50$.

Figure 7.11 shows snapshots in time of a front propagating with cooperative feedback in the presence of background convection. The snapshots are $t \approx 0.5$ apart from each other. A zoomed-in spatial region is shown for better visualization. The lighter products in this case stretch over a large spatial distance. The cooperative feedback annihilates the background convection in the spatial extent covered by the front. The leading edge of the front interacts with the convection roll ahead of it as it propagates. There are secondary plume-like structures behind the leading edge which are formed due to the exothermic reaction.

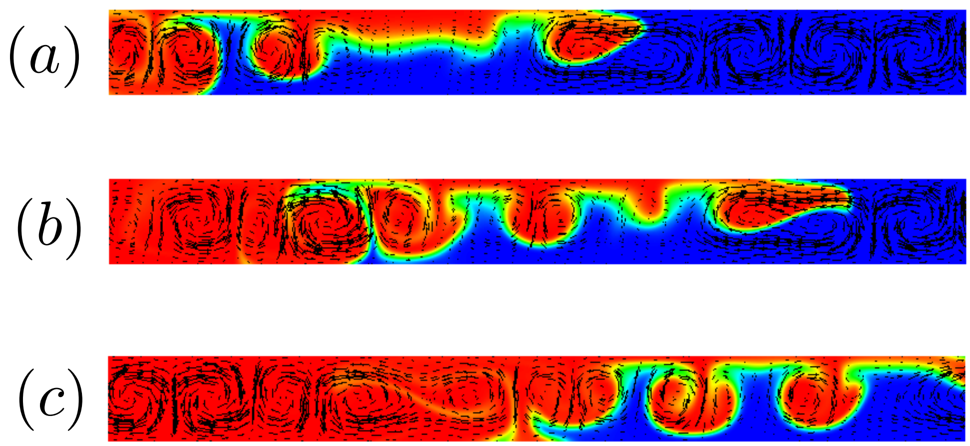

Figure 7.11: Snapshots in time of a front propagating with cooperative feedback in a convective flow field. The relevant parameters are $\mathrm{Ra} = 3000$, $\mathrm{Ra}_s = +300$ and $\eta = 50$. The background flow field is shown by arrows. The snapshots (a), (b) and (c) are approximately $t \approx 0.5$ apart. Color shows concentration (c) where red is products ($c = 1$) and blue is reactants ($c{=}0$). The flow field vectors are visualized by arrows. A zoomed-in spatial region ($10 \le x \le 20$) is shown for better visualization.

Figure 7.12 shows the space-time plot through the midplane slice of Fig. 7.11. The centers of the background convection rolls are shown by the lines in the plot with solid lines representing clockwise convection rolls and dotted lines representing anticlockwise convection rolls. The interaction of the leading edge of the front with the convection rolls is shown by the isolated patch of products in the space-time plot, where the reaction is completed first. The finger-like structures in the space-time plot are descriptive of the complicated features behind the leading edge in Fig. 7.11. An important aspect of cooperative feedback is that the dynamics does not settle to a periodic nature in long time. This aspect can be seen from the isolated patch of products along the diagonal of the space-time plot that is not setting down to a periodic nature. This isolated patch is representative of the leading edge of the front. It is also clear that the finger like disorders in the space-time plot are not periodic.

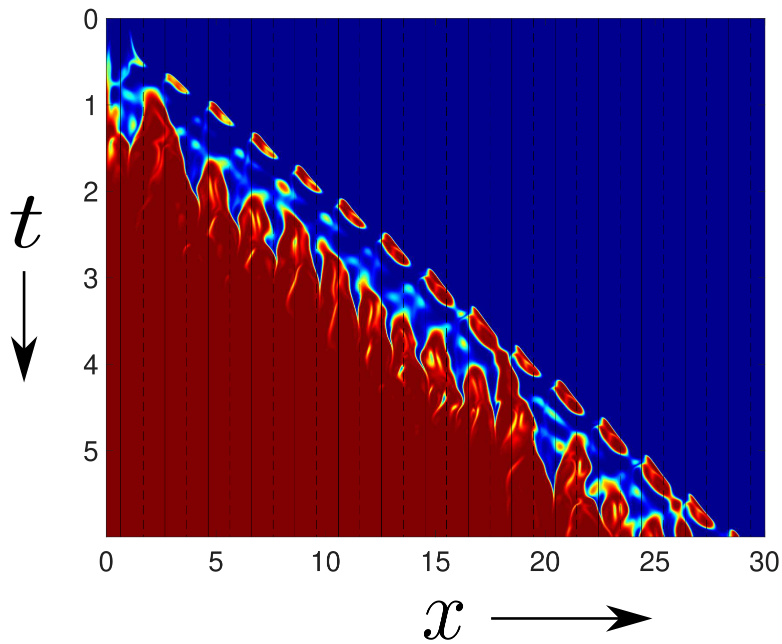

Figure 7.12: Space-time plot for a front with cooperative feedback where $\mathrm{Ra}_s = 300$ and $\eta = 50$ in the presence of convection at $\mathrm{Ra} = 3000$. The concentration field is shown in Fig. 7.11. The spatial location of the thermal convection rolls are indicated by the vertical lines with the centers of convection rolls with a clockwise (counterclockwise) rotation are shown with solid (dashed) lines. Color shows concentration (c) where red is products ($c\!=\!1$) and blue is reactants ($c\!=\!0$).

Figure 7.13 shows the scenario of a front propagating with antagonistic feedback propagating through a chain of convection rolls. The snapshots are again $t \approx 0.5$ apart from each other. In this scenario, the spatial extent covered by the front is smaller. The leading edge or the snout which consists of heavier products extends through a small spatial distance before falling down. The leading edge by this process scoops out isolated patches of reactants inside. The leading edge also interacts with the convection roll ahead of it. The isolated patch of reactants is carried well inside the reaction zone and almost near the end where new convection rolls are forming.

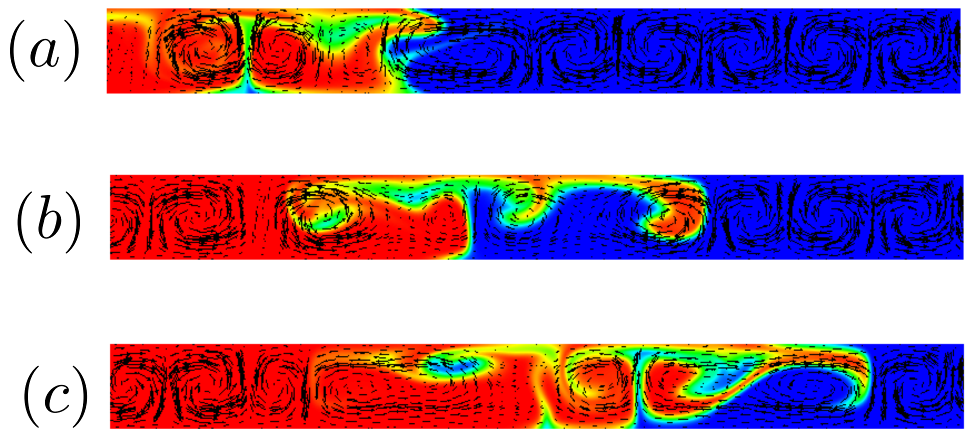

Figure 7.13: Snapshots in time of a front propagating with antagonistic feedback in a convective flow field. The relevant parameters are Ra $= 3000$, Ra$_s$ $= -300$ and $\eta = 50$. The background flow field is shown by arrows. The snapshots (a), (b) and (c) are approximately $t \approx 0.5$ apart. Color shows concentration (c) where red is products ($c = 1$) and blue is reactants ($c\!=\!0$). The flow field vectors are visualized by arrows. A zoomed-in spatial region ($10 \leq x \leq 20$) is shown for better visualization.

The space-time plot for this complicated scenario is shown in Fig. 7.14. The isolated patch of product in the leading edge is still present but is not as frequent as the cooperative case. This is because the leading edge consists of heavier products and is unable to sustain itself for long times and falls down. Here as well, the dynamics does not settle down to a periodic nature for the domains that we have tested. However, the dynamics are more regular than for the cooperative scenario.

We plot the temporal variation of the front velocity for fronts propagating with cooperative and antagonistic feedback in the presence of background convection. Figure 7.15 shows this variation. The antagonistic scenario is shown by the brown curve. It is clear that the front velocity for the antagonistic feedback is regular although not quite periodic. The front

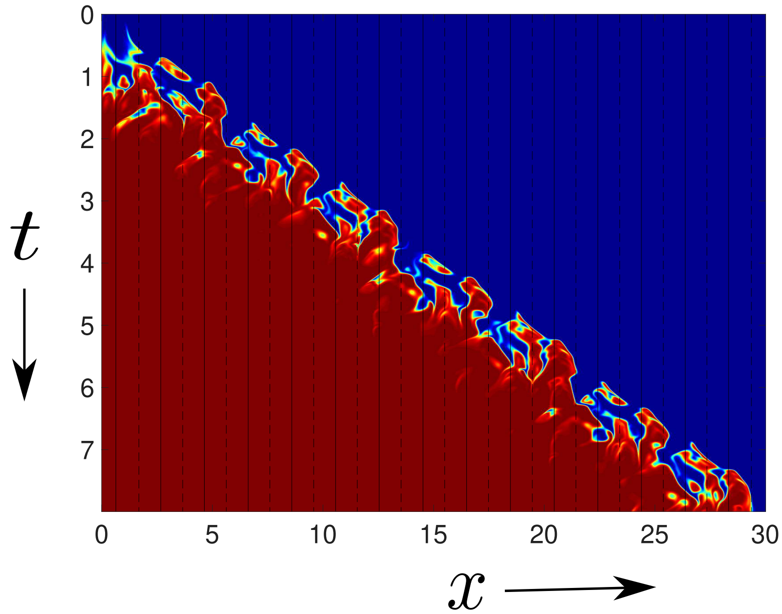

Figure 7.14: Space-time plot for a front with antagonistic feedback where $\mathrm{Ra}_s = -300$ and $\eta = 50$ in the presence of convection at $\mathrm{Ra} = 3000$. The concentration field is shown in Fig. 7.13. The spatial location of the thermal convection rolls are indicated by the vertical lines with the centers of convection rolls with a clockwise (counterclockwise) rotation are shown with solid (dashed) lines. Color shows concentration (c) where red is products (c=1) and blue is reactants (c=0).

velocity for the cooperative feedback has no apparent regular features. The expected trend of the cooperative feedback fronts being faster than the antagonistic feedback fronts is also present when there is background convection.

We next plot the phase portraits for fronts propagating with cooperative and antagonistic feedback in the presence of background convection. Figure 7.16 shows the phase portraits. The phase portraits are plotted in the same window of time as in Fig. 7.15 and the start and the end points of the trajectories are shown by arrows. The phase portrait for cooperative feedback in the presence of background convection is shown in Fig. 7.16(a). No clear signature of repetition of the trajectories is present in the phase portrait. This is suggestive of the aperiodic nature of the dynamics as observed from the space-time plot for this case in

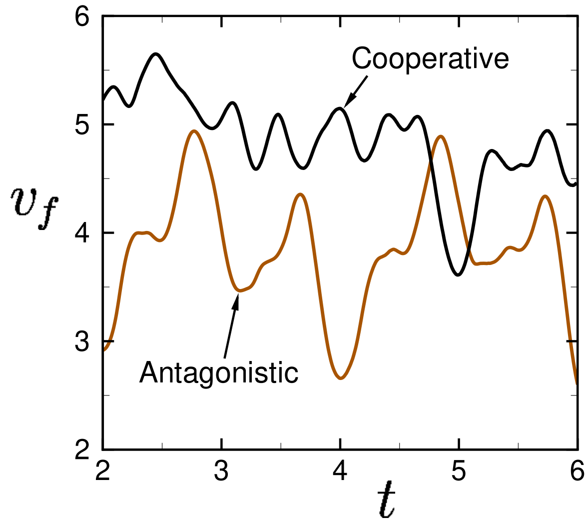

Figure 7.15: The temporal variation of front velocity for fronts propagating with cooperative and antagonistic feedback in the presence of background convection. Relevant parameters are $\mathrm{Ra}_s = \pm 300$, $\eta = 50$ and $\mathrm{Ra} = 3000$.

Fig. 7.12. Figure 7.16 (b) shows the phase portrait for antagonistic feedback in the presence of convection. Although the trajectories in the phase space are not repeating, there is a presence of a somewhat regular structure. This structure is similar to the two lobed oval shape in the phase portrait of this scenario in the absence of convection shown in Fig. 7.10 (b).

We have also explored the presence of periodic dynamics for fronts with cooperative feedback in convection by doubling the size of our domain. We have used a two dimensional domain of aspect ratio $\Gamma_x = 60$ to study the fronts with feedback traveling through a chain of convection rolls at $\mathrm{Ra} = 3000$. The case we examined is identical to the scenario shown in Fig. 7.11 ($\mathrm{Ra}_s = 300$ and $\eta = 50$). Figure 7.17 shows this scenario. The dynamics are clearly not settling to a periodic nature even in this longer domain, however the dynamics show an almost repeating nature near the end. It may be useful in future to explore a larger domain to explore the possibilities of periodic dynamics.

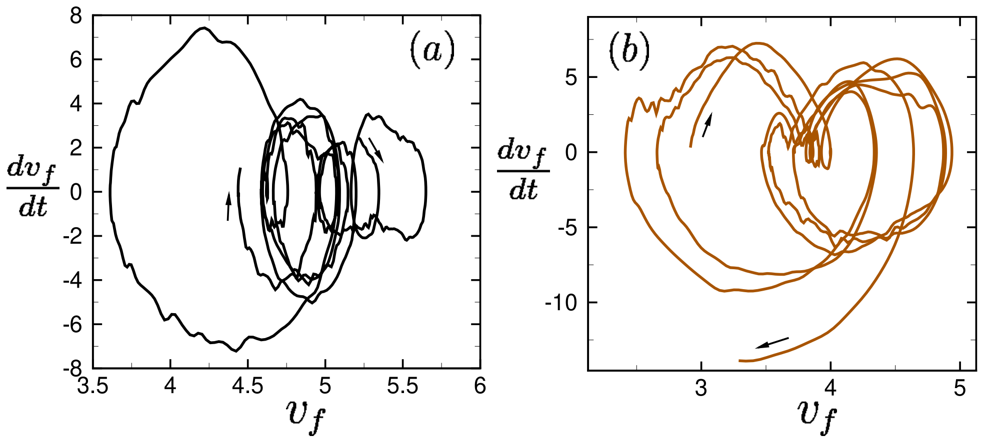

Figure 7.16: Phase portrait of the front velocity for fronts with cooperative and antagonistic feedback $\eta = 50$ in the presence of background convection at Ra = 3000. The time variation of the front velocities for this case are shown in Fig. 7.15. The phase portraits are plotted in the same window of time as in Fig. 7.15. The start and the end points of the trajectories are shown by arrows. (a) Cooperative feedback, $\mathrm{Ra}_s = 300$. (b) Antagonistic feedback, $\mathrm{Ra}_s = -300$.

We next investigate the scenario where we have propagating fronts with feedback in chaotic flow fields. Figure 7.18 shows the scenario of front induced feedback in a chaotic flow field in the cylindrical domain at Ra = 6000. Shown are snapshots of the concentration field with the centers of the underlying convection rolls shown by the black lines. We have used a Lewis number of Le = 0.1 for this study. All the snapshots are at a time $t = 3.4$.

Figure 7.18 (a) shows the scenario without front induced feedback ($\mathrm{Ra}_s = 0$ and $\eta = 0$). We have studied this scenario closely in Ch. 5. The front interface is heavily affected by the underlying defects, spirals and other spatial disorders of the flow field.

Figure 7.18 (b) shows the scenario where we have solutal feedback at $\mathrm{Ra}_s = 6000$. In this case, the reaction zone is much wider as shown by the green region. The reaction zone is not affected by the chaotic flow field except for the leading edge which interacts with the chaotic convection rolls. The front is faster here which is clear from the larger radial extent that has been covered by the front. The solutal convection roll traveling with the

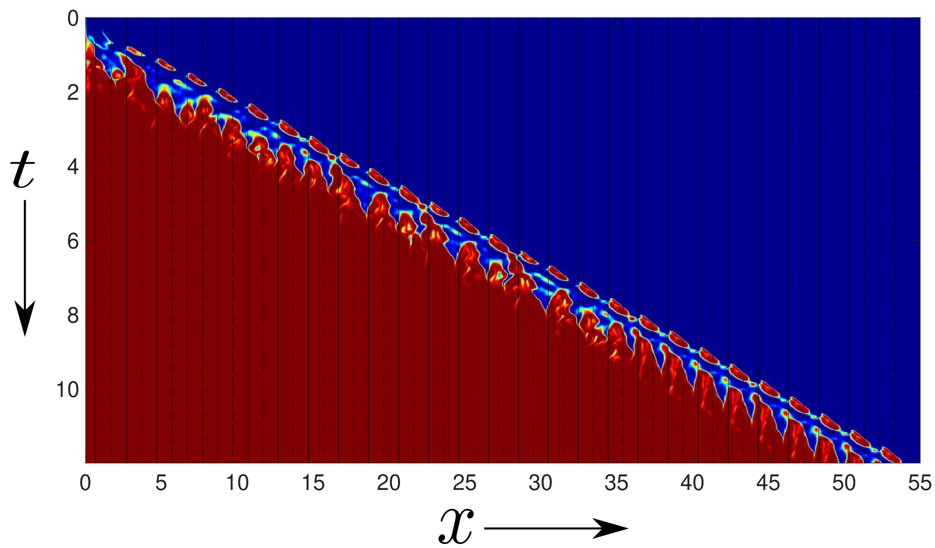

Figure 7.17: Space-time plot for a front with cooperative feedback in the presence of convection in a two dimensional domain of aspect ratio $\Gamma_x = 60$. The relevant parameters are $\mathrm{Ra}_s = 300$, $\eta = 50$ and $\mathrm{Ra} = 3000$. The spatial location of the thermal convection rolls are indicated by the vertical lines with the centers of convection rolls with a clockwise (counterclockwise) rotation are shown with solid (dashed) lines. Color shows concentration (c) where red is products ($c=1$) and blue is reactants ($c=0$).

front has annihilated a number of convection rolls which then reemerge due to the convective instability. Interestingly, these reemerged convection rolls line up to form a target pattern behind the front in a spatial extent spanning 6 convection rolls. The target pattern is unstable because its wavenumber is outside the range of stable wavenumbers at this Rayleigh number described by the Busse balloon [2, 43]. This leads to the reemergence of chaotic rolls behind the target pattern, which starts from the center of the domain. These are examples of pattern forming fronts which we will explore in greater detail in Ch. 8. In this scenario there are two pattern forming fronts where one of them form target patterns in its wake while the other one starting from the center forms chaotic patterns in its wake. If we take a horizontal slice through the middle of the domain in Fig. 7.18 (b), the wavenumber of the target patterns can be found out to be $k_t \approx 3.8$, which is more than the wavenumber of the chaotic rolls in the horizontal slice through the middle of Fig. 7.18 (a) where it is equal to $k_c \approx 2.3$. It is interesting to note that a steady pattern of straight parallel rolls shown in Fig. 5.1 generates a pattern wavenumber of $k \approx \pi$. The wavenumber of $k_t \approx 3.8$ lies outside the Busse balloon for this Rayleigh number and reverts back to the chaotic pattern starting from the center [43]. This suggests that the wavenumber selected by the pattern in the wake of a front with solutal feedback depends on the complex feedback dynamics. In future, it will be interesting to explore the wavenumber selected by the pattern behind the feedback front for a range of solutal and thermal feedback. Pattern forming fronts with a steady state wavenumber of $k \approx \pi$ will be investigated in Ch. 8.

Figure 7.18 (c) shows the scenario of antagonistic feedback at $\mathrm{Ra}_s = -6000$ and $\eta = 18$. In this case, the front is slower than the case of only solutal feedback but it is still faster than the scenario without any feedback in Fig. 7.18 (a). The reaction zone is extended as shown by the green and yellow region. At the instant shown in the snapshot the wake of the front is forming a weak target pattern. The reaction generates a hotspot where $T = 1.1$ which is slightly larger than the temperature of the bottom wall of the domain at $T = 1$.

Figure 7.18 (d) shows the scenario of cooperative feedback in a chaotic flow field at $\mathrm{Ra}_s = 6000$ and $\eta = 18$. This scenario produces a front which is faster than the other cases as shown by the large radial extent that has been covered by the front. This is expected since the cooperative feedback produces faster fronts as explored before. The reaction zone shown by green is widest for this case. Again we see a target pattern that emerges in the wake of the front. The target pattern shows disorder in its center which is expected since the system is chaotic.

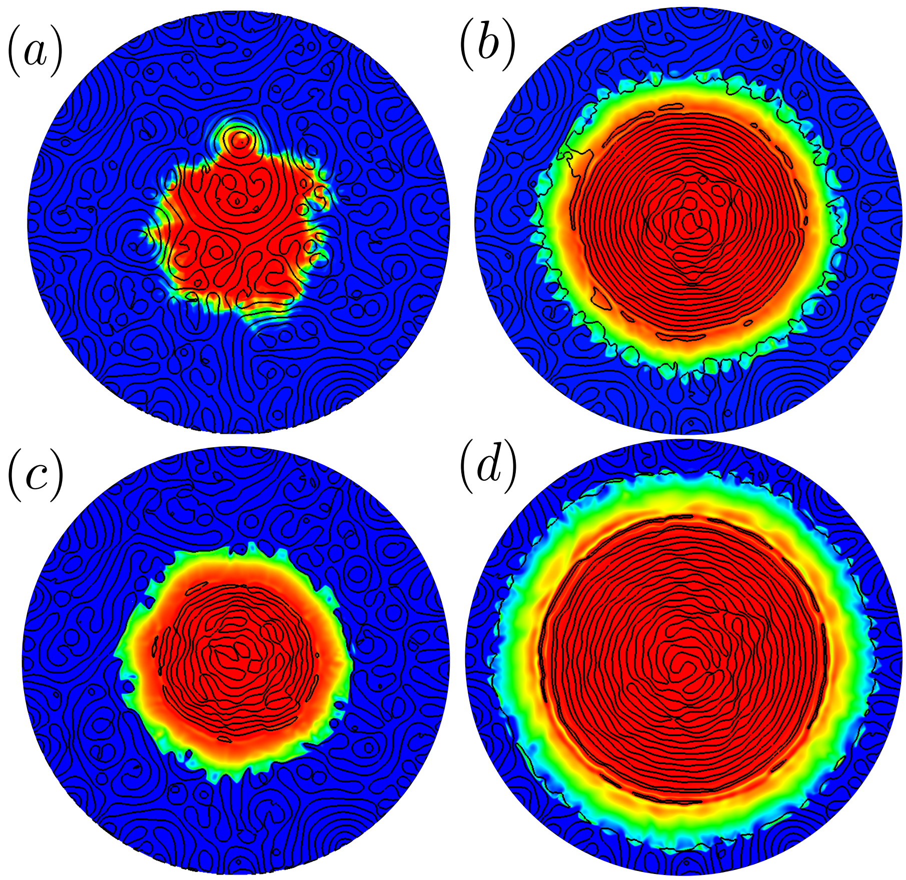

Figure 7.18: Snapshots of the concentration field for cooperative and antagonistic feedback in a spatiotemporally chaotic flow field in a cylindrical domain at Ra = 6000 and Le = 0.1. Snapshots of the scenarios where there is no feedback and where only solutal feedback is present is also shown for reference. Red is pure products and blue is pure reactants. The black lines represent the line contour of $T = 1/2$ which locate the center of the convection rolls. All the snapshots are taken at a time $t = 3.4$ from the initiation of the front in the center of the domain. (a) The scenario without feedback which has been studied in depth in Ch. 5. (b) The scenario with only solutal feedback at $\mathrm{Ra}_s = 6000$. (c) A front with antagonistic feedback for $\eta = 18$ and $\mathrm{Ra}_s = -6000$. The maximum temperature for this case is slightly more than the bottom wall of the domain at $T = 1.11$. (d) A front with cooperative feedback $\eta = 18$ and $\mathrm{Ra}_s = 6000$. The maximum temperature for this case is $T = 1.16$.

Chapter 8

Pattern forming fronts

In this section we will briefly explore pattern forming fronts. In many situations of interest, a front propagates while leaving a trail of spatial structures behind. Examples of pattern forming fronts include dendritic growth fronts, crystal growth fronts and dissolution fronts in rocks and flame fronts which form cellular patterns in their wake [24, 25]. We have also encountered this phenomenon for fronts propagating with solutal and thermal feedback in convective flow fields in Ch. 6 and Ch. 7. As can be seen from Fig. 6.8 (e)-(g), the solutally induced stretched front annihilates the convection rolls locally as it propagates. However, as the front passes through a location the convection rolls reemerge in its wake because of the convective instability. The reemerged convection rolls form a pattern forming front which fills the spatial region without convection rolls to the left of the front which now consists of products. A similar scenario is observed for fronts with cooperative and antagonistic feedback propagating through a convective flow as shown in Fig. 7.11 and Fig. 7.13. We have also encountered pattern forming fronts in the scenario of front induced feedback in a chaotic flow field as shown in Fig. 7.18. For example in Fig. 7.18 (b), the pattern forming convection roll front behind the reaction zone (shown in green) forms a target pattern of wavenumber $k_t \approx 3.8$. There is also the presence of a propagating chaotic instability that develops from the center of the domain which travels outward radially while reorienting the target roll patterns into spatiotemporally chaotic rolls. This is an example of a *chaotic* pattern forming front and has not been explored further in this dissertation.

An important aspect of a pattern forming front is that the velocity and wavenumber of the patterns selected are not arbitrary and are closely linked to the nature of the instability [2]. Here, we study the pattern forming fronts of convection rolls in a two-dimensional domain of aspect ratio $\Gamma_x = 30$ near the onset of convective instability. We use 30 equally spaced square spectral elements in the domain and a 16th order Lagrangian interpolation polynomial to discretize each element. We use a hot sidewall boundary condition $T = 1$ at the left wall at $x = 0$. This leads to the formation of a convection roll which then propagates in the positive x-direction. We use a range of Rayleigh numbers between $1750 \leq \mathrm{Ra} \leq 4800$ to study the propagation of the convection rolls. A larger Rayleigh number $\mathrm{Ra} > 4800$ causes the entire fluid layer to simultaneously erupt due to the convective instability prior to the front traveling across the domain. We cover a range of reduced Rayleigh numbers $0.025 \leq \epsilon \leq 1.81$, which covers a large range of thermal driving above the onset of thermal convection.

Figure 8.1 shows the snapshots of a pattern forming front at $\mathrm{Ra} = 2100$ at different times. Red represents hot rising fluid and blue represents cold descending fluid as usual. Figure 8.1 (a) shows a time of $t = 0.1$ from the start of the simulation. Figure 8.1 (b)-(g) shows the pattern forming front for $1 \leq t \leq 6$ with each snapshot at $\Delta t = 1$ apart.

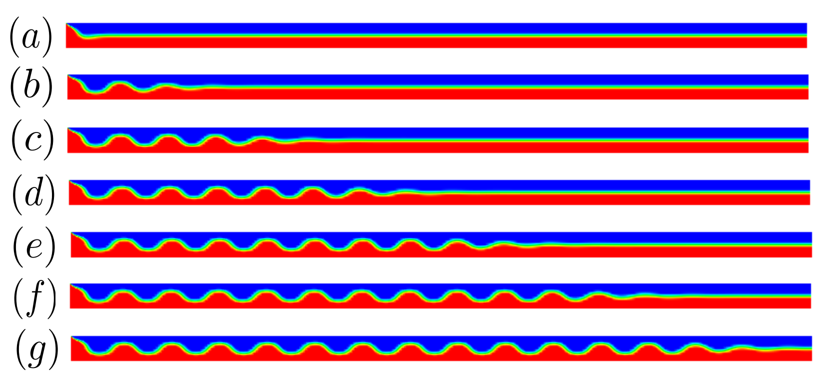

Figure 8.1: Snapshots of a propagating pattern forming front. Shown is the color contour of temperature between $0.4 \leq T \leq 0.6$. Red is hot rising fluid and blue is cold descending fluid. The Rayleigh number is $R = 2100$. The snapshots from (b)-(g) are 1 vertical diffusion time unit apart. (a) $t = 0.1$ (b) $t = 1$ (c) $t = 2$ (d) $t = 3$ (e) $t = 4$ (f) $t = 5$ (g) $t = 6$.

Figure 8.2 shows the space-time plot of the pattern forming front shown in Fig. 8.1 by taking a slice at the midplane $z = 1/2$ of the flow field. It is clear that around $t \approx 6.5$, the front has reached the right wall of the domain. The inverse slope of the line through the boundary of the pattern forming front in Fig. 8.2 is equal to the front velocity.

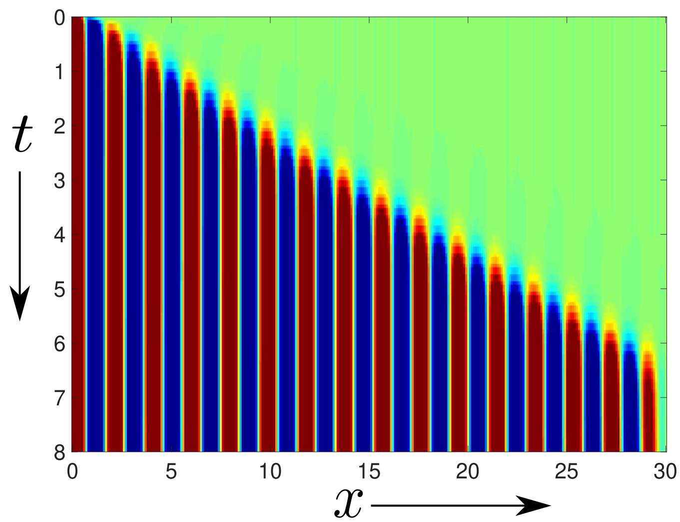

Figure 8.2: Space-time plot of a propagating pattern forming front obtained by taking a horizontal slice at the vertical midplane of the temperature fields shown in Fig. 8.1. Color shows temperature where red is hot rising fluid and blue is cold descending fluid.

The dynamics near the onset of convective instability can be described using the amplitude equation [1, 2]. The linear selection criterion suggests that the front velocity of the pattern forming front is given by

$$v_{fp} = 2\xi_0 \tau_0^{-1} \sqrt{\epsilon}, \tag{8.1}$$

where ξ_0 and τ_0 are the parameters of the amplitude equation [10, 94–97]. For Prandtl number $\sigma = 1$ and no-slip top and bottom walls, the values of these parameters are $\xi_0 = 0.38$ and $\tau_0^{-1} = 13$ which can be obtained using Table II in Ref. [97].

Figure 8.3 shows excellent agreement between theory and our numerical results, where the black solid line is the theoretical prediction given by Eq. 8.1 and the blue circles are the data points from numerical simulation. In practice, we track the x-coordinate of the tip of the propagating front to obtain the front velocity. This agreement with theory for the front velocity has also been reported in a numerical study of the Swift-Hohenberg equation [94] and the two-dimensional Boussinesq equations [98]. Agreement with theory was also shown in an experiment on propagating pattern forming fronts in Rayleigh-Bénard convection by Ref. [96] where a range of $4 \times 10^{-4} \leq \epsilon \leq 2.5 \times 10^{-1}$ was used. The experiment was conducted using water with Prandtl number $\sigma = 5.373$. Our results show that the theoretical prediction for the front velocity is quite accurate for $0.025 \lesssim \epsilon \lesssim 1.81$ which extends beyond the onset of convective instability.

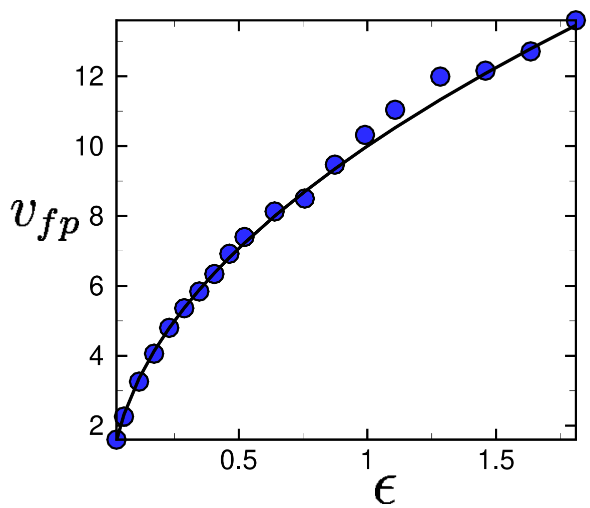

Figure 8.3: The front velocity as a function of ϵ for the pattern forming front. The blue circles represent the data points from numerical simulations and the black solid line is the theoretical prediction given by Eq. 8.1.

Figure 8.4 shows the variation of the wavelength λ of the patterns behind the front with ϵ. The black solid line in Fig. 8.4 is a curvefit of the form $\lambda/\lambda_0 = 1 - 0.1233\sqrt{\epsilon}$, where $\lambda_0 = 2.049$ which is similar to the wavelength found in steady state where $\lambda_{\text{eq}} \approx 2$. The steady state wavelength is found from the fact that we get 15 pairs of counterrotating convection rolls in a domain of aspect ratio $\Gamma_x = 30$ after the front has propagated through the entire domain length and the pattern has fully developed. This yields $\lambda_{\rm eq} = 30/15 = 2$. This relation is similar to the one obtained in the experiment by Ref. [96] where it was found that $\lambda/\lambda_0 = 1 - 0.18\sqrt{\epsilon}$, where $\lambda_0 = 2.29$. The experiment used a domain of aspect ratio $\Gamma_x \approx 27$ which yielded 12 pairs of counterrotating convection rolls. Thus $\lambda_{\rm eq} = 2.27$ which was found to be close to λ_0. Overall, our results can be described by the form of the curvefit used by Ref. [96]. However, our numerical results are for much larger values of ϵ than what was used in the experiment.

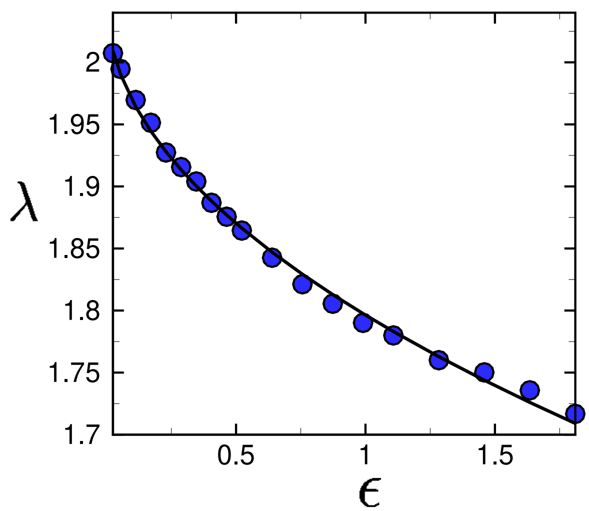

Figure 8.4: The wavelength as a function of ϵ for the pattern forming front. The blue circles represent the numerical points and the black solid line through the data is a curve fit of the form $\lambda = 2.049(1 - 0.1233\epsilon^{1/2})$.

The wavenumber of the pattern selected is given by $k = 2\pi/\lambda$. It is interesting to note that a linear dependence of the wavenumber with ϵ near the onset of convective instability has been predicted theoretically [2, 94, 98]. The linear dependence of the wavenumber with ϵ near the onset has also been verified in a numerical study of pattern forming convection rolls by Ref. [98]. This result is however in contrast with the experimental study done by Ref. [96] which showed that the wavenumber was inversely related to $\epsilon^{1/2}$. This discrepancy was possibly attributed to the sidewall boundary condition used in the experiment [98]. Our simulations are for ϵ values which are larger than previous simulations and experiments, and therefore, we cannot directly compare our results with previous results. It is interesting to note that our results for the wavelength follow a relation similar to the one obtained in the experiment on pattern forming convection roll front near the onset of convective instability by Ref. [96]. However, our results are for relatively large values of ϵ above the onset of convective instability and we have not conducted a targeted investigation very close to the onset ($\epsilon \ll 1$), which would be required to explore this observed discrepancy.

Chapter 9

Conclusions

We have used high-order numerical simulations to study autocatalytic front propagation and feedback in convective flow fields. We have solved the Boussinesq equations along with a reaction-advection-diffusion equation using an FKPP nonlinearity. Overall, front propagation with feedback in convective flow fields is an immensely broad problem characterized by a vast parameter space which includes two different Rayleigh numbers Ra, Ra_s, heat release parameter η, Lewis number Le, reaction rate ξ, Prandtl number σ and aspect ratio Γ. What makes the problem complicated is that these parameters can be varied independently. Here, we have conducted a targeted investigation by fixing our Prandtl number to $\sigma = 1$, which is consistent with Rayleigh-Bénard convection experiments with compressed gases and where the flow field undergoes the state of spiral defect chaos. We also fixed our reaction rate to a value of $\xi = 9$ such that our reaction and flow time scales are comparable. We have focused our investigation in the regime where the flow field has a significant effect on the front propagation. Our investigation cover a range of Péclet numbers $0 \leq \mathrm{Pe} \lesssim 1100$ and intermediate Damköhler number $\mathrm{Da} \sim \mathcal{O}(1)$ which yield fronts with finite width and is away from the well understood theoretical insights which use thin front approximations at large Péclet and Damköhler numbers ($\mathrm{Da} \gg 1, \mathrm{Pe} \gg 1$).

We have quantified the power law scaling of the front velocity with the underlying fluid velocity for a range of flow fields. We have found that weakly chaotic flow fields *slow down* the front when compared to straight parallel rolls because of convection rolls which orient themselves perpendicularly to the direction of front propagation. However with the onset of an oscillatory instability in the flow field, the front velocity increases in a weakly turbulent fluid flow. This increment is partly due to the wrinkled front interface which increases the effective area in which the reaction takes place. The wrinkled front interface is a fractal with a box counting dimension that increases with the flow complexity.

We have studied front propagation with feedback where an autocatalytic reaction is exothermic and the reactants and products can vary in density. Solutal feedback creates a single self-organized convection roll which travels with the front while thermal feedback creates a pair of counter rotating convection rolls because of a local hotspot at the front.

For small values of the solutal Rayleigh number the characteristic fluid velocity scales linearly, and the front velocity and mixing length scale quadratically, with increasing solutal Rayleigh number. For small solutal Rayleigh numbers the front geometry is described by a curve that is nearly antisymmetric about the horizontal midplane. For large values of the solutal Rayleigh number the characteristic fluid velocity, the front velocity, and the mixing length exhibit square-root scaling and the front shape collapses onto an asymmetric self-similar curve. In the presence of counterrotating convection rolls, the mixing length decreases while the front velocity increases and the concentration field exhibits chemical oscillations with time.

For small values of heat release by the reaction the fluid velocity scales linearly while the front velocity scales as three-halves with the heat release parameter and the two counterrotating convection rolls are nearly symmetric. For large values of heat release, the symmetry gets broken and the front and fluid velocities scale as the square root of the heat release parameter. The concentration field gets stretched and disordered for large values of heat release and secondary fluid rolls develop.

In the presence of both thermal and solutal feedback the dynamics can be cooperative or antagonistic depending on the relative sign of Ra_s and η. Fronts with cooperative feedback are always found to be faster than fronts with antagonistic feedback and fronts with only solutal or thermal feedback. Cooperative and antagonistic feedback induce temporal oscillations in the concentration field for certain parameters. The situation becomes more complicated in the presence of background convection where the system does not settle to periodic dynamics for the range of parameters and domain lengths we have studied. In three dimensional chaotic flow fields, front induced feedback morphs the chaotic convection rolls to form a target pattern in its wake. After the front has passed, the target pattern revert back to a chaotic pattern because of the convective instability.

Lastly, we have quantified pattern forming fronts of convection rolls over a large range of thermal driving above the onset of convection. We have found that the velocity of the front agrees with theoretical predictions using the amplitude equation. The variation of the wavelength selected by the pattern with the reduced Rayleigh number (ϵ) is found to follow a similar trend that was obtained in an earlier experiment conducted on pattern forming fronts near the onset of convection [96], although our results are for larger values of ϵ than what was used in the experiment.

There are several implications from the present study that would benefit from further investigation. An experimental realization of the present project would be a study of a bi-molecular reaction fronts in the presence of Rayleigh-Bénard convection. Our computational approach is quite flexible and it is straightforward to change the different parameters quantifying front propagation studies in the future. For instance, it will be particularly interesting to explore front propagation in a convective fluid with $\sigma = 7$ which aligns with an aqueous chemical reaction. It will also be of interest to change the reaction nonlinearity to Arrhenius type reactions which can model combustion [99]. A particularly interesting direction would be the study of fronts for even higher Rayleigh numbers (Ra > 25000) which will lead to turbulence [100]. Recently, it has been found that turbulent Rayleigh-Bénard convection displays a range of length scales from extremely small scale features to *superstructures* which are greater than the depth of the convection layer [101]. It would be interesting to study propagating fronts in these flow fields which will possibly help in understanding the reactive transport in the surface of a star [23]. There are several nonlinear dynamical tools such as exact coherent structures (ECS) [102] which identify unstable solutions and Lagrangian coherent structures (LCS) [103] which identify transport barriers in the flow. These tools have been used in spatiotemporally disordered flows such as Rayleigh-Bénard convection and Kolmogorov flow to identify important regions in state space where trajectories often visit or where there are transport barriers [104, 105]. Front diagnostic tools that locally quantify front propagation such as the reaction zone angle ϕ and front velocity v_f which have been developed in this work can then be used to study the dependence of front propagation on these important geometric regions of the fluid dynamics. The dependence of front propagation and feedback on the range of spatially disordered flow fields quantified in this dissertation will be helpful in the study of reactive transport processes in industries such as mixing of chemicals and dyes, geophysical transport such as the spread of blooming plankton in open oceans, spread of reactive pollutants in the atmosphere and the propagation of wild fire fronts.

Bibliography

[1] W. van Saarloos. Front propagation into unstable states. *Phys. Rep*, 386:29–222, 2003.

[2] M. C. Cross and P. C. Hohenberg. Pattern formation outside of equilibrium. *Rev. Mod. Phys.*, 65:851–1112, 1993.

[3] A. N. Wetzel, L. M. Smith, and S. N. Stechmann. Discontinuous fronts as exact solutions to precipitating quasi-geostrophic equations. *SIAM J. Appl. Math*, 79:1341–1366, 2019.

[4] E. Hernández-Garcıa and C. López. Sustained plankton blooms under open chaotic flows. *Ecol. Complex.*, 1:253–259, 2004.

[5] W. W. Hargrove, R. H. Gardner, M. G. Turner, W. H. Romme, and D. G. Despain. Simulating fire patterns in heterogeneous landscapes. *Ecol. Model*, 135:243–263, 2000.

[6] M. Belk, K. G. Kostarev, V. Volpert, and T. M. Yudina. Frontal photopolymerization with convection. *J. Phys. Chem. B*, 107:10292–10298, 2003.

[7] V. A. Sabelnikov and A. N. Lipatnikov. Transition from pulled to pushed fronts in premixed turbulent combustion: Theoretical and numerical study. *Combust. Flame*, 162:2893–2903, 2015.

[8] D. Barkley. Taming turbulent fronts by bending pipes. *J. Fluid Mech*, 872:1–4, 2019.

[9] R. A. Fisher. The wave of advance of advantageous genes. *Annal. Eugenics*, 7:355–369, 1937.

[10] A. N. Kolmogorov, I. G. Petrovskii, and N. S. Piskunov. A study of the equation of diffusion with increase in the quantity of matter, and its application to a biological problem. *Bull. Moscow Univ. Math.*, 1:1–25, 1937.

[11] J. D. Murray. *Mathematical Biology II: Spatial Models and Biomedical Applications*. Springer New York, 2003.

[12] A. M. Turing. The chemical basis of morphogenesis. *Phil. Trans. R. Soc. Lond. B*, 237:37–72, 1952.

[13] K. R. Sreenivasan, R. Ramshankar, and C. H. Meneveau. Mixing, entrainment and fractal dimensions of surfaces in turbulent flows. *Proc. R. Soc. Lond. A*, 421:79–108, 1989.

[14] M. N. Kuperman and H. S. Wio. Front propagation in epidemiological models with spatial dependence. *Physica A*, 272:206–222, 1999.

[15] T. John and I. Mezic. Maximizing mixing and alignment of orientable particles for reaction enhancement. *Phys. Fluids*, 19:123602, 2007.

[16] P. K. Trong, J. Guck, and R. E. Goldstein. Coupling of active motion and advection shapes intracellular cargo transport. *Phys. Rev. Lett.*, 109:028104, 2012.

[17] R. Tiani, A. De Wit, and L. Rongy. Surface tension- and buoyancy-driven flows across horizontally propagating chemical fronts. *Adv. Colloid Interface Sci.*, 225:76–83, 2018.

[18] R. J. Field and M. Burger. *Oscillations and traveling waves in chemical systems*. Wiley, 1985.

[19] L. Rongy. *Influence of Marangoni and buoyancy convection on the propagation of reaction-diffusion fronts*. PhD thesis, Université Libre De Bruxelles, 2008.

[20] J. E. Simpson. *Gravity currents: In the environment and the laboratory.* Cambridge university press, 1999.

[21] I. Bou Malham, N. Jarrige, J. Martin, N. Rakotomalala, L. Talon, and D. Salin. Lock-exchange experiments with an autocatalytic reaction front. *J. Chem. Phys.*, 133: 244505, 2010.

[22] J. O. Shin, S. B. Dalziel, and P. F. Linden. Gravity currents produced by lock exchange. *J. Fluid Mech*, 521:1–34, 2004.

[23] N. Vladimirova. Model flames in the boussinesq limit: Rising bubbles. *Combust. Theory Model*, 11:377–400, 2007.

[24] B. Jamtveit and Ø. Hammer. Sculpting of rocks by reactive fluids. *Geochem. Perspect*, 1:341–342, 2012.

[25] G. I. Sivashinsky. Instabilities, pattern formation, and turbulence in flames. *Annu. Rev. Fluid Mech*, 15:179–199, 1983.

[26] M. Abel, A. Celani, D. Vergni, and A. Vulpiani. Front propagation in laminar flows. *Phys. Rev. E*, 64:046307, 2001.

[27] M. Abel, M. Cencini, D. Vergni, and A. Vulpiani. Front speed enhancement in cellular flows. *Chaos*, 12:481–488, 2002.

[28] P. W. Megson, M. L. Najarian, K. E. Lilienthal, and T. Solomon. Pinning of reaction fronts by burning invariant manifolds in extended flows. *Phys. Fluids*, 27:023601, 2015.

[29] M. Doan, J. J. Simons, K. Lilienthal, T. Solomon, and K. A. Mitchell. Barriers to front propagation in laminar, three-dimensional fluid flows. *Phys. Rev. E*, 97:033111, 2018.

[30] A. Pocheau and F. Harambat. Front propagation in a laminar cellular flow: Shapes, velocities, and least time criterion. *Phys. Rev. E*, 77:036304, 2008.

[31] B. D. Haslam and P. D. Ronney. Fractal properties of propagating fronts in a strongly stirred fluid. *Phys. Fluids*, 7:1931–1937, 1995.

[32] L. Rongy, A. De Wit, and G. M. Homsy. Asymptotic structure of steady nonlinear reaction-diffusion-Marangoni convection fronts. *Phys. Fluids*, 20:072103, 2008.

[33] F. Rossi, M. A. Budroni, N. Marchettini, and J. Carballido-Landeira. Segmented waves in a reaction-diffusion-convection system. *Chaos*, 22:037109, 2012.

[34] J. Martin, N. Rakotomalala, D. Salin, and M. Böckmann. Buoyancy-driven instability of an autocatalytic reaction front in a Hele-Shaw cell. *Phys. Rev. E*, 65:051605, 2002.

[35] N. Jarrige, I. Bou Malham, J. Martin, N. Rakotomalala, D. Salin, and L. Talon. Numerical simulations of a buoyant autocatalytic reaction front in tilted Hele-Shaw cells. *Phys. Rev. E*, 81:066311, 2010.

[36] J. Mahoney, D. Bargteil, M. Kingsbury, K. Mitchell, and T. Solomon. Invariant barriers to reactive front propagation in fluid flows. *EPL*, 98:44005, 2012.

[37] P. Constantin, A. Kiselev, A. Oberman, and L. Ryzhik. Bulk burning rate in passive-reactive diffusion. *Arch. Rational Mech. Anal.*, 154:53–91, 2000.

[38] S. Mukherjee and M. R. Paul. Velocity and geometry of propagating fronts in complex convective flow fields. *Phys. Rev. E*, 99:012213, 2019.

[39] S. Mukherjee and M. R. Paul. Propagating fronts in fluids with solutal feedback. *Phys. Rev. E*, 101:032214, 2020.

[40] See https://nek5000.mcs.anl.gov for more information about the NEK5000 solver.

[41] S. Chandrasekhar. *Hydrodynamic and Hydromagnetic Stability.* Dover Publications, 1981.

[42] S. W. Morris, E. Bodenschatz, D. S. Cannell, and G. Ahlers. Spiral defect chaos in large aspect ratio Rayleigh–Bénard convection. *Phys. Rev. Lett.*, 71:2026–2029, 1993.

[43] E. Bodenschatz, W. Pesch, and G. Ahlers. Recent developments in Rayleigh-Bénard convection. *Annu. Rev. Fluid Mech*, 32:709–778, 2000.

[44] M. R. Paul, K. H. Chiam, M. C. Cross, P. F. Fischer, and H. S. Greenside. Pattern formation and dynamics in Rayleigh–Bénard convection: numerical simulations of experimentally realistic geometries. *Physica D*, 184:114–126, 2003.

[45] M. R. Paul, M. I. Einarsson, P. F. Fischer, and M. C. Cross. Extensive chaos in Rayleigh–Bénard convection. *Phys. Rev. E*, 75:045203, 2007.

[46] F. Ginelli, H. Chaté, R. Livi, and A. Politi. Covariant Lyapunov vectors. *J. Phys. A*, 46:254005, 2013.

[47] M. Xu and M. R. Paul. Covariant Lyapunov vectors of chaotic Rayleigh–Bénard convection. *Phys. Rev. E*, 93:062208, 2016.

[48] M. Xu. *Spatiotemporal Chaos in Large Systems Driven Far-From-Equilibrium: Connecting Theory with Experiment.* PhD thesis, Virginia Tech, 2017.

[49] S. Weinberger. What is... persistant homology? *Not. Am. Math. Soc.*, 58:36–39, 2011.

[50] M. Kramár, R. Levanger, J. Tithof, B. Suri, M. Xu, M. R. Paul, M. F. Schatz, and K. Mischaikow. Analysis of Kolmogorov flow and Rayleigh–Bénard convection using persistent homology. *Physica D*, 334:82–98, 2016.

[51] G. K. Vallis, D. J. Parker, and S. M Tobias. A simple system for moist convection: the Rainy–Bénard model. *J. Fluid Mech*, 862:162–199, 2019.

[52] C. Sotin and S. Labrosse. Three-dimensional thermal convection in an iso-viscous, infinite Prandtl number fluid heated from within and from below: applications to the transfer of heat through planetary mantles. *Phys. Earth Planet. Inter*, 112:171–190, 1999.

[53] M. S. Miesch and J. Toomre. Turbulence, magnetism, and shear in stellar interiors. *Annu. Rev. Fluid Mech*, 41:317–345, 2009.

[54] T. H. Solomon and J. P. Gollub. Passive transport in steady Rayleigh–Bénard convection. *Phys. Fluids*, 31:1372–1379, 1988.

[55] M. N. Rosenbluth, H. L. Berk, I. Doxas, and W. Horton. Effective diffusion in laminar convective flows. *Phys. Fluids*, 30:2636–2647, 1987.

[56] K. H. Chiam, M. C. Cross, H. S. Greenside, and P. F. Fischer. Enhanced tracer transport by the spiral defect chaos state of a convecting fluid. *Phys. Rev. E*, 71: 036205, 2005.

[57] C. O. Mehrvarzi and M. R. Paul. Front propagation in a chaotic flow field. *Phys. Rev. E*, 90:012905, 2014.

[58] C. O. Mehrvarzi. Active transport in chaotic Rayleigh–Bénard convection. Master's thesis, Virginia Tech, 2014.

[59] C. R. Koudella and Z. Neufeld. Reaction fronts in a turbulent flow. *Phys. Rev. E*, 70: 026307, 2004.

[60] T. D. Nevins and D. H. Kelley. Optimal stretching in advection–reaction–diffusion systems. *Phys. Rev. Lett*, 117:164502, 2016.

[61] L. Rongy and A. De Wit. Buoyancy-driven convection around exothermic autocatalytic chemical fronts traveling horizontally in covered thin solution layers. *J. Chem. Phys.*, 131:184701, 2009.

[62] J. A. Pojman and I. R. Epstein. Convective effects on chemical waves. 1. Mechanisms and stability criteria. *J. Phys. Chem.*, 94:4966–4972, 1990.

[63] J. A. Pojman, I. R. Epstein, T. J. McManus, and K. Showalter. Convective effects on chemical waves. 2. Simple convection in the iodate-arsenous acid system. *J. Phys. Chem.*, 95:1299–1306, 1991.

[64] L. Rongy, N. Goyal, E. Meiburg, and A. De Wit. Buoyancy-driven convection around chemical fronts traveling in covered horizontal solution layers. *J. Chem. Phys.*, 127: 114710, 2007.

[65] Y. Wu, D. A. Vasquez, B. F. Edwards, and J. W. Wilder. Convective chemical-wave propagation in the Belousov-Zhabotinsky reaction. *Phys. Rev. E*, 51:1119–1127, 1995.

[66] M. C. Rogers and S. W. Morris. The heads and tails of buoyant autocatalytic balls. *Chaos*, 22:037110, 2012.

[67] M. C. Rogers, A. Zebib, and S. W. Morris. Autocatalytic plume pinch–off. *Phys. Rev. E*, 82:066307, 2010.

[68] D. A. Vasquez, J. M. Littley, J. W. Wilder, and B. F. Edwards. Convection in chemical waves. *Phys. Rev. E*, 50:280–284, 1994.

[69] L. Rongy, G. Schuszter, A. Sinkó, T. Tóth, D. Horváth, A. Tóth, and A. De Wit. Influence of thermal effects on buoyancy-driven convection around autocatalytic chemical fronts propagating horizontally. *Chaos*, 19:023110, 2009.

[70] M. A. Budroni, V. Upadhyay, and L. Rongy. Making a simple A + B → C reaction oscillate by coupling to hydrodynamic effect. *Phys. Rev. Lett*, 122:244502, 2019.

[71] A. De Wit. Chemo-hydrodynamic patterns and instabilities. *Annu. Rev. Fluid Mech*, 52:531–55, 2020.

[72] M. J. Ablowitz and A. Zeppetella. Explicit solutions of Fisher's equation for a special wave speed. *Bull. Math. Biol.*, 41:835–840, 1979.

[73] P. K. Brazhnik and J. J. Tyson. On traveling wave solutions of Fisher's equation in two-spatial dimensions. *SIAM J. Appl. Math.*, 60:371–391, 1999.

[74] A. Kiselev and L. Ryzhik. An upper bound for the bulk burning rate for systems. *Nonlinearity*, 14:1297–1310, 2001.

[75] U. Ebert and W. van Saarloos. Front propagation into unstable states: universal algebraic convergence towards uniformly translating pulled fronts. *Physica D*, 146: 1–99, 2000.

[76] J. J. Tyson and J. P. Keener. Singular perturbation theory of traveling waves in excitable media (a review). *Physica D*, 32:327–361, 1988.

[77] L. N. Trefethen. *Spectral methods in MATLAB*. SIAM, 2000.

[78] M. O. Deville, P. F. Fischer, and E. H. Mund. *High-order methods for incompressible fluid flow*, volume 9. Cambridge University Press, 2002.

[79] P. F. Fischer. An overlapping Schwarz method for spectral element solution of the incompressible Navier-Stokes equations. *J. Comput. Phys*, 133:84–101, 1997.

[80] J. D. Scheel. *Rotating Rayleigh-Bénard convection*. PhD thesis, California Institute of Technology, 2007.

[81] K. H. Chiam, M. R. Paul, M. C. Cross, and H. S. Greenside. Mean flow and spiral defect chaos in Rayleigh–Bénard convection. *Phys. Rev. E*, 67:056206, 2003.

[82] A. Karimi and M. R. Paul. Quantifying spatiotemporal chaos in Rayleigh–Bénard convection. *Phys. Rev. E*, 85:046201, 2012.

[83] P. Clavin and F. A. Williams. Theory of premixed-flame propagation in large-scale turbulence. *J. Fluid Mech*, 90:589–604, 1979.

[84] Y. Pomeau. Dispersion dans un écoulement en présence de zones de recirculation. *C. R. Acad. Sci.*, 301:1323–1326, 1985.

[85] E. Beauvier, S. Bodea, and A. Pocheau. Front propagation in a regular vortex lattice: Dependence on the vortex structure. *Phys. Rev. E*, 96:053109, 2017.

[86] D. A. Egolf, I. V. Melnikov, and E. Bodenschatz. Importance of local pattern properties in spiral defect chaos. *Phys. Rev. Lett.*, 80:3228–3231, 1998.

[87] J. D. Farmer, E. Ott, and J. A. Yorke. The dimension of chaotic attractors. *Physica D*, 7:153–180, 1983.

[88] H. O. Peitgen, H. Jürgens, and D. Saupe. *Chaos and fractals: New frontiers of science*. 2006.

[89] B. B. Mandelbrot. *The fractal geometry of nature*. W. H. Freeman New York, 1983.

[90] A. R Kerstein. Fractal dimension of turbulent premixed flames. *Combust. Sci. Technol*, 60:441–445, 1988.

[91] R. Ramshankar and J. P. Gollub. Transport by capillary waves. Part II: scalar dispersion and structure of the concentration field. *Phys. Fluids A*, 3:1344–1350, 1991.

[92] A. Thom. The flow past circular cylinders at low speeds. *Proc. Royal Soc. Lond. A.*, 141:651–669, 1933.

[93] E. Weinan and J. G Liu. Vorticity boundary condition and related issues for finite difference schemes. *J. Comp. Phys.*, 124:368–382, 1996.

[94] G. Dee and J. S. Langer. Propagating pattern selection. *Phys. Rev. Lett*, 50:383–386, 1983.

[95] E. Ben-Jacob, H. Brand, G. Dee, L. Kramer, and J. S. Langer. Pattern propagation in nonlinear dissipative systems. *Physica D*, 14:348–364, 1985.

[96] J. Fineberg and V. Steinberg. Vortex-front propagation in Rayleigh–Bénard convection. *Phys. Rev. Lett.*, 58:1332–1335, 1987.

[97] M. C. Cross. Derivation of the amplitude equation at the Rayleigh–Bénard instability. *Phys. Fluids*, 23:1727–1731, 1980.

[98] M. Lücke, M. Mihelcic, and B. Kowalski. Propagating convection fronts. *Phys. Rev. A*, 35:4001–4003, 1987.

[99] N. Peters. *Turbulent Combustion.* Cambridge University Press, 2000.

[100] G. Ahlers, S. Grossmann, and D. Lohse. Heat transfer and large scale dynamics in turbulent Rayleigh–Bénard convection. *Rev. Mod. Phys.*, 81:503–537, 2009.

[101] A. Pandey, J. D. Scheel, and J. Schumacher. Turbulent superstructures in Rayleigh–Bénard convection. *Nat. Commun.*, 9:2118, 2018.

[102] F. Waleffe. Exact coherent structures in channel flow. *J. Fluid Mech*, 435:93–102, 2001.

[103] G. Haller. Lagrangian coherent structures. *Annu. Rev. Fluid Mech*, 47:137–62, 2015.

[104] B. Suri, J. Tithof, R. O. Grigoriev, and M. F. Schatz. Forecasting fluid flows using the geometry of turbulence. *Phys. Rev. Lett*, 118:114501, 2017.

[105] P. Tallapragada. *Identifying dynamical boundaries and phase space transport using Lagrangian coherent Structures*. PhD thesis, Virginia Polytechnic Institute and State University, 2010.